

ABSTRACT

Title of Document: PREDICTION OF UPWARD FLAME SPREAD
OVER POLYMERS

Directed by: Associate Professor Stanislav I. Stoliarov, PhD
Department of Fire Protection Engineering

In this work, the existing understanding of flame spread dynamics is enhanced through an extensive study of the heat transfer from flames spreading vertically upwards across 5 cm wide, 20 cm tall samples of extruded Poly (Methyl Methacrylate) (PMMA). These experiments have provided highly spatially resolved measurements of flame to surface heat flux and material burning rate at the critical length scale of interest, with a level of accuracy and detail unmatched by previous empirical or computational studies. Using these measurements, a wall flame model was developed that describes a flame's heat feedback profile (both in the continuous flame region and the thermal plume above) solely as a function of material burning rate.

Additional experiments were conducted to measure flame heat flux and sample mass loss rate as flames spread vertically upwards over the surface of seven other commonly used polymers, two of which are glass reinforced composite materials. Using these measurements, our wall flame model has been generalized such that it can predict heat feedback from flames supported by a wide range of materials. For the seven materials tested here – which present a varied range of burning behaviors including dripping, polymer melt flow, sample burnout, and heavy soot formation – model-predicted flame heat flux has been shown to match experimental measurements (taken

across the full length of the flame) with an average accuracy of 3.9 kW m^{-2} (approximately 10 – 15 % of peak measured flame heat flux).

This flame model has since been coupled with a powerful solid phase pyrolysis solver, ThermaKin2D, which computes the transient rate of gaseous fuel production of constituents of a pyrolyzing solid in response to an external heat flux, based on fundamental physical and chemical properties. Together, this unified model captures the two fundamental controlling mechanisms of upward flame spread – gas phase flame heat transfer and solid phase material degradation. This has enabled simulations of flame spread dynamics with a reasonable computational cost and accuracy beyond that of current models. This unified model of material degradation provides the framework to quantitatively study material burning behavior in response to a wide range of common fire scenarios.

PREDICTION OF UPWARD FLAME SPREAD OVER POLYMERS

Isaac T. Leventon

Dissertation submitted to the Faculty of the Graduate School of the
University of Maryland, College Park in partial fulfillment
of the requirements for the degree of
Doctor of Philosophy
2015

Advisory committee:

Associate Professor Stanislav I. Stoliarov, PhD – Chair

Professor Hugh A. Bruck, PhD

Assistant Professor Michael J. Gollner, PhD

Richard E. Lyon, PhD

Professor Emeritus James G. Quintiere, PhD

Professor Michael R. Zachariah, PhD

© Copyright by
Isaac T. Leventon
2015

Acknowledgements

What's the proper way to write an acknowledgements section for something that you've worked on for the better part of a decade? This can't just be about funding and who helped you in lab, on presentations, or with final paper edits. It's probably not even fair to only look back to the first days of grad school, as if getting here was inevitable.

The easiest place to start though is obvious – Dr. Stas thank you for making this possible. You've set the bar so incredibly high on what it means to be a good advisor, mentor, teacher, and researcher. Your careful attention to detail, knowledge of this field, and willingness to support your students whenever they came to you for help is unmatched. Any time we got stuck with our work, there was incredible comfort in knowing that we could come to you to find a way forward. This is an excellent department to be in and, even as part of this group, you clearly stand out as particularly hardworking and wonderfully supportive. You even gave me the freedom to pursue a surprising number of side projects while here, few of which directly advanced my actual research. From mentoring and teaching to just painting dragons and burning Christmas trees you somehow saw some value in these diversions. The ridiculous workload of classes, lab time, and writing that accumulates over years of grad school is unavoidable – everything that made my time here special couldn't have been expected when I started. Thank you for making this experience as rewarding as possible.

To Dr. Rich Lyon at the FAA, the magic that is Grant Number 09-G-018, and Dr. Roland Kraemer at BASF. In a much more practical sense your support made this entire project possible. I suppose it really was just Dr. Stas who earned that support in the first place, but thank you for trusting me to take things over as the years passed and the project grew. Even better, when we have had the chance to meet and discuss our progress, you both showed a genuine interest in this work and a deep understanding of what we're doing and how to improve - that really helped me to believe that my efforts here actually matter.

Lab people – oh, lab people. As much as I like hiding away in my little corner, this wouldn't have all come together without your help. I can't name everyone – maybe you're back overseas, just starting college now, back home to start a new life, or still finishing up here with the department – but thank you going through all this with me.

To the faculty and staff of the Department – I've now taken pretty much every course that is offered here (let's ignore the new ones you've thought up since I finished taking classes, those don't count) and had the chance to work with each and every one of you over the years. I still remember coming to campus at 17 with no real sense of self, purpose, or what I was even doing here and having Dr. Milke steer me towards our intro FPE class. Now, ten years later, we're presenting at the same conferences and working with the same students as they make their way into and through the program. I'm still expecting someone to finally stop me and ask, 'Really? How did you last here this long? You barely know anything, away with you already...' but I've yet to be discovered. That said, after ten years, I've lived in College Park longer than any one other place and,

while I still can look around and see how much more there is to learn, I'm happy to have grown up here. Thank you for helping to make that possible.

Carl – everything that we've worked on together has made it more difficult for me to complete this dissertation, at the very least in the sense of spending time on what I should have been working on. I wouldn't trade that time for anything, even for another frantic week to edit all this. Thank you for connecting me with schools and students in a way that would simply not have been possible otherwise. Some good hopefully came from our efforts and, if nothing else, it was fun and helped me to keep going through the years.

Genevieve – for reasons I'll never really understand, you made it possible for me to continue on this path; I haven't forgotten that. Hopefully that was worth it. Thank you.

Non-school people! Inexplicably, despite the hours that I put in here and my continuing, and questionable, decision to always let work come before any semblance of a social life, I still manage to find myself with a number of great people in my life. Some of you, I've known forever, some for two decades (Joe, you're engaged now, how weird is that? Congratulations), others I may have only met briefly and somehow, luckily, have gotten to know better from a distance; maybe you lived in the Teen Coffee House, have stayed with us for months at a time, just stopped by for dinner and a bonfire, or we only catch up every year or so on a nice, long trip... My life is better because you're a part of it and when writing, research, or any of the other silly obligations that pile up here became overwhelming – and that has happened way more often than I would have liked – it was great to know that somehow, for reasons that still don't add up to me, you're out there.

Warriors – you've been a welcoming and supportive group since the first day I joined you on the ice. You've shared with me so much more than I could ever give back. Thank you for offering me an escape from a lifeless ordinary each week.

Finally, Jackie – it was easy enough to follow you down to Maryland and try to keep up with you grade-wise but those were fairly simple things. Since then, you've gone on to do the whole doctor-professor-married-with-a-family-thing. I've done my best but can't keep up, that ship has sailed. It's probably for the best too. At some point – perhaps at 27, maybe not quite yet – I really have to take off and do my own thing already. You're a few thousand miles away but that doesn't really seem all that far. Thank you for always being there for me and showing me what it means to be a good student, researcher, sibling, and person. Maddie's pretty cool too but she can't read yet so it doesn't matter what I say; she gets a picture instead.

Was it all worth it? It's hard to say. I think I did okay.



Symbols

a	=	Empirical constant in flame height expression
A	=	Pre-exponential constant (Arrhenius reaction rate)
A_s	=	Surface area of sample exposed to the flame
b	=	Empirical constant in flame height expression
B	=	Mass transfer (Spalding B) number
c, c_p	=	Specific heat
$c_0 - c_5$	=	Constants defining polynomial fits of measured burning rate
$d_0 - d_1$	=	Constants defining linear fits of measured base of flame location, y_b
dm'/dt	=	width-normalized mass loss rate
\mathcal{D}	=	Diffusivity
E	=	Activation energy (Arrhenius reaction rate)
h	=	Heat of reaction
h_{burner}	=	Convection heat transfer coefficient (to describe the burner flame)
h_{flame}	=	Convection heat transfer coefficient
ΔH_c	=	Heat of combustion (kJ per gram gaseous volatiles)
I_{ex}^0	=	Incident radiation through an object boundary
J	=	Flux of gaseous volatiles
J_{flow}	=	Mass flux term used to account for polymer melt flow in ThermaKin2D
k	=	Thermal conductivity
P	=	Empirical constant in flame height expression
q_{burner}''	=	Burner (ignition source) flame heat flux
q_{conv}''	=	Convection component of heat flux
q_{ext}''	=	External radiant heat flux
q_{fitted}''	=	Fitted flame heat flux curve, used to represent q''_{HFg}
q_{flame}''	=	Wall flame heat flux
q_{flush}''	=	‘Flush’ denotes the gauge’s position, flush with the surface of the sample
q_{HFg}''	=	Total flame heat feedback measured by a water cooled het flux gauge
q_{net}''	=	Net flame to surface heat flux (into sample)
q_{rad}''	=	Radiative component of heat flux
$q_{rad}^{\%}$	=	Radiative fraction of total heat flux
q_{rad}^{flame}''	=	Radiative component of flame heat flux
$q_{recessed}''$	=	‘Recessed’ denotes the gauge’s position, recessed into the sample’s surface
q_{steady}''	=	Steady flame heat flux (observed for $y \leq y_f$)
\dot{Q}'	=	Width-normalized Heat Release Rate [kW m ⁻¹]

r	=	Reaction rate
r_y	=	Constant defining rate of increase of $q_{rad}^{\%}$ with y
r_0	=	Constant defining $q_{rad}^{\%}$ at $y = 0$
r_1	=	Constant defining $q_{rad}^{\%}$ at $y = 1$ m
R	=	Molar gas constant
t	=	Time after start of test
t_{ign}	=	Ignition time
T	=	Temperature
T_{fl}	=	Flame temperature
$T_{fl,adiabatic}$	=	Adiabatic flame temperature
$T_{fl,max}$	=	Maximum flame temperature (typically a function of $T_{fl,adiabatic}$)
T_{HFg}	=	Heat flux gauge temperature (18°C)
T_{ig}	=	Ignition or pyrolysis temperature
T_{surf}	=	Local surface temperature (of pyrolyzing sample)
u	=	Pre-exponential constant in J_{flow} expression
v	=	Activation energy in J_{flow} expression
V_s	=	Flame speed
w	=	Sample width
x	=	Cartesian coordinate, distance from back of the sample
y	=	Cartesian coordinate, distance from base of the sample (positive above)
y_b	=	Location of the base of the flame
y_p	=	Pyrolysis height
y_{eff}	=	Distance from base of flame
y_f	=	Flame height
y_0	=	Empirical constant in y^* expression; defines length of 'tail' flame heat transfer beyond y_f
y^*	=	Normalized flame length scale
α	=	Radiation absorption coefficient
α_f	=	Empirical constant defining decay (curvature) of flame heat flux with respect to distance downstream of y_f
α_{rad}	=	Absorptivity
δ_f	=	Flame extension length
ε	=	Emissivity
λ	=	Gas transfer coefficient
μ	=	Dynamic viscosity
ζ	=	Concentration of a component [units: mass per unit volume]
ρ	=	Density

Table of Contents

Acknowledgements.....	ii
Symbols.....	iv
Table of Contents.....	vi
List of Tables.....	viii
List of Figures.....	ix
1. Introduction.....	1
1.1 The Fire Problem.....	1
1.2 Controlling Mechanisms of Flame Spread.....	2
1.3 Early Models of Upward Flame Spread.....	5
1.4 Secondary Influences on Upward Flame Spread.....	9
1.4.1 Flame Height and Transition to Turbulence.....	9
1.4.2 Effects of Sample Geometry.....	12
1.5 Purpose of this Study.....	14
2. Flame Heat Feedback Model.....	17
2.1 Material Selection.....	17
2.2 Experimental Procedure.....	18
2.3 Extruded PMMA Burning Behavior.....	28
2.4 Experimental Measurements.....	31
2.4.1 Mass Loss Rate.....	31
2.4.2 Flame Heat Flux.....	34
2.5 Flame Heat Feedback Model Development.....	47
3. Unified Model of Material Burning Behavior.....	54
3.1 Modeling Framework.....	54
3.2 Pyrolysis Model Parameterization.....	61
3.3 Prediction of Vertical Burning and Upward Flame Spread.....	63
3.3.1 Steady Flaming Conditions.....	63
3.3.2 Upward Flame Spread.....	68
3.4 Analysis of Factors Affecting Flame Spread Predictions.....	70
4. A Generalized Wall Flame Model.....	74
4.1 Scaling Approach.....	74
4.2 Material Selection.....	77
4.3 Methods.....	79
4.3.1 Upward Flame Spread Experiments.....	79
4.3.2 Heat of Combustion Measurements.....	83
4.4 Results.....	90
4.4.1 Material Burning Behavior, Qualitative Observations.....	90
4.4.2 Upward Flame Spread.....	101
4.4.3 Heat of Combustion.....	114
4.4.4 Model Generalization.....	121
5. Model Applications.....	139
5.1 Modeling of Standard Flammability Tests – UL 94 and ISO9705.....	139
5.2 Mechanisms of Action of Flame Retardants During Upward Flame Spread.....	143
5.3 FDS Simulations.....	149

6. Conclusions.....	157
Appendix.....	161
A1. Determination of Steady State Flame Heat Flux, q''_{steady}	161
A2. Recessed Heat Flux Gauge Measurements	162
A3. View Factor Calculations.....	165
Theoretical [50].....	165
Empirical.....	166
A4. Adiabatic Flame Temperature Calculations.....	168
A5.1 Propane.....	168
A5.2 Polymeric Materials	170
A6. ThermaKin2D Input Files	175
A6.1 Components (.cmp).....	175
A6.2 Conditions (.cnd); 17.5 cm Tall Sample	176
A7. FDS Input Files (Fine Grid).....	179
References.....	190

List of Tables

Table 1. Calculated radiative fraction of total flame to surface heat flux, $q_{rad}^{\%}$	44
Table 2. Summary of extruded PMMA and Kaowool PM insulation material properties used in the pyrolysis model.....	62
Table 3. Materials used to obtain data for flame model generalization.....	78
Table 4. Test matrix of heat of combustion experiments performed in the cone calorimeter	86
Table 5. Coefficients used with eqn. 32 to describe $\frac{dm'}{dt}$ during upward flame spread ..	105
Table 6. Coefficients used in eqn. 33 to define the location of the base of the flame, y_b , supported by each material as it burns during flame spread experiments	113
Table 7. Heat of combustion (reported in units of kJ per gram volatilized mass)	115
Table 8. CO/CO _x ratios (%) as a function of material and burning configuration	119
Table 9. Flame model input parameters: $T_{fl,adiabatic}^{MATL}$, h_{flame} , and χ_r	126
Table 10. Absolute difference between measured and model-predicted q_{HFg}'' (kW m ⁻²) for each material, averaged throughout the duration of experiments across all measurement locations, y	128
Table 11. Sample preheat and burner application times for PBT samples with various concentrations of bromine- and phosphorous-based flame retardants.....	146
Table 12. Thermophysical properties of methyl methacrylate (MMA) vapor.....	152

List of Figures

Figure 1. Thermal model for surface flame spread.....	3
Figure 2. Sample holder design	19
Figure 3. Experimental setup used for flame spread tests	21
Figure 4. Measured propane burner (sample ignition source) heat feedback.....	26
Figure 5. Representative flame spread test of a 20 cm tall sample of extruded PMMA; this sample is ignited using the final burner configuration.....	29
Figure 6. 13 x 5 cm PMMA sample that did not sustain flaming ignition following burner removal (preliminary configuration).....	30
Figure 7. Measured sample mass loss rate of extruded PMMA samples 3 – 15 cm tall ..	32
Figure 8. Measured burning rate of 17.5 cm tall samples of extruded PMMA	34
Figure 9. Measured extruded PMMA flame heat flux at three heat flux gauge temperatures: 10, 65, and 87 °C.....	35
Figure 10. Measured and fitted extruded PMMA flame heat flux versus time at nine locations $3 \leq y \leq 20$ cm	36
Figure 11. Dependence of steady state flame heat flux on distance from base of sample	37
Figure 12. Measured flame heat flux at sample's center and edge at $y = 7.5$ and 15 cm .	39
Figure 13. Measured q_{HFg}'' at two locations, $y = 10$ and 15 cm, during upward flame spread over 2.5 and 5 cm wide samples of extruded PMMA	40
Figure 14. Representative tests showing recessed heat flux gauge measurements taken at $y = 10$ cm before and after extinction of a wall flame supported by extruded PMMA	42
Figure 15. Radiative fraction, $q_{rad}^{\%}$, of extruded PMMA wall flames	46
Figure 16. Flame height versus sample burning rate during upward flame spread over extruded PMMA	48
Figure 17. Evolution of flame to surface heat flux during upward flame spread over extruded PMMA	49
Figure 18. Normalized flame heat feedback profiles at $15 \leq t - t_{ign} \leq 270$ s	50
Figure 19. Normalized measured flame heat flux as a function of distance from the base of the sample	51
Figure 20. Comparison of experimentally-measured and model-predicted extruded PMMA heat feedback profiles during different stages of flame spread	53
Figure 21. Experimentally-measured and model-predicted mass loss rate observed during vertical burning of 4 cm tall extruded PMMA samples.....	65
Figure 22. Side view images of upward flame spread over a 10 cm tall PMMA sample.	66
Figure 23. Experimentally-measured and model-predicted mass loss rate during upward flame spread over 17.5 cm tall extruded PMMA samples.....	69
Figure 24. Impact of assumed maximum flame temperature on ThermaKin2D predictions of mass loss rate during upward flame spread over PMMA.....	71

Figure 25. Impact of inclusion of melt flow on ThermaKin2D predictions of mass loss rate during upward flame spread over PMMA	73
Figure 26. Cone calorimeter heat of combustion test configurations	84
Figure 27. Measured heat of combustion, ΔH_c heat H_b , of a 10 x 10 cm cast PMMA sample burning in the standard (horizontal) configuration in the cone calorimeter	89
Figure 28. Representative test of flame spread over a 15 cm tall sample of PMMA _{CAST}	90
Figure 29. Representative test of upward flame spread over a 10 cm tall PP sample	92
Figure 30. Representative test of upward flame spread over a 10 cm tall POM sample ..	93
Figure 31. Auto-suppression of upward flame spread over ABS by soot deposition.....	94
Figure 32. Evolution of soot deposition during upward flame spread over 15 x 5 cm ABS samples exposed to an external heat flux of $q_{ext}'' = 10 \text{ kW m}^{-2}$	96
Figure 33. Auto-suppression of upward flame spread over HIPS by soot deposition	97
Figure 34. Sketch of fracture propagation in soot layer formed across the surface of (a) ABS and (b) HIPS samples as they burn in the vertical configuration.....	98
Figure 35. Representative test of upward flame spread over a 10 cm tall FRP sample....	99
Figure 36. Representative test of upward flame spread over a 14.5 cm tall PBT sample	101
Figure 37. Measured width-normalized mass loss rate of PP samples of different heights	102
Figure 38. Measured width-normalized mass loss rate of ABS samples of different heights	102
Figure 39. Width-normalized sample mass loss rate of each polymer tested in this work	104
Figure 40. Measured PMMA _{CAST} flame heat flux at $y = 15 \text{ cm}$	107
Figure 41. Measured PP flame heat flux at $y = 5, 7, 10, 12,$ and 15 cm	108
Figure 42. Measured POM flame heat flux at $y = 5, 7.5, 10,$ and 12.5 cm	108
Figure 43. Measured ABS flame heat flux at $y = 5$ and 11 cm	109
Figure 44. Measured ABS flame heat flux at $y = 7$ and 15 cm	109
Figure 45. Measured HIPS flame heat flux at $y = 5, 7.5,$ and 10 cm	110
Figure 46. Measured FRP flame heat flux at, $y = 5, 7.5,$ and 10 cm	110
Figure 47. Measured PBT flame heat flux at $y = 4.5, 9,$ and 14.5 cm	111
Figure 48. Base of flame location, y_b , during upward flame spread over PMMA _{EXT}	113
Figure 49. Measured heat of combustion (kJ per gram volatilized mass) of ABS, FRP, HIPS, PBT, PMMA, PMMA _{CAST} , PMMA _{EXT} , POM, and PP	116
Figure 50. Changes in relative CO production and heat of combustion of samples burning in the vertical condition without external heating versus in the horizontal configuration with external heating.....	120
Figure 51. Effect of movement of the base of the flame on the relation between flame height and width-normalized mass loss rate during upward flame spread over PMMA _{EXT}	122

Figure 52. Experimentally-measured and model-predicted PMMA _{CAST} flame heat flux at $y = 15$ cm.....	124
Figure 53. Experimentally-measured and model-predicted PP flame heat flux at five locations above the base of the sample, $y = 5, 7, 10, 12,$ and 15 cm	129
Figure 54. Experimentally-measured and model-predicted POM flame heat flux at four locations above the base of the sample, $y = 5, 7.5, 10,$ and 12.5 cm	129
Figure 55. Experimentally-measured and model-predicted ABS flame heat flux at two locations above the base of the sample, $y = 5$ and 11 cm	130
Figure 56. Experimentally-measured and model-predicted ABS flame heat flux at two locations above the base of the sample, $y = 7$ and 15 cm	130
Figure 57. Experimentally-measured and model-predicted HIPS flame heat flux at three locations above the base of the sample, $y = 5, 7.5,$ and 10 cm	131
Figure 58. Experimentally-measured and model-predicted FRP flame heat flux at three locations above the base of the sample, $y = 5, 7.5,$ and 10 cm	131
Figure 59. Experimentally-measured and model-predicted PBT flame heat flux at three locations above the base of the sample, $y = 4.5, 9,$ and 14.5 cm	132
Figure 60. Simplified thermal model for surface flame spread highlighting flame heat losses due to blackbody radiation from soot.....	134
Figure 61. Comparison of flame height correlation developed in this work to literature values	136
Figure 62. Flame height comparison during upward flame spread over PMMA _{EXT}	138
Figure 63. UL94 test setup for samples burning in the vertical configuration	139
Figure 64. Measured and model-predicted width-normalized heat release rate, Q' , of medium density fiberboard samples during the ISO 9705 room corner test [103].....	143
Figure 65. Measured heat feedback from burners used for sample ignition.....	145
Figure 66. Measured flame heat flux at $y = 7$ cm from flames supported by PBT samples with increasing concentrations of a BFR, poly(pentabromobenzyl acrylate).....	147
Figure 67. Visualization of material object and modeling domain in FDS simulations.	150
Figure 68. Predicted net flame heat flux in fine, medium ,and coarse FDS simulations of vertical burning and upward flame spread over 5 cm tall PMMA samples.....	154
Figure 69. Predicted net flame heat flux in FDS and ThermaKin2D simulations of vertical burning and upward flame spread over 5 cm tall PMMA samples.....	155

1. Introduction

1.1 The Fire Problem

The growing prevalence of synthetic polymers in a variety of applications across a wide range of environments has reinforced the need to evaluate and understand the hazards that they pose, specifically in fire scenarios. This rapid expansion of polymer usage in buildings and transportation vehicles has been driven, most notably, by their adaptability and ease of use, low cost, light weight, and, particularly recently, a desire for more energy efficient ‘green’ materials. Consider, for example, a standard wide body aircraft – typically, upwards of 7,000 kg of combustible materials (an equivalent fire load of 500 gallons of jet fuel) fill an interior cabin [1] via [2]. The majority of these combustible materials are synthetic polymers, which are used in a variety of components including, but not limited to, ceiling, wall, and floor coverings, windows, insulation, and seating. This fire load, combined with the high occupant density within the cabin, presents a particularly demanding life safety challenge.

In an effort to better protect against the dangers of unwanted fires, it is important to understand the phenomena that collectively define material flammability and to test materials by the appropriate metrics, given their intended use. Numerous, widely used standard test methods have been defined by organizations such as the American Society for Testing and Materials (ASTM) [3] [4] [5], Underwriters Laboratory (UL) [6], and the Federal Aviation Administration (FAA) [7] to assess material performance in response to fire scenarios based on ignitability and fire resistance, smoke density, burning and heat release rate, and surface flame spread.

Although strong evidence has been put forth suggesting that heat release rate is the most important parameter in fire hazard [8], Ito and Kashiwagi [9] have reported that, “in the initial stages of building fires, flame spread ... is the key determinant of the rate of fire growth.” Upward flame spread over the surface of a material is particularly important because it is frequently present following ignition [10] and, in this configuration, flame spread is most rapid and thus most hazardous [11]. Despite this known challenge, even widely applied test standards that assess flame spread over materials express their results in terms of a relative ranking scale [6] [12], rather than by quantifying the fundamental controlling dynamics of the process, thus they show limited ability to predict material response outside of particular test conditions [13] and conflicting assessments often arise between different tests [14].

1.2 Controlling Mechanisms of Flame Spread

Despite these challenges, the fundamental governing dynamics of flame spread have been studied for more than half a century [15] via. [16]. Upward flame spread is known to be controlled by a positive feedback cycle between coupled processes of solid degradation and gas phase combustion. As gaseous degradation products react with the ambient oxidizer in a diffusion flame, a fraction of heat produced in this reaction is transferred back to the solid, causing further degradation and production of flammable gases. In vertical wall flames, this process has the potential for rapid growth because gasified fuel moves upward, driven by buoyancy, and burns downstream from where it was created, thus heating a region of the solid that is not yet degrading. As seen in Fig. 1, a non-premixed, primarily laminar flame, which is fixed at the base ($y = 0$) of the sample

is supported between the polymer and an idealized thermal boundary layer, TBL. In the pyrolysis region, $0 \leq y \leq y_p$, a constant surface temperature equal to the pyrolysis temperature of the sample (for poly (methyl methacrylate) (PMMA), ~ 650 K [17]) is maintained as heat transfer from the flame is balanced by reradiation, in depth conduction, and the endothermic process of material degradation. Flame to surface heat transfer, \dot{q}''_{flame} , is relatively constant from $0 \leq y \leq y_f$ and decreases farther downstream in the thermal plume where the flame begins to flicker and ultimately burn out.

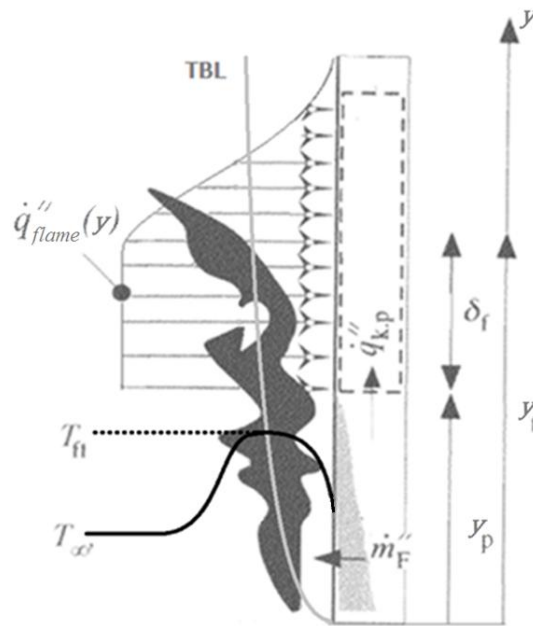


Figure 1. Thermal model for surface flame spread

By 1969, DeRis [18] presented a theoretical description of laminar, opposed flow flame spread over a solid or liquid fuel. Along with a number of simplifying assumptions (notably, ignoring chemical reaction kinetics in the solid and gas phase and treating flame heat transfer as purely conduction) an analytical solution for this two-dimensional flame spread problem was solved for both thin and thick fuel beds. Fernandez-Pello and Williams [19] furthered the study of laminar, opposed flow flame spread with

experimental work focused on downward to horizontal spread over PMMA. Through gas chromatography and detailed measurements of flame radiation and the temperature fields within the solid and the gas, they created a material-dependent, opposed flow flame spread model with conduction through the material as the controlling factor. These models are significant in their contribution to our understanding of flame spread dynamics but they cannot account for the behavior of the much more hazardous upward (concurrent flow) cases.

In 1977, Williams [20] produced an expansive review of studies highlighting the controlling mechanisms of multiple modes of flame spread across different fuel types (solid, liquid, and porous), orientations, and geometries with considerations given to transitional behaviors between these modes. Strongly emphasized was the need to identify and describe the dominant mode of heat transfer to the burning material. Also highlighted was the difficulty in obtaining reliable measurements of this flame heat flux as well as the challenge, when defining a flame spread model, to compromise between including each potentially important phenomena and neglecting all but the most essential ones. Several years later, Fernandez-Pello and Hirano [21] extended this foundation with a review of more recent investigations of flame spread, further emphasizing heat transfer from the flame to the combustible as the primary controlling mechanism of the rate of upward flame spread. With the wealth of knowledge accumulated from these experimental and analytical investigations, models designed to predict upward flame spread began to develop, albeit with a number of simplifying assumptions.

1.3 Early Models of Upward Flame Spread

Markstein and DeRis [11] produced an analytical model predicting the rate of upward flame spread over thermally thin materials. Soon after, Orloff et al. [22] described fire growth as a ‘leap-frogging’ process and developed an approximate theory to predict flame spread rate, which they compared to experimental measurements on large PMMA slabs. Sibulkin and Kim [23] later developed a model that calculated the rate of upward flame spread under laminar or turbulent conditions across solid materials of varying thickness. This work was then expanded upon by Annamalai and Sibulkin [24] [25] by including a careful analysis of ‘excess pyrolyzate’ (Pagni and Shih [26]), which is defined as combustible gases produced by a pyrolyzing sample but burned farther downstream from where they form. Pagni and Shih argue that this excess pyrolyzate controls flame length and hence heat fluxes to the burning material, and they offer a method to quantitatively predict its production as a function of the mass transfer and consumption numbers (B and r , respectively) and the fluid dynamics of the system in question. Annamalai and Sibulkin closely examined heat transfer in the region where excess pyrolyzate is burned and how that controls fire spread rates; they also noted that correlation of experimental results is sensitive to initial ignition conditions.

Numerous later works [14] [27] [28] built upon this foundation to develop simplified, analytical expressions defining the rate of upward flame spread over a fuel surface with each of these analyses resting on a number of key assumptions including two-dimensionality of flame structure (i.e. uniform flame behavior across its width), assuming a constant (or simplified description of) heat flux over the flame length, neglecting gas phase chemical kinetics and details of pyrolysis, and assuming simplified

heat transfer into the solid fuel bed with material thermophysical properties defined as temperature-independent. A representative, first order approximation for upward flame spread rate, V_s , over thermally thick materials can be expressed as [27]:

$$V_s \approx \frac{4(q_{net}'' \delta_f)}{\pi(k\rho c)(T_{ig} - T_{surf})^2} \quad \text{Equation 1}$$

Here, q_{net}'' is net flame heat transfer to the unburned fuel surface and δ_f is the length over which it occurs; k , ρ , and c are, respectively, the material's thermal conductivity, density, and specific heat (collectively known as the material's thermal inertia) and T_{ig} and T_{surf} are the ignition (or pyrolysis) and initial surface temperatures of the unburned material. In such a simplified model, only the fundamental factors that control flame spread rate are considered and, to derive this analytical solution, they're represented here only as constant values. This highlights the importance of better understanding the gas phase quantities of q_{net}'' and δ_f and improving knowledge of material thermal degradation in the solid phase. For flame spread predictions to improve, more precise measurements and detailed descriptions of both flame heat transfer and material thermodynamic and decomposition kinetics properties must be determined.

As time progressed and both computational power and understanding of the controlling mechanisms of flame spread increased, models of constituent processes have correspondingly improved in detail and accuracy. Twenty years after the first flame spread models began to appear, Delichatsios et al. [29] produced a simulation tool that included transient pyrolysis and production of flammable vapors in the solid phase. Solid phase pyrolysis models thus began their evolution from one-dimensional, steady-state

formulations to multi-dimensional, time-resolved solvers with multi-reaction degradation chemistry and temperature and composition resolved thermophysical properties. Currently, state of the art pyrolysis models such as ThermaKin2D [30], Gpyro [31], and the solid phase model in the Fire Dynamics Simulator (FDS) [32] have advanced capabilities considerably beyond those of previous simulation tools. These models can calculate material degradation and decomposition based on knowledge of chemical reactions, phase transitions, and heat transfer through the material with temperature- and composition-resolved thermophysical properties.

Flame heat flux models have similarly advanced in complexity. The simplest method used to model flame to surface heat flux during vertical flame spread is to approximate it as a constant value from the base of a flame up to some effective measure of its height, y_f , and zero beyond (downstream of) that region. Together, the papers written by Tsai et al. [33] and Consalvi et al. [34] provide summaries of twelve different studies that modeled upward flame spread with such a heat flux profile. Between them, flame spread was modeled on a range of different wall materials using constant heat fluxes between 20 and 35 kW m⁻² (most often, 25 or 30 kW m⁻²). These reviews highlight the uncertainty that still remains when defining even this most fundamental variable.

This uncertainty arises largely due to variations in measurement technique and inconsistencies when reporting values of flame heat flux as either net heat transfer to the material or total heat transfer to the measurement device; in some studies, a lack of clarity with regards to this distinction compounds difficulties in interpretation and application of results. The distinction between net and total heat flux is critical because, as a material

heats up, convection heat transfer to its surface decreases and surface reradiation losses increase thus net heat flow into the material can be different than measured values.

More accurate descriptions of flame heat feedback have prescribed a constant value of flame heat flux below the flame height and included a linear [23] or exponentially decaying term farther downstream [16] [33] [35] [36]. In either case, this flame height is often defined with a power law dependence on either pyrolysis height, burning or heat release rate, or some normalized version thereof [22] [29] [35] [36] [37] [38] [39] [40]. It is important to note that this correlation for flame height arises in both theoretically derived models and experimental observations of upward flame spread. In a thorough review of flames burning on surfaces, Lattimer [41] has shown that, for a range of different materials, wall heat flux appears to follow a single spatial distribution: constant underneath the steady portion of a flame, where $y \leq 0.7 y_f$ and decaying with a power law dependence on normalized distance, $\frac{y}{y_f}$, farther downstream. Although fair agreement exists between the measurements collected in this work, some inaccuracy arises due to inconsistent definitions of flame height (typically defined simply by visual observations) and because peak flame heat flux shows some material specificity.

Brehob et al. have suggested that peak measured flame heat flux can be regarded as a “fire property” of the wall lining material and, as part of their research, they showed that it does not increase with sample height, at least up to 1.2 m [16]. Consalvi et al. [42] have suggested an improved method for defining flame height that improves the ability of a single heat flux profile to describe heat feedback from wall flames supported by a range of different materials. In their work, y_f is defined as the position in the flame where “wall

heat flux” exceeds a threshold value of 10 kW m^{-2} ; heat flux is correspondingly prescribed a constant value for $\frac{y}{y_f} < 0.8$ and an exponentially decaying value farther downstream.

1.4 Secondary Influences on Upward Flame Spread

Additional influences on flame spread rate — which must be accounted for when designing experiments, comparing results from different tests, and modeling flame spread — include sample geometry, entrainment of air into the flame, and non-ideal burning behaviors such as charring, soot deposition, melting, and dripping. With a firm understanding of the fundamental phenomena governing flame spread dynamics, it is important to consider the impact of these secondary factors.

1.4.1 Flame Height and Transition to Turbulence

Flame heat feedback is typically defined with reference to a critical length scale — flame height, y_f . Numerous experimental works, studying both solid fuels and gaseous line and wall burners, have thus been performed to determine the height dependence of wall flames. In many of these [11] [22] [23] [25] [37], flame height is defined as a power law function of pyrolysis (or burner) height, y_p , of the form $y_f = ay_p^n$. Such an expression is simple to measure empirically and creates a useful input for flame spread models of the form presented in eqn. 1 (in this expression, the flame extension length can be defined as $\delta_f = y_f - y_p$); however, correlating flame height with pyrolysis height requires the assumption that the local mass loss rate is steady and uniform throughout the pyrolysis zone.

Building upon an integral model for the calculation of turbulent wall flows dominated by buoyancy forces [43], Delichatsios developed a theoretical model that could be used to predict turbulent wall fire behavior, including flame height [44]. Here, flame height is expressed as a function of heat release rate per unit width, Q' , of a wall fire: $y_f \sim (Q')^{2/3}$. In this work, however, the author notes that comparisons of model predictions to small-scale turbulent wall fires were of limited value due to the difficulty in providing accurate flame height measurements. Numerous experimental studies later confirmed the power law dependence of flame height on heat release rate: $y_f \sim (Q')^n$ [35] [27] [39] [45] [46]. Although measuring heat release rate is not a trivial task, correlating y_f with Q' , as opposed to with y_p , allows for better predictions of wall flame behavior.

Functional relationships for flame height have been firmly established; however, the value of the power law exponent, n , in this expression is not universally agreed upon. As shown in a comprehensive study by Tewarson and Ogden [47], $n = 2/3$ (the value originally proposed by Delichatsios) is typically accepted for turbulent wall fires, with experimental observations closely matching this number, although there is some variation in the best fit for specific data sets. For smaller, primarily laminar flames, current results in the literature indicate a larger value of n is required, though its exact value and where this laminar to turbulent transition occurs is still a subject of debate. Several studies on laminar wall flames have suggested that this exponent should be closer to 1, with values reported between $0.71 < n < 1.39$ [10] [37] [40] [46] and [48] via [35]. A recent work by Tsai and Drysdale [39] on vertically burning PMMA samples up to 25 cm in height has measured $0.98 < n < 1.25$, with this variation attributed solely to differences in how samples are mounted.

Predictions of the transition from laminar to turbulent burning behavior have been attempted in a number of ways. Numerous sources simply note this transition as occurring somewhere between 10 and 20 cm (reported as either flame height or the height above the base of the ignition source or burner) [9] [22] [37] [49]. A traditional heat transfer analysis for buoyancy induced flow over vertical walls suggests that this transition would be reached at a Grashof number of $Gr = 4 \times 10^8$ [50]. For wall fires, however, which have steep thermal gradients due to the flame, and which do not have the same smooth, non-reacting wall as described by laminar boundary layer theory (gaseous products of pyrolysis are ejected from burning walls, normal to the primary flow velocity) Pizzo et al. [51] suggest $Gr \approx 5 \times 10^7$ may be more appropriate.

Ahmad and Faeth [52] show a transition between laminar and turbulent behavior in their measurements at a Rayleigh number of $10^8 < Ra_x < 10^9$. In this work, they point out that when flow is ‘tripped’ by a physical obstruction at the base of the pyrolysis zone, turbulent flow can be observed at Rayleigh numbers as low as $Ra = 2 \times 10^6$; however, changes in measured burning behavior are not observed until higher values of Ra are reached. Note: the Grashof and Rayleigh numbers are related as: $Ra = Gr \times Pr$, where Pr is the Prandtl number, which is approximately equal to 0.7 for the temperatures encountered in this system [50].

Multiple other sources suggest that a critical value of heat release rate, $Q' = 20$ kW m^{-1} indicates the boundary between laminar and turbulent fires [34] [39] [40] [46]. Although it is a commonly accepted practice to measure fire size by heat release rate, Pizzo et al. [10] have shown that a single value of Q' cannot be universally applied to mark the laminar to turbulent transition of wall flames of finite width. Specifically, for

samples just 5 or 2.5 cm wide – which support non-uniform burning across their width (mass flux decreases towards sample edges, with this effect more pronounced on narrower samples) – this threshold value of Q' reduces to 17 and 9 kW m⁻¹, respectively. This occurs, they explain, because the reduced burning rate along sample edges necessitates a significantly greater pyrolysis height to yield the same Q' (and thus flame height) in narrow samples.

Whether this transition is best predicted by some physical length scale of the system, or by a threshold value of heat release rate is of secondary concern; it is more important to understand the fundamental reason why this change in behavior occurs and to be able to predict its effects on the key feature of interest in this system – flame to surface heat transfer. When wall flames are laminar, y_f demonstrates a strong dependence on Q' (or y_p). As the system transitions towards turbulent behavior, further increases in Q' produce comparatively smaller increases in flame height because oxygen can be introduced to the flame not just by diffusion, but by turbulent mixing as well. A significant advancement to fire modeling capabilities would be the development of a flame model that can yield accurate predictions not only under either laminar or turbulent conditions but also in the transitional regime between the two.

1.4.2 Effects of Sample Geometry

Material thickness is widely known to influence the rate of upward flame spread, with flames spreading significantly faster over thinner materials than thick ones. Additionally, thermally thin materials have been shown to asymptotically reach a high but constant spread rate due to fuel burnout behind the flame front [11] whereas thermally thick samples allow for a continually accelerating spread rate [20]. These

works, and many others studying upward flame spread, assume a priori that flames can be treated as two-dimensional – that is, although they vary along the length of a sample, y , and normal to the sample surface, flames are uniform across the sample width. Significant effort has been invested into addressing the limiting width at which this assumption breaks down.

Experimental observations on 1 m tall samples of PMMA by Tsai and Wan [53] showed that flame spread rate decreases for samples narrower than 30 cm; however, no obvious effect on flame heat flux distribution or ‘flame height correlation’ was found. Rangwala et al. [49] modified the ‘excess pyrolyzate’ theory of Pagni and Shih [26] to include a Fick’s Law diffusion term that would account for lateral diffusion of gaseous pyrolysis products. Their work predicted a decrease in flame standoff distance and a reduction of the correlation between y_f and y_p as sample width decreases. These theoretical predictions were compared to experimental measurements on 50 cm tall samples, which varied in width, w , from 2.5 to 15 cm. Experimental results showed qualitative agreement with the theory, though the magnitude of this effect was reduced – specifically, with a reduction in sample width from 7.5 to 2.5 cm, y_f is predicted to decrease by ~45% at a given y_p ; however, experimental observations report slightly less than a 20% reduction.

Two further experimental works by Pizzo et al. [10] [51] measured sample burning rate and visually tracked pyrolysis and flame heights during vertical burning of 30 cm tall PMMA slabs of width $2.5 \leq w \leq 20$ cm. These works suggest that flame behavior may begin to change for samples of width less than 20 cm; however, width-normalized burning rate, $\frac{dm'}{dt}$, was consistent between tests performed on 5, 10, 15, and

20 cm wide samples. That is, when ignited identically, samples 5 to 20 cm wide support the same $\frac{dm'}{dt}$ during vertical flame spread over their surface. Further, for flame heights less than 35 cm, dependence of y_f on Q' is consistent for all samples $5 \leq w \leq 20$ cm. For taller flames, the observed dependence of y_f on Q' is reduced for 5 cm wide samples, though the authors suggest that this is likely a result of the flame's transition from laminar to turbulent burning behavior.

Samples only 2.5 cm wide, however, show significant three-dimensional effects – rather than forming a flat, uniform regression front into their surface, as predicted by the two-dimensional theory, these samples exhibited a curved regression front that was markedly deeper at its center than along sample edges. This front had an effective radius of curvature comparable to the sample width itself and provided clear evidence of a non-uniform burning rate across the width of the sample (decreasing from centerline towards the sample edges). Peak, steady state $\frac{dm'}{dt}$ of 2.5 cm wide samples was 40% lower than that of wider samples. These narrow samples also supported greater flame heights than their wider counterparts at all measured Q' .

1.5 Purpose of this Study

Recently, by building upon the wealth of information obtained from these and other studies conducted throughout the last half century, promising results have been obtained by applying Direct Numerical Simulations (DNS) to modeling of laminar wall flames [54] and Large Eddy Simulations (LES) to modeling of turbulent wall fires [55]. However, the computational cost associated with the necessity to resolve near-wall

convection and conduction for laminar wall flames and soot production and radiation for turbulent fires remains extremely high. In this work we present a new model of upward flame spread, which is developed by combining a highly spatially resolved empirical model of flame heat feedback with a state-of-the-art computational pyrolysis solver.

To create the flame heat feedback model used here, detailed measurements of mass loss rate and flame heat flux are carefully obtained as a flame spread vertically upwards over 20 cm tall, 5 cm wide samples of extruded PMMA. This sample size was selected as it represents the critical length scale at which, in likely ignition scenarios, flame spread is the most important hazard determining fire growth. As described earlier in this work, much debate still remains regarding how to best define and predict flame height in wall fires, what exactly is the correct magnitude of peak heat flux in the steady region of a flame, and how does flame heat flux behave farther downstream in the thermal plume, beyond y_f . This wall flame model addresses these questions and offers a significant advancement over similar scaling laws in the literature because it is developed on non-steady (spreading) flames, at the critical length scale of interest, and spanning both the purely laminar and laminar-to-turbulent transitional regimes.

By coupling this model of the flame with the solid phase pyrolysis solver ThermaKin2D, which computes the transient rate of gaseous fuel production of a pyrolyzing solid from fundamental physical and chemical properties of its constituents, a unified description of material degradation and burning is produced. This unified model captures the two fundamental controlling mechanisms of upward flame spread – gas phase flame heat transfer and solid phase material degradation. Effectively, the flame heat feedback model developed here calculates the energy produced by a flame and

transferred back into a material, given its burning rate, while the pyrolysis solver determines the rates at which the material heats up, degrades, and burns in response to this energy transfer. This unified model has enabled simulations of flame spread dynamics with a reduced computational cost and accuracy beyond that of current models.

Our research group has established a systematic methodology for pyrolysis model parameterization of both non-charring [56] and charring polymers [57] as well as for several composite materials [58] [59] [60]. Thus, to fully utilize the capabilities of our unified model of material burning, our wall flame model is further developed such that it can predict the behavior of flames supported by a wide range of materials. This generalization is accomplished through experimental measurements of flame heat flux and sample mass loss rate obtained as a flame spreads vertically upwards over the surface of seven additional widely used polymers, two of which are glass reinforced composites. Each of these materials supports a varied range of burning behaviors including dripping, polymer melt flow, sample burnout, and heavy soot and solid residue formation.

The unified model of material degradation developed here provides the framework to quantitatively study material degradation in response to a wide range of common fire scenarios with a level of accuracy and reduced computational cost unmatched by other currently available models. Characterization of several secondary factors, which may impact upward flame spread, is also presented here, including: the effects of finite width on sample burning behavior, peak flame heat flux, and flame heat flux distribution; the impact of soot deposition and char formation at a material's surface and polymer melt flow and dripping on flame heat transfer; and determination of the flame to surface heat transfer mechanism (convection vs. radiation) of < 20 cm tall wall flames.

2. Flame Heat Feedback Model

2.1 Material Selection

The flame model developed in this work was created based on experimental measurements of mass loss rate and heat flux from flames spreading vertically upwards across the surface of extruded PMMA. This PMMA was purchased in the form of 5.9 mm thick, clear sheets produced by Evonik Industries and distributed by the US Plastic Corporation. This material was selected because it is a widely used commodity plastic that is easily ignitable and non-charring and it does not form excessive amounts of soot while burning. Although cast PMMA is often utilized in research because it does not soften and flow during heating in the vertical configuration, which makes it easier to study, this form of the material is seldom used in common engineering applications. Additionally, dripping is a common behavior supported by many synthetic polymers as they burn in the vertical configuration thus this behavior should not be avoided in experimental research. During flame spread experiments conducted here, extruded PMMA samples exhibit a moderate melt flow, which is analyzed and accounted for as described in later sections of this manuscript.

Although PMMA was extensively studied in this work, the goal here was not to analyze measurements of its burning rate and flame heat feedback and assume that they directly characterize the wall flames supported by any material without any further analysis or adjustment. Instead, we sought to create a baseline model predicting flame heat feedback that accounts for the primary controlling dynamics common to all materials burning in this orientation. With this foundation, the flame model can be further developed to describe flames supported by a wide range of wall materials (this generalization is

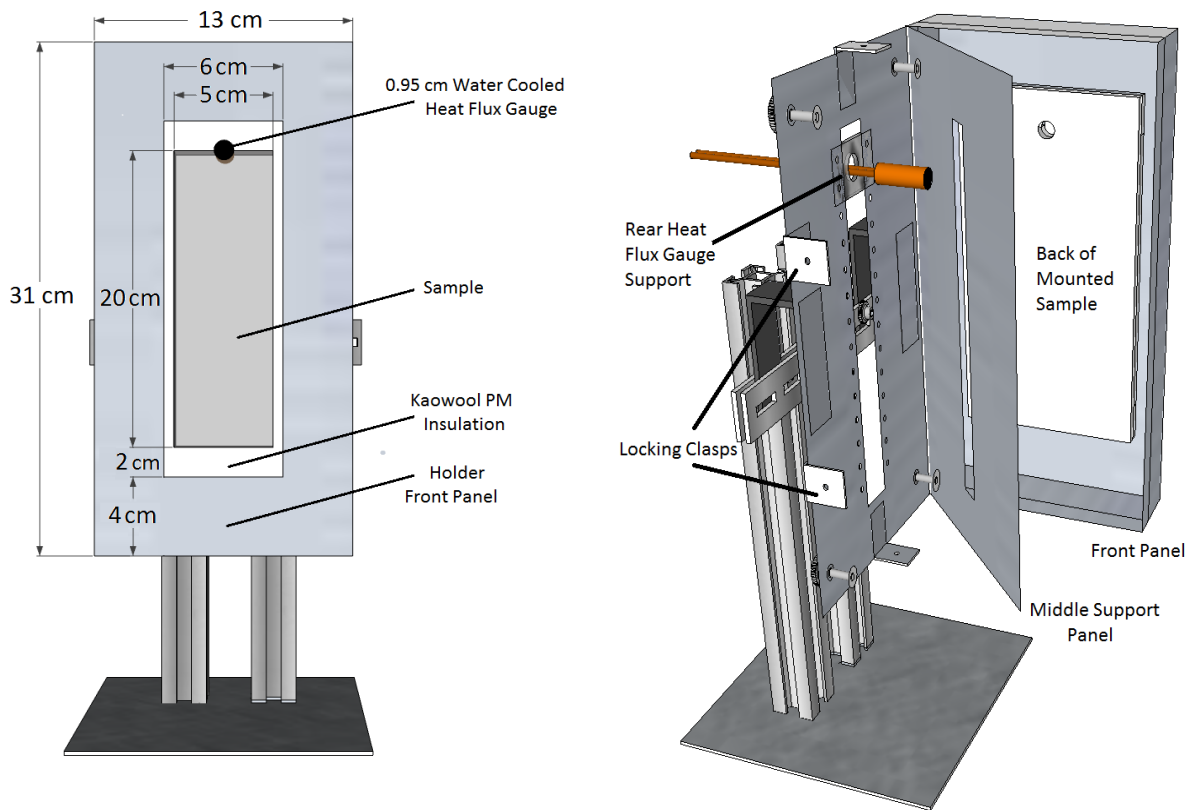
described in Section 4 of this manuscript) and the impact of complex, though common, secondary burning behaviors can be uniquely quantified by experimental measurements so that they can be incorporated as submodels when needed.

2.2 Experimental Procedure

Extruded PMMA sheets are cut into 5 cm wide strips, cut to the sample height needed for each test, and then weighed. This sample width was selected because previous experimental studies have demonstrated that, in the vertical burning configuration, 5 cm wide PMMA slabs produce the same width-normalized burning rate as wider slabs when each are uniformly ignited across their base [10]. Using samples of this width thus ensures that edge effects are minimal and two-dimensional wall flame behavior should be observed in test conducted here. Cut samples are mounted onto a 5.9 mm thick sheet of Kaowool PM insulation board (which has well-defined thermophysical properties [61]) and surrounded by a 2.5 cm strip of the same insulation at its top, bottom, and two sides. Samples and the surrounding insulation pieces are secured to the back insulation panel using a thin layer (less than 0.5 mm thick) of a high temperature Loctite epoxy (manufactured by 3M). Prepared sample-insulation assemblies are placed in a desiccator for a minimum of 24 hours prior to use in testing.

As seen in Fig. 2, in each test, sample-insulation assemblies are secured within a steel holder that exposes only the front surface of the PMMA slab as well as 2.0 and 0.5 cm, respectively, of insulation above/below and to either side. Pressed forward into the front of the holder, the sample's front surface is effectively extended by an additional 4 cm in all directions by the (1.4 mm thick) front panel of the holder; this allows for

unimpeded lateral air entrainment from either side of the sample. Extension of the lower edge (beneath the sample's base) in this manner has been shown to limit the introduction of turbulence in wall fires [39]. Supporting samples in this configuration allows a small, primarily laminar flame to spread upwards across the front surface of a sample with repeatable, well defined boundary conditions.



(a) Front view showing a 20 cm tall sample, mounted on insulation and set in place inside the steel holder.

(b) Side view showing heat flux gauge and sample supports. When the front panel is closed, it is locked in place by four (top, bottom, and sides) clasps and the middle panel is pressed forward by thumbscrews at all four corners to secure the sample in place.

Figure 2. Sample holder design

As seen in Fig. 3, at the start of each test, the sample holder is placed underneath an exhaust hood, which captures products of combustion as the material burns, and surrounded by fire curtains, which limit horizontal perturbations of air. This setup ensures quiescent conditions around the sample (induced vertical air velocity of approximately 5 cm s^{-1}) without relying upon side walls positioned immediately adjacent to the sample. Tests begin by igniting a 5 cm wide non-premixed propane burner that is positioned below the bottom edge of samples. The burner is provided with $0.15 \text{ L min}^{-1} \pm 1\%$ (at 1 atm and 298 K) of propane. This flow rate is measured by a Bios Defender 530 flow meter and regulated using a needle valve. To limit the area of the sample preheated by the burner and to provide reproducible and well-defined ignition conditions, the burner flame is restricted by a steel shield positioned horizontally above the base of the sample (see Fig. 3). This configuration provides a constant, well defined heat flux to the sample throughout the duration of its exposure. The burner is left in place just long enough for sustained, uniform ignition of the sample along its bottom edge. Samples are allowed to burn until completely involved (i.e. pyrolysis observed across their entire surface), until steady state measurements of flame heat flux are recorded for at least 60 s, or until secondary burning behavior (e.g. polymer melt flow) have a significant impact on material burning behavior. All tests are videotaped.

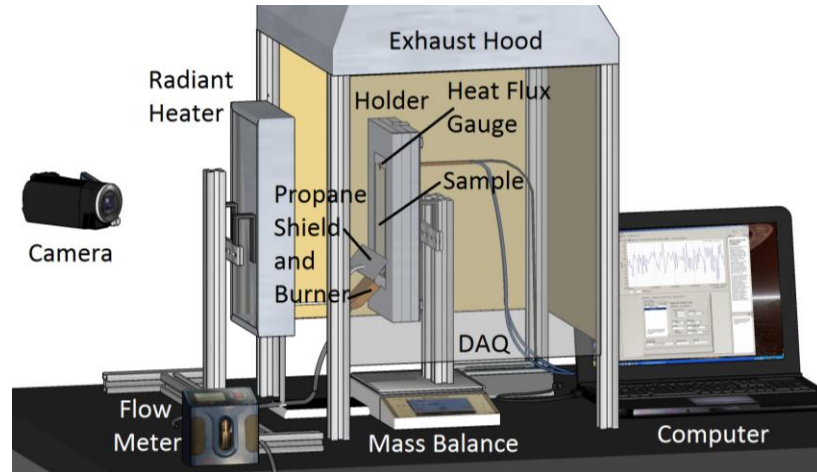


Figure 3. Experimental setup used for flame spread tests

Also shown in Fig. 3 is a radiant heater, supported on a sliding track, which can be positioned to provide up to 20 kW m^{-2} to the sample's front surface. This external heat flux, q''_{ext} , remains constant throughout the length of its exposure and is measured to be fairly uniform (spatially), deviating by just 10%, on average, across the material's surface. This external heat flux can be used to represent the radiation heat transfer that commonly arises in enclosure fires. The use of such a heater has been shown to induce flame spread across materials that cannot independently sustain the process and to enhance the rate of fire growth over materials that can [62]. Although this heater was not used for tests on PMMA, it is needed to promote flame spread and continued burning of several other materials tested in this work; these experiments are described in detail in later sections of this manuscript.

Two types of measurements are obtained from independent experiments conducted in this test apparatus: sample mass loss rate and flame heat flux. In mass loss rate tests, the sample holder is placed atop a Mettler Toledo XS4002S mass balance, which records total sample mass throughout the duration of experiments at a frequency of

1 Hz. Width-normalized mass loss rate, $\frac{dm'}{dt}$, is calculated as the numerical derivative of measured sample mass, using a 1 s time step, divided by sample width, $w = 5$ cm. Signal noise is subsequently reduced by applying a 5 s running average to $\frac{dm'}{dt}$ histories from each individual test. Tests are repeated four to six times each for all sample heights of interest; measurements from repeated tests are averaged together and this combined dataset is further smoothed using a 5 s running average prior to further analysis.

At later times in each test, samples 10 cm or taller begin dripping at a measurable rate. These drips remain on the mass balance after sliding off from the sample slab and the pool that forms continues to burn until samples were extinguished. This pool fire is small and has no impact on flame to surface heat feedback; however, it does affect $\frac{dm'}{dt}$ measurements. To correct for this behavior, a second series of tests is conducted in which sample drippings are carefully and continuously collected, removed, and extinguished as they fall, and a corrected mass loss rate, which represents the mass loss rate of only the material burning on the wall, is thus determined.

In experiments measuring flame to surface heat feedback, samples are further prepared by drilling a hole at the upper edge and along the centerline (width) of the PMMA slab to allow a heat flux gauge to be tightly secured, such that its face is flush with that of the slab and the surrounding insulation (above) and so that its center rests directly on the divide between the two (see Fig. 2). Here, a 0.95 cm diameter, water cooled Schmidt-Boelter heat flux gauge (manufactured by Medtherm) is used to measure total flame to surface heat flux, q''_{HFg} , at 2 Hz using an NI USB-9211A data acquisition

module (DAQ) connected to a computer. The use of a heat flux gauge in a similar configuration was previously shown by Beaulieu and Dembsey [26] to provide accurate measurements of flame to surface heat flux. To test the uniformity of flame heat flux across the width of samples (and thus verify the two dimensional nature of this flame) additional samples, 7.5 and 15 cm tall, are prepared such that a heat flux gauge could be placed just inside the left or right edge of the PMMA slab. All heat flux experiments are repeated three times for each sample height; measurements from repeated tests are averaged together and this combined dataset is smoothed using a 5 s running average.

Before each test, the heat flux gauge was cleaned and recalibrated by placing it beneath the radiant heater of a Govmark CC1 Cone Calorimeter, directly beside a reference gauge. After every three tests, heat flux gauges are repainted using an optical black coating supplied by the gauge manufacturer, which provides a listed average absorptance of 0.95 from 0.3 to 15 μm . Repeated refinishing of the heat flux gauge ensured the accuracy of experimental measurements, despite the accumulation of deposits on the surface of the heat flux gauge during tests. During calibrations, both the experimental and the reference gauge are cooled with water at 18 \pm 7 $^{\circ}\text{C}$ (this variation results from seasonal changes in the laboratory's water temperature), as used during the majority of testing. Gauges were calibrated using incident radiant heat fluxes of 20, 35, and 50 kW m^{-2} with a measured response of zero when the heater was off. The heat flux gauge calibration coefficient is determined by relating the voltage generated by the experimental gauge thermopile to the heat flux measured by the reference gauge.

It has been suggested in the literature [63] that increasing the temperature of water flowing through a heat flux gauge above 65 $^{\circ}\text{C}$ improves the accuracy of the gauge

readings by preventing condensation of pyrolysis and combustion products on the face of the gauge. Additional tests were thus conducted on PMMA in which the heat flux gauge was cooled using 10, 65, or 87 °C water. In these tests, heat flux gauge water temperature is maintained using a Julabo F25 water circulator connected to a heat flux gauge with thermally insulated tubing. During calibration, experimental gauges were cooled by water at the same (elevated or reduced) temperature as used during testing versus a reference gauge cooled to 18 °C.

Two different burner configurations were used to ignite samples. In preliminary testing, the burner was positioned at $y = -1$ cm and the burner shield was positioned at $y = 3.5$ cm. Here, and throughout this manuscript, y indicates distance from the base of the sample ($y > 0$ above the sample's base). In final testing, the burner is lowered to $y = -1.8$ cm and the burner shield is repositioned to $y = 2.25$ cm. In both configurations, the burner flame is effectively cut off by this shield, thus allowing for careful control of the region of the sample preheated by the burner. Total burner flame heat flux (q''_{HFg}) is measured at 0.25 to 0.5 cm intervals from $y = 0$ cm up to and beyond the burner shield using the same water cooled Schmidt-Boelter heat flux gauge used for measurements of PMMA wall flames; near the shield, the spatial resolution of these heat flux measurements was increased. For measurements of burner flame heat flux, small sheets of Kaowool PM insulation were used to represent sample slabs. These sheets were supported in the steel holder and the heat flux gauge was mounted flush with their front surfaces at the measurement locations, y , of interest.

Fig. 4 compares the measured flame heat feedback profiles of each burner configuration; also shown here is the parameterization of the final burner heat flux profile

as defined in numerical simulations, performed using ThermaKin2D, which are described in later sections of this manuscript. At each measurement location, burner flame heat flux measurements remain constant, with respect to time, throughout the duration of burner exposure. Burner flame heat flux is also found to be fairly uniform across the width of the sample (less than 10% deviation from the center reading). Every three months, the burner heat feedback profile is re-measured to ensure consistent performance. These measurements indicate that, despite frequent, repeated use, burner flame heat flux remained primarily unchanged throughout the full series of experiments presented in this work. In its final configuration, the burner must be applied longer – 125 s versus just 75 s with the original burner design – to ignite PMMA samples. However, in the final configuration, the spatial uniformity of the burner flame heat feedback profile is greatly improved – unlike in the preliminary setup, the final burner configuration does not induce increased heat transfer near the burner shield.

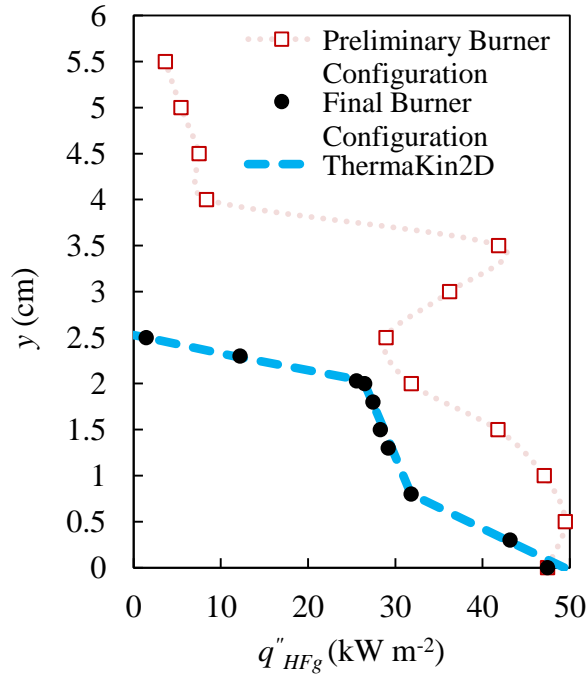


Figure 4. Measured propane burner (sample ignition source) heat feedback

Ideally, the entire flame heat feedback profile could be measured in a single experiment using an array of heat flux gauges; however, this would create at least two significant challenges. First, embedding such a large number of thermostated gauges in the sample slab would produce local distortions in material burning behavior and in the temperature and structure of the gaseous flow field above the sample. Second, as synthetic polymers heat up, they can soften, melt, and drip down; these drippings could destroy, or at the very least strongly alter, the face of the gauge by the end of each test, thus rendering final measurements unusable. A height resolved heat feedback profile is therefore obtained by preparing samples of different heights, from 2 to 20 cm tall, igniting them identically, and measuring flame heat flux at the tops of each one, with a single gauge, as a flame spreads across their surface. In this manner, heat flux measurements recorded at the top of each smaller sample could be used to represent those

that would be obtained at the same height in a full sized sample. Although this process requires a greater number of experiments, it has provided reliable measurements that can be combined to create an effective heat flux profile across the full sized sample

To justify combining measurements in this fashion, one must consider the main assumption in doing so – measuring the heat flux at the top of a small sample of PMMA yields the same result as measuring the heat flux at that same height in a larger sample. This should be expected; conditions downstream of the measurement location (here, above the heat flux gauge) should have no significant effect on the reacting flow of interest. The substitution of insulation for PMMA at the top of the gauge should not affect measured heat flux as the hot boundary layer gases must already have crossed the face of the heat flux gauge before passing over this region. Also, as the gauge itself is small (0.95 cm in diameter) and the front surfaces of the sample, heat flux gauge, and upper layer of insulation are each flush with one another, the insulation/polymer boundary should not cause a significant physical disturbance in the reacting flow.

The sensitivity of flame heat flux measurements to material composition downstream of the gauge was examined by additional verification experiments in which the heat flux gauge was fully surrounded by PMMA – in these tests, the heat flux gauge was positioned such that its top edge is below the top edge of the sample. Additionally, in a preliminary series of tests, the mass loss rate of seven different sized samples, from 3 to 15 cm tall, was also measured to ensure that the burning behavior of smaller samples represented that which would be produced by the lower regions of a full sized sample, at least until their entire surface is pyrolyzing. The results of these tests are presented in greater detail in Section 2.4.1 of this manuscript.

2.3 Extruded PMMA Burning Behavior

Fig. 5 shows typical fire growth during upward flame spread over a 20 cm tall extruded PMMA sample; here, samples are ignited by the propane burner in its final configuration. Timestamps at the bottom of this figure indicate time after sample ignition, $t - t_{ign}$. Extruded PMMA samples can be uniformly ignited across their base by a 75 or 125 s exposure to the propane burner (ignition time, $t_{ign} = 75$ or 125 s) in either its preliminary or final configuration, respectively. Time $t = 0$ s corresponds to the start of each experiment, when the propane burner is first applied to the sample. Within 10 s of ignition, PMMA flames grow to approximately 4 – 5 cm in height. A thin (< 0.5 mm), layer of soot is observed to quickly deposit between the flame and the surface of the virgin material, downstream of the pyrolysis front at $y > 4$ cm. This layer does not appear to impede flame spread but it effectively transforms PMMA slabs from clear to non-transparent. Soot deposition in this manner is important because it is well known [47] that in depth radiation absorption can affect the rate of flame spread.

As extruded PMMA continues burning, the flame it supports grows and transitions away from purely laminar behavior. During the first 180 s after ignition ($0 \text{ s} < t - t_{ign} < 180 \text{ s}$) PMMA samples remain primarily stationary (minimal melt flow) with only small, narrow drips of the melted polymer beginning to extend 1 cm below the sample's base. At this point in the test, flame tips can be seen up to $y = 20$ cm. Approximately 240 s after sample ignition, drips (polymer melt) begin intermittently falling from the sample to the base of the holder below. These drips form a small pool of fire at the holder's base though, initially, their impact on measured burning rate is negligible. After $t - t_{ign} = 330$ s, the drip pool has grown larger and burns at a low, but

measurable, rate. By the end of each test on samples between 15 and 20 cm in height, approximately 15% of the sample's original mass has been lost due to dripping, not burning. Smaller samples less than 10 cm tall do not exhibit such melt flow behavior.

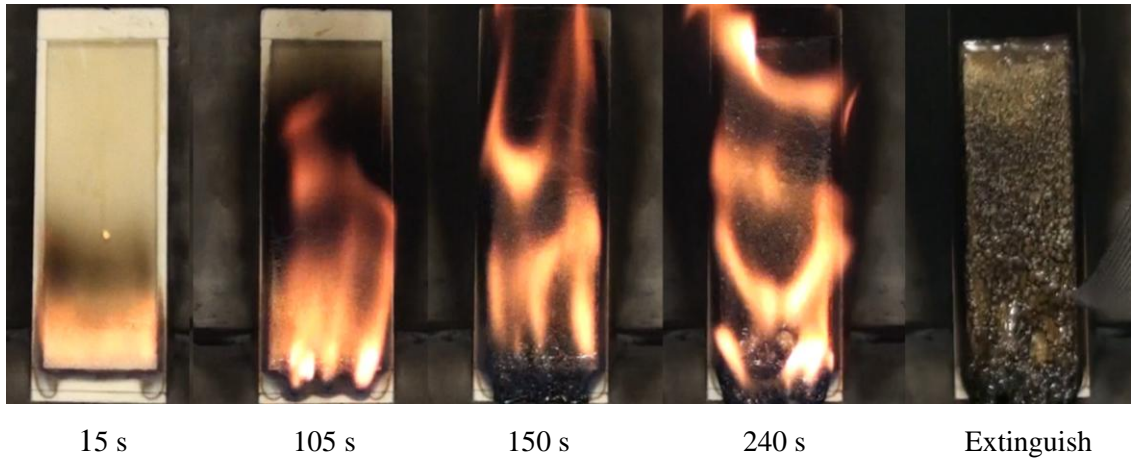


Figure 5. Representative flame spread test of a 20 cm tall sample of extruded PMMA; this sample is ignited using the final burner configuration

An extensive series of tests was conducted in which samples were ignited by the propane burner in its preliminary (larger) configuration. These tests yielded detailed, spatially resolved measurements of steady state flame heat flux (where $y < y_f$) and insight into the dependence of flame height on sample mass loss rate [64]. As seen in Fig. 6, in these tests, samples were preheated (see burner heat flux distribution, Fig. 4) such that the region closest to the burner shield began pyrolyzing sooner than the region between 1 and 3 cm above the sample's base. This appeared to create a 'dual flame' system – one anchored to the base of the sample and another tied to this forward region – that allowed for rapid flame spread over the base of the sample early in testing. Igniting samples with the final (smaller) burner design, precluded the development of this complex ignition

behavior, thus it was from this series of experiments that an expression defining flame heat feedback as a function of sample mass loss rate was determined.

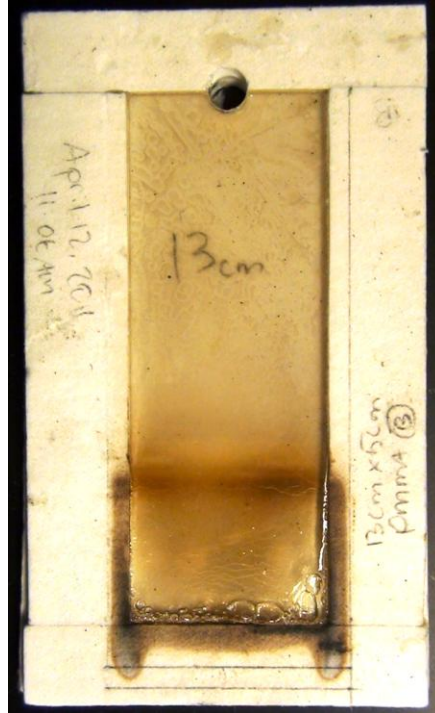


Figure 6. 13 x 5 cm PMMA sample that did not sustain flaming ignition following burner removal (preliminary configuration)
Note the two regions of material decomposition: one at the sample's base and a second, close to the burner shield, at $y = 3.5$ cm.

2.4 Experimental Measurements

2.4.1 Mass Loss Rate

Fig. 7 shows $\frac{dm'}{dt}$ measured as a flame spread across the surface of 5 cm wide extruded PMMA samples of seven different heights, from 3 to 15 cm tall. Here, each sample was ignited by the propane burner in its preliminary configuration. Measured mass loss rates of each sample 5 cm or taller are nearly identical until $t - t_{ign} = 90$ s. This indicates that only the lower 5 cm of any sample is undergoing significant pyrolysis during this time period. Measured mass loss rate of 3 cm tall samples quickly differs from that of larger samples. Such behavior is expected here because, in these preliminary tests, the entire surface of this sample is preheated by the propane burner, thus allowing the flame to quickly spread across this region of the sample by $t - t_{ign} = 15$ s. A more general observation that can be derived from these measurements is that the mass loss rates of smaller PMMA samples are equivalent to that of the full-sized sample until a certain time in the experiment. For successively larger samples, this time period of equivalent burning is progressively longer. In other words, $\frac{dm'}{dt}$ of any two samples is equivalent until the pyrolysis height, y_p , reaches the top of the shorter sample.

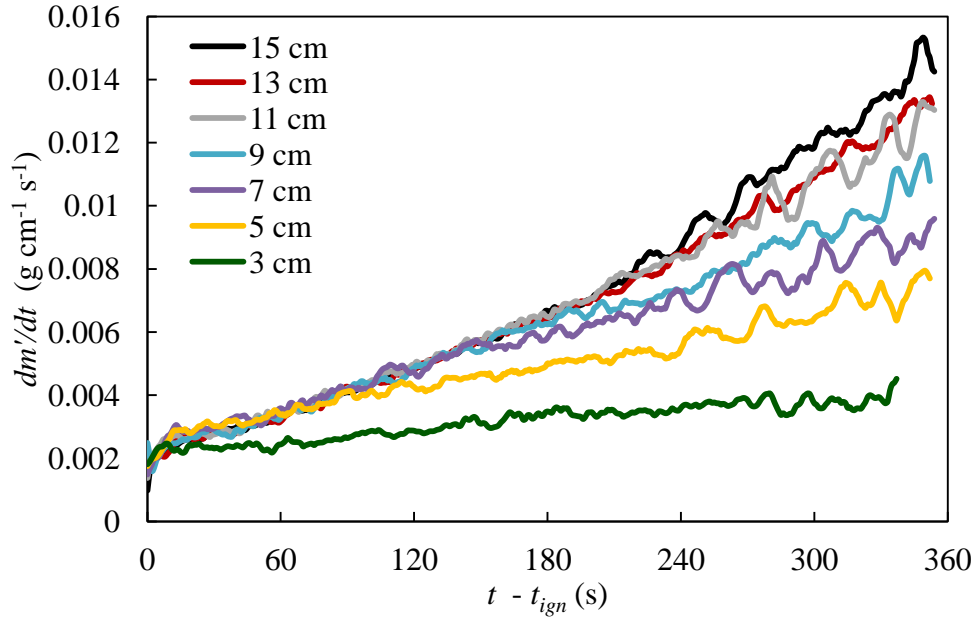


Figure 7. Measured sample mass loss rate of extruded PMMA samples 3 – 15 cm tall
 Note: here, samples are ignited by the propane burner in its preliminary configuration.

These measurements indicate that the burning dynamics controlling the development of the pyrolysis zone is not altered between PMMA samples of different heights when they are ignited identically. Thus, for flame model development – in which heat flux measurements taken at the tops of different samples are combined to form an effective heat feedback profile across the length of the flame – a single mass loss rate, that of the largest samples tested, can be used to characterize the burning behavior of all samples that height or smaller. Here, however, $\frac{dm'}{dt}$ from the second largest, 17.5 cm tall, samples was used as these samples showed greater resistance to melt flow. When analyzing heat flux measurements taken at the tops of 20 cm tall samples, only those recorded during the first 300 s after sample ignition were considered. During this 300 s period, the pyrolysis front was well below the top of 17.5 cm samples, hence their

measured mass loss rate could still be used, with confidence, to characterize the behavior of these slightly taller samples.

At later times in each test ($t - t_{ign} > 330$ s), 17.5 cm tall samples began dripping at a measurable rate. Although this melted PMMA remained on the mass balance after separation from the main slab, the small pool that formed would burn until samples were extinguished. Flames from this drip pool were never in contact with the sample above and thus this drip pool's small addition to measured sample mass loss rate was removed (as it had no contribution to flame to surface heat feedback). To make this correction, sample drippings were carefully and continuously collected, removed, and extinguished as they fell, and a corrected mass loss rate, which represented the burning rate of only the material burning on the wall was thus determined.

Both corrected and uncorrected sample mass loss rate measurements are plotted in Fig. 8, along with the fitted polynomial curve used to smooth final results. In each of these tests, samples are ignited by the burner in its final configuration. After ignition, the burning rate history for a 17.5 cm tall PMMA sample can be described by:

$$\frac{dm'}{dt} = -5.40 \times 10^{-15} (t - t_{ign})^5 + 4.35 \times 10^{-12} (t - t_{ign})^4 - 8.13 \times 10^{-10} (t - t_{ign})^3 + 4.75 \times 10^{-9} (t - t_{ign})^2 + 2.79 \times 10^{-5} (t - t_{ign}) + 1.44 \times 10^{-3} \quad \text{Equation 2}$$

where $\frac{dm'}{dt}$ is in $\text{g s}^{-1} \text{cm}^{-1}$ and t is in s.

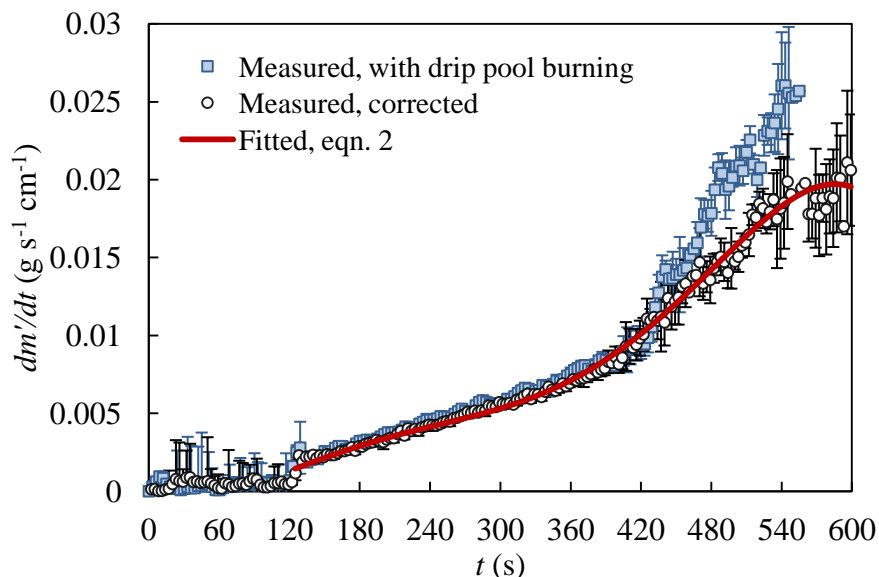


Figure 8. Measured burning rate of 17.5 cm tall samples of extruded PMMA
 Note: here, samples are ignited by the propane burner in its final configuration

2.4.2 Flame Heat Flux

2.4.2.1 Effects of Heat Flux Gauge Temperature on Flame Heat Flux Measurements

Fig. 9 presents total PMMA flame heat flux measured at two heights, $y = 5$ and 15 cm, as recorded by heat flux gauges cooled by water at 10, 65, and 87 °C; here, samples are ignited by the propane burner in its preliminary configuration. As shown here, q''_{HFg} demonstrates no significant dependence on heat flux gauge temperature. Identical results (which are not shown in this figure) are observed when flame heat flux is measured in this manner at $y = 8$ and 12 cm. Although using warmer water did improve the physical appearance of the gauge by the end of each test – deposition of combustion products at the front surface of the heat flux gauge was limited in these experiments – because q''_{HFg} shows no sensitivity to gauge temperature, tap water (at an average temperature of 18 °C) was used to cool heat flux gauges during all other tests conducted in this work and presented throughout this manuscript.

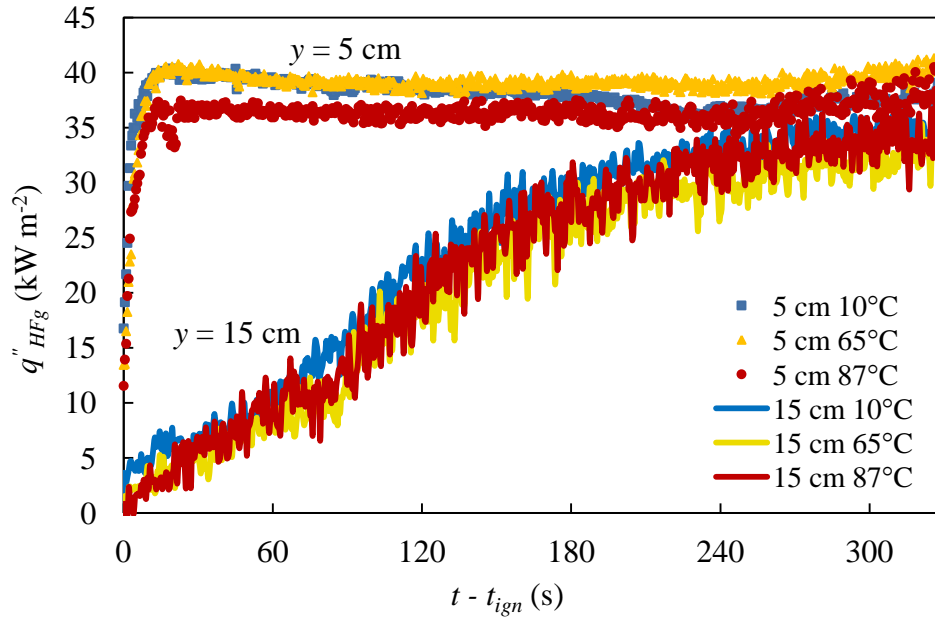


Figure 9. Measured extruded PMMA flame heat flux at three heat flux gauge temperatures: 10, 65, and 87 °C

2.4.2.2 Measured heat flux, q''_{HFG}

Fig. 10 shows q''_{HFG} measurements (solid lines) of extruded PMMA flames recorded at nine locations $3 \leq y \leq 20$ cm; here, samples are ignited by the propane burner in its final configuration. Also shown in this figure are fitted curves (q''_{fitted} , dashed lines) which are used to represent these measurements in further analysis when a reduction in noise in the reported signal is desired. At each measurement location, y , q''_{fitted} is piecewise defined by a series of third to fifth order polynomials. For each sample height, q''_{HFG} increases with time before reaching a relatively steady value, q''_{steady} . As expected, it takes progressively longer for q''_{steady} to be observed at higher heights; the delay

corresponding to the great amount of time required for the flame to spread to, and establish itself above, the measurement location.

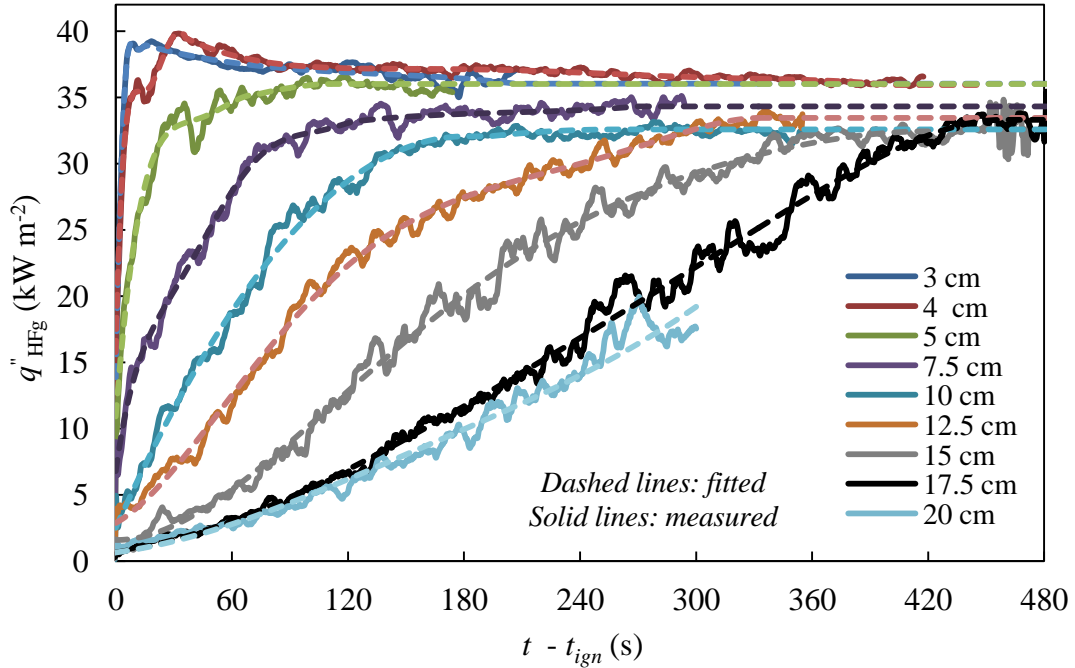


Figure 10. Measured and fitted extruded PMMA flame heat flux versus time at nine locations $3 \leq y \leq 20$ cm

Steady flame heat flux was determined¹ at each measurement location by averaging measured q''_{HFg} over the 30 s time period immediately following the first time

in experiments when $\frac{d(q''_{fitted})}{dt} \leq 0.02 \text{ kW m}^{-2} \text{ s}^{-1}$. q''_{steady} is typically within 2 kW m^{-2} of

the maximum heat flux recorded at the same location and was found to be somewhat dependent on the position of the gauge, y , with respect to the bottom of the flame (or PMMA sample). This dependence is shown in Fig. 11 along with similar measurements of q''_{steady} determined at 1 cm intervals, from $y = 2$ to 15 cm, in experiments where

¹ The systematic procedure used to determine q''_{steady} is presented in greater detail in the appendix.

samples were ignited using the preliminary burner configuration. While the evolution of the flame heat feedback profile may have been affected by the burner configuration, peak steady state flame heat flux is independent of these ignition conditions. Thus, at sample heights where flame heat flux was measured in both studies, an average value of q''_{steady} (weighted by total number of tests) is reported; error bars in this figure, and all others in this work, represent two standard deviations of the mean.

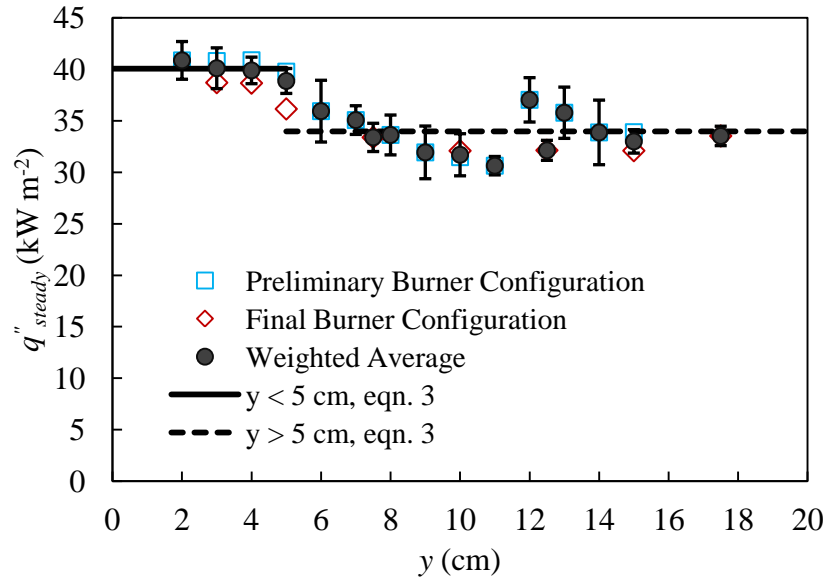


Figure 11. Dependence of steady state flame heat flux on distance from base of sample

q''_{steady} is highest near the sample's base and decreases slightly farther downstream, where it averages to a single value at larger heights. This trend is consistent with the structure of the flame, which is thinnest and closest to the sample surface at the base of the sample. The asymptotic behavior of q''_{steady} at larger heights is in agreement

with previous observations in the literature [16]. q''_{steady} can be simply, but accurately, expressed as a piecewise linear function of y :

$$q''_{steady} = \begin{cases} 40 \text{ kW m}^{-2} & ; y \leq 5 \text{ cm} \\ 34 \text{ kW m}^{-2} & ; y > 5 \text{ cm} \end{cases} \quad \text{Equation 3}$$

2.4.2.3 Impact of Finite Sample Width on Flame Heat Flux

At two heights, $y = 7.5$ and 15 cm, flame heat flux was measured by a heat flux gauge positioned such that its outer edge lined up with the left or right boundary of the PMMA slab. In these tests, samples are ignited by the propane burner in its final configuration. As seen in Fig. 12, as the flame spreads across the sample, q''_{HFg} is initially slightly lower at the edge than along the centerline of samples; however, by the end of each test, a single value of q''_{steady} is measured across the width of the sample. The difference between measured centerline and edge flame heat flux never exceeds 4 kW m^{-2} . During the early stages of each test (as the flame spread towards the heat flux gauge) this difference likely results from flickering (partial extinction) and random side to side motion of the flame. This behavior is more prominent downstream of the steady region of the flame, where it narrows towards its tips. Ultimately, these results indicate that heat transfer from these wall flames is primarily uniform across the width of the sample.

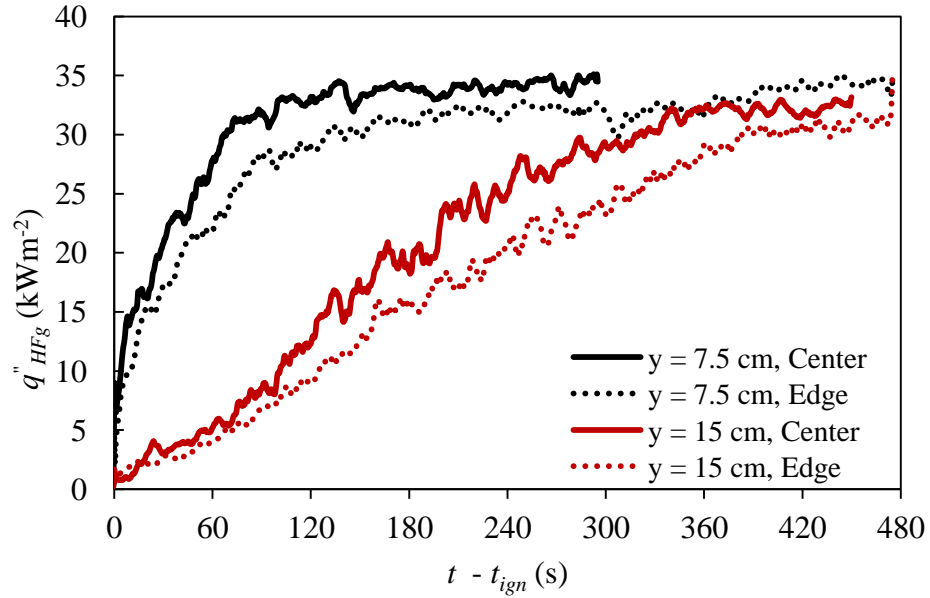


Figure 12. Measured flame heat flux at sample's center and edge at $y = 7.5$ and 15 cm

Flame heat flux was also measured along the centerline of 2.5 cm wide samples at $y = 10$ and 15 cm; these measurements are shown in Fig. 13 alongside those recorded at the same locations, y , in experiments conducted on 5 cm wide samples. In each of these tests, samples are ignited using by the propane burner in its preliminary configuration. As seen here, there is a slight delay before q''_{steady} is observed on 2.5 cm wide samples as compared to their 5 cm wide counterparts. This delay increases with the height of the measurement location, y and can be observed in Fig. 13 as the increasing (horizontal) separation of measured heat flux curves obtained from samples of the same height, but different widths. Although slight, this behavior corresponds with observations in the literature, which suggest very narrow samples will support shortened flames [49].

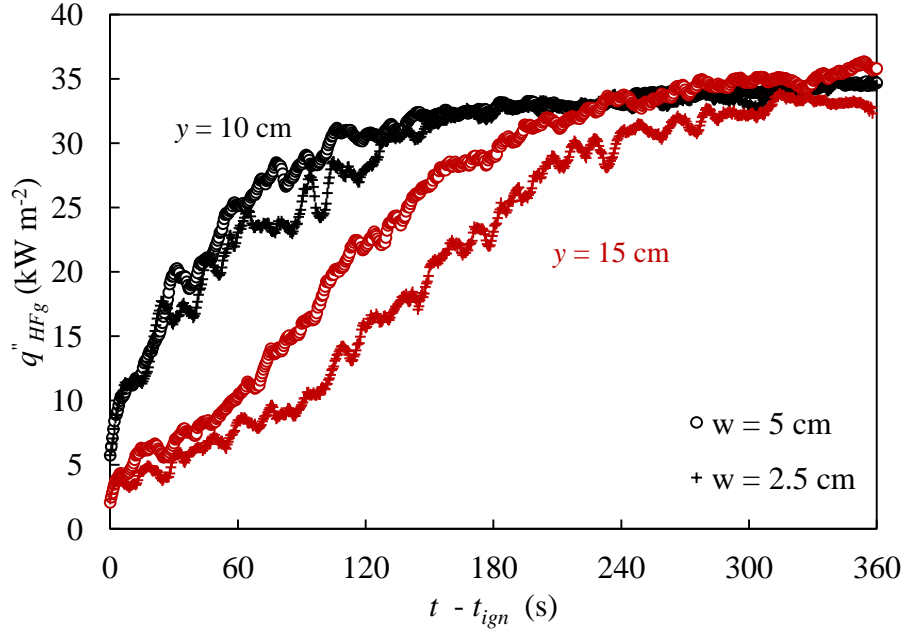


Figure 13. Measured q''_{HFg} at two locations, $y = 10$ and 15 cm, during upward flame spread over 2.5 and 5 cm wide samples of extruded PMMA

2.4.2.4 Flame Heat Transfer Mechanism – Convection vs. Radiation

It is important to note that q''_{HFg} is defined as total flame heat feedback measured by a water-cooled ($18\text{ }^{\circ}\text{C}$) heat flux gauge. Net heat flux into the surface of pyrolyzing PMMA samples, q''_{net} , will be different as it depends on the local surface temperature, T_{surf} , emissivity, ε , and absorptivity, α_{rad} , of the material. This net heat flux can be represented by the following expression:

$$q''_{net} = h_{flame}(T_{fl} - T_{surf}) + \alpha_{rad}q_{rad}^{flame} - \varepsilon\sigma T_{surf}^4 \quad \text{Equation 4}$$

where h_{flame} is a convection heat transfer coefficient, T_{fl} is an effective flame temperature, q_{rad}^{flame} is radiative heat flux from the flame to the front surface of the sample, and σ is the

Stefan-Boltzmann constant. To determine q_{net}'' based on measurements of q_{HFg}'' , this total heat flux must be decomposed to its convective and radiative components:

$$q_{HFg}'' = q_{conv}'' + q_{rad}'' \quad \text{Equation 5}$$

Beaulieu and Dembsey [63] have measured total and radiative heat flux from flames supported by PMMA, POM, and propylene gas burning in both the vertical and horizontal configurations. In their work, radiation heat transfer was determined in three ways – using a gauge with individual sensors for radiation and total heat flux, recessing a total heat flux gauge so as to protect it from hot flow gases and thus the convective component of heat flux, and by calculations based on measurements of flame emissivity and temperature – each of which was reported as consistent with the other two. Following their second approach, additional experiments were performed in our test apparatus to measure flame heat flux at $y = 3, 5, 8, 10, 12,$ and 15 cm with a gauge that was similarly recessed 0.64 cm into the sample's surface. When recessed, the heat flux gauge is initially shielded by a small, custom cut and fitted piece of Kaowool PM insulation that prevents the accrual of deposits on the surface of the gauge. When enough time has passed in the experiment such that q_{steady}'' should be observed at the gauge location, the insulation is removed, the sample is allowed to burn for an additional $10 - 20$ s, and then the flame is extinguished.

To remove the contribution that the hot insulation and PMMA surrounding the heat flux gauge has on recessed gauge measurements, the reported heat flux from these tests, $q_{recessed}''$, is calculated as the value obtained just prior to flame extinction minus the

value obtained after extinction once $\frac{d(q''_{HFg})}{dt} \geq -1 \text{ kW m}^{-2} \text{ s}^{-1}$; this measurement is highlighted in Fig. 14. Defined in this manner, $q''_{recessed}$ can be treated as purely radiation heat transfer from the flame to the recessed gauge. Dividing $q''_{recessed}$ by its radiative view factor, ϕ , yields an estimate of the radiative heat flux from the flame to the sample's surface, q''_{rad}^{flame} . This process was repeated three times each for all six measurement locations, y , of interest. A representative calculation for this process is found in the appendix where it is also shown that this method effectively eliminates the influence that the hot insulation (which forms the walls of the cavity surrounding the recessed heat flux gauge) may have on measurements.

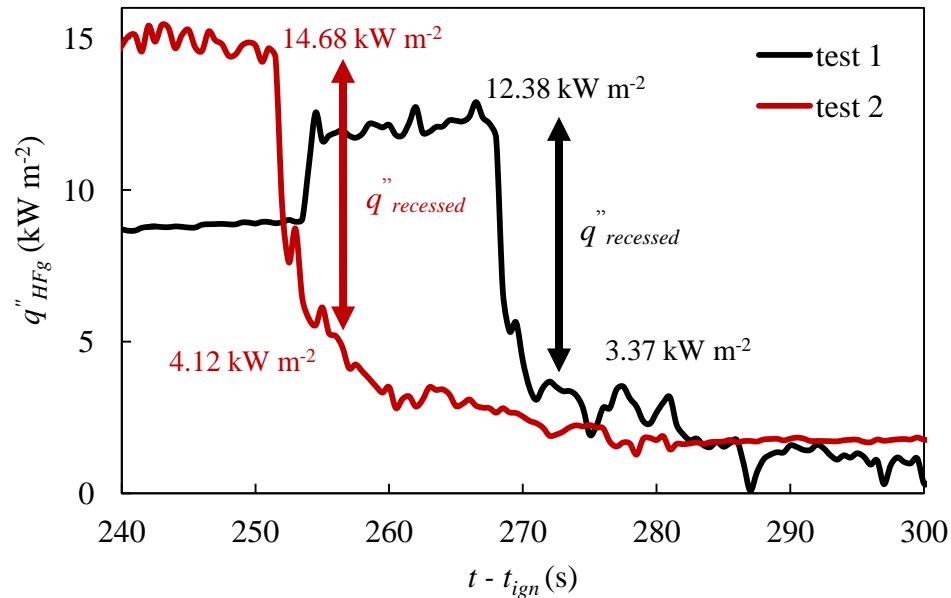


Figure 14. Representative tests showing recessed heat flux gauge measurements taken at $y = 10 \text{ cm}$ before and after extinction of a wall flame supported by extruded PMMA

ϕ was determined both experimentally and analytically² [50], with the experimentally determined value, $\phi = 0.77 \pm 0.05$, selected as more representative of actual test conditions³. This uncertainty is derived based on a propagation of errors arising from variations in flush and recessed measurements of radiative heat flux underneath the cone calorimeter. Based on these measurements, radiative fraction of total

heat flux – $q_{rad}^{\%} = 100 \times \left(\frac{q_{rad}^{flame}}{q_{steady}} \right)$ – is calculated at each measurement location, y , using

previously obtained measurements of $q_{steady}^{\prime\prime}$ (see Fig. 11) and recessed heat flux gauge

measurements as: $q_{rad}^{\%} = 100 \times \left(\frac{q_{recessed}^{\prime\prime} / \phi}{q_{steady}^{\prime\prime}} \right)$. Table 1 lists calculated $q_{rad}^{\%}$ at each

measurement location. In row 1 of this table, $q_{rad}^{\%}$ is calculated assuming that recessing the heat flux gauge by 0.64 cm completely eliminates non-radiative heat transfer from the flame (as suggested in the literature [63]); the values listed in this row are effectively upper limits for $q_{rad}^{\%}$.

² See appendix for a description of view factor calculations.

³ Analytical calculations of ϕ , when coupled with measurements of incident heat flux to the gauge when both flush and recessed, suggested a maximum possible radiative component that exceeded 80% of the total incident heat flux, the value reported for large scale, wholly turbulent flames [47].

Table 1. Calculated radiative fraction of total flame to surface heat flux, $q_{rad}^{\%}$

	y = 3 cm	y = 5 cm	y = 8 cm	y = 10 cm	y = 12 cm	y = 15 cm
Uncorrected						
for convection	$27 \pm 6\%$	$28 \pm 2\%$	$34 \pm 3\%$	$34 \pm 8\%$	$27 \pm 4\%$	$38 \pm 9\%$
Corrected for convection	$5 \pm 15\%$	$5 \pm 13\%$	$14 \pm 28\%$	$14 \pm 32\%$	$5 \pm 13\%$	$17 \pm 38\%$

Row 1 of this table lists values of $q_{rad}^{\%}$ calculated assuming zero convection heat transfer at the recessed gauge's surface; effectively this yields an upper limit for $q_{rad}^{\%}$.

Row 2 lists values of $q_{rad}^{\%}$ that are corrected to allow for reduced, though non-zero, convection heat transfer observed at the surface of the recessed heat flux gauge.

Current experimental observations suggest that, although reduced, non-radiative heat transfer is not entirely eliminated when the heat flux gauge is recessed. If purely radiative heat transfer is assumed in these recessed measurements, $q_{rad}^{\%}$ is calculated to be nearly 30 % at $y = 3$ and 5 cm; this is highly unlikely near the base of such a thin, laminar flame. Additionally, convection is evidenced by the deposits that form at the surface of the recessed heat flux gauge throughout experiments (hence the need to shield recessed gauges until just prior to measuring heat flux). It is possible that this was overlooked in Beaulieu and Dembsey's work because heat flux gauges used in their tests were cooled with 65°C water, which limits the formation of such deposits.

Further work was thus performed to develop an effective parameter, ϕ_{conv} , that represents the fraction of non-radiative heat transfer measured by a heat flux gauge that is recessed into a sample. ϕ_{conv} was determined experimentally by measuring the heat transfer from the thermal plume (beyond the flame tips) above a steady, well defined non-premixed propane flame as it burns against a vertically oriented sheet of Kaowool

PM insulation. In separate experiments, a heat flux gauge is mounted either flush or recessed (by 0.64 cm) into this layer of insulation. ϕ_{conv} is calculated as:

$$\phi_{conv} = \frac{\sum_{i=1}^N \frac{q''_{recessed,i}}{q''_{flush,i}}}{N} = 0.18 \pm 0.07 \quad \text{Equation 6}$$

Here, the subscripts ‘recessed’ and ‘flush’ denote the gauge’s position, i indicates the heat flux gauge reading at time $t = t_i$ seconds, and N is a large enough number such that variations in $\frac{q''_{recessed,i}}{q''_{flush,i}}$ due to noise in experimental measurements are minimized but still small enough such that secondary heating from the steadily warming insulation that surrounds the recessed gauge remains negligible. Based on these definitions for ϕ and ϕ_{conv} , the convective and radiative components of heat flux measured by the recessed gauge can be calculated as:

$$q''_{conv,recessed} = \phi_{conv} (1 - q_{rad}^{\%}) (q''_{steady}) \quad \text{Equation 7}$$

$$q''_{rad,recessed} = \phi (q_{rad}^{\%}) (q''_{steady}) \quad \text{Equation 8}$$

with

$$q''_{recessed} = q''_{conv,recessed} + q''_{rad,recessed} \quad \text{Equation 9}$$

In this system of equations $q_{rad}^{\%}$ at each position in the sample is the only unknown, with all other variables measured experimentally. Values of $q_{rad}^{\%}$ calculated in this manner are listed in the second row of Table 1 and plotted as a function of y in Fig. 15. A relationship between $q_{rad}^{\%}$ and distance from the base of the flame is defined by

combining these measurements with data reported by Tewarson and Ogden [47] whose work with large PMMA slabs indicates that, at heights above 1 m, radiation accounts for 80% of flame to surface heat transfer. Using these results, $q_{rad}^{\%}$ can be expressed as

$$q_{rad}^{\%} = \begin{cases} r_y y + r_0 & \forall y \leq 100 \text{ cm} \\ r_1 & \forall y > 100 \text{ cm} \end{cases} \quad \text{Equation 10}$$

with $r_y = 0.77 \text{ cm}^{-1}$, $r_0 = 3.2$, and $r_1 = 80 \%$. These results indicate that flame to surface heat transfer in this system is dominated by convection. This confirms previous observations by Fernandez-Pello and Hirano [21] who also reported that, in the laminar region of a wall flame, heat transfer from the flame occurs primarily by convection. As discussed in Section 3 of this manuscript, knowledge of this flame heat transfer mechanism allows for calculation of net flame heat transfer into the surface of pyrolyzing samples.

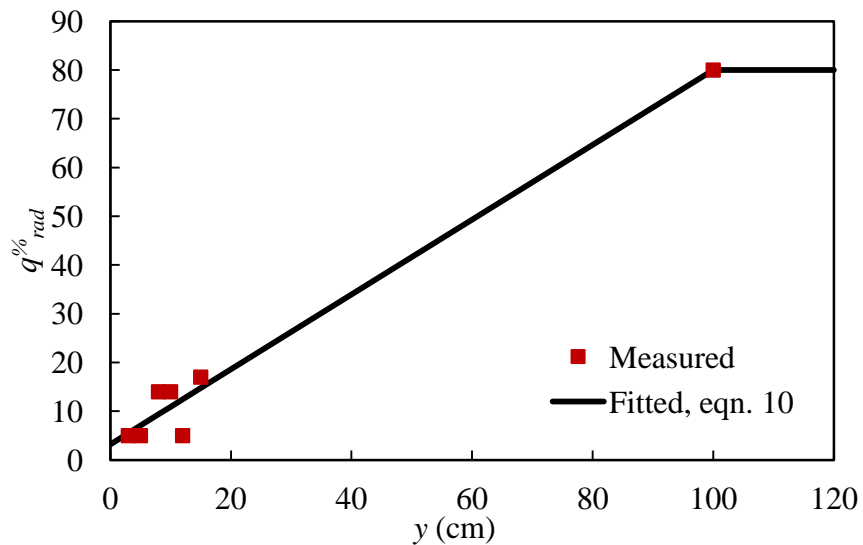


Figure 15. Radiative fraction, $q_{rad}^{\%}$, of extruded PMMA wall flames

2.5 Flame Heat Feedback Model Development

Defining a characteristic length scale (flame height) for this system is critical for accurate descriptions of the flame. In this work, flame height, y_f , is defined as the distance from the bottom of the flame to the highest position where measured flame heat flux reaches 97.5 % of q''_{steady} . The evolution of y_f with extruded PMMA mass loss rate is shown in Fig. 16; here, measurements are obtained from tests in which samples are ignited by the burner in its final configuration. Error bars in this figure represent two standard deviations of the mean calculated based on a propagation of errors resulting from variations in the time at which y_f reaches the measurement location during each test and scatter in measured sample mass loss rate (see Fig. 8). Note: the greater uncertainty observed at the lowest height, $y = 3$ cm, results from the rapid arrival of y_f at this location shortly after sample ignition. The maximum $\frac{dm'}{dt}$ recorded before a flame was observed – calculated as the average value measured in the 20 s immediately prior to sample ignition – is used to define $y_f = 0$. Sample mass loss rate shows a distinct increase at ignition (see Fig. 8), thus this average value serves as a reasonable lower bound for the critical ignition mass loss rate.

The observed dependence of y_f on $\frac{dm'}{dt}$ is well captured here by a single power law function:

$$y_f = a \left(\frac{dm'}{dt} \right)^P + b \quad \text{Equation 11}$$

where the units of y_f and $\frac{dm'}{dt}$ are [cm] and [$\text{g s}^{-1} \text{cm}^{-1}$] and a , P , and b are empirical constants equal to 87.7, 0.275, and -11.9, respectively.

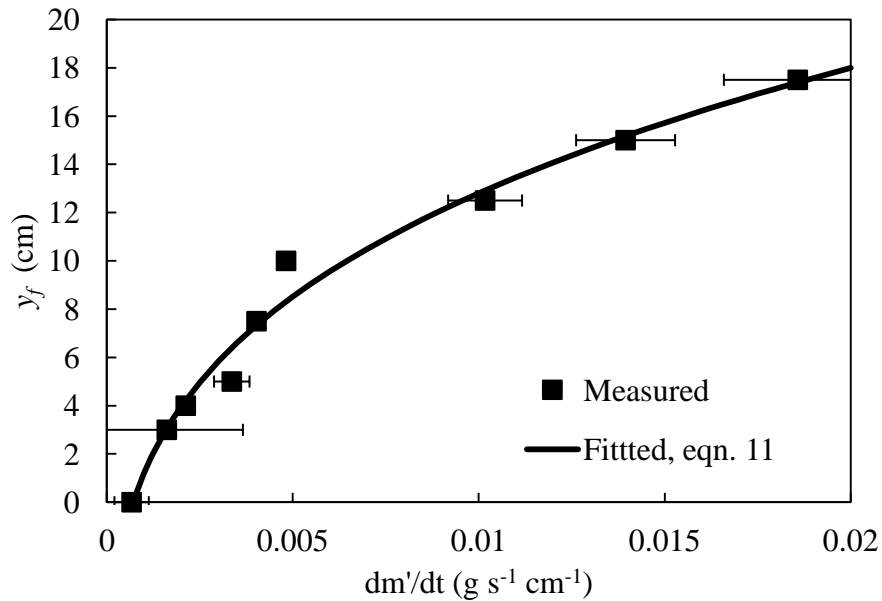


Figure 16. Flame height versus sample burning rate during upward flame spread over extruded PMMA

As seen in Fig. 17, the flame heat flux time dependencies, q''_{fitted} , obtained for different sample heights (different measurement locations, y) can be normalized by their corresponding q''_{steady} values as $q^* = \frac{q''_{fitted}}{q''_{steady}}$. These measurements are then converted to spatially resolved profiles by taking normalized heat flux readings from all measurement locations at a specific time, t , (vertical strips in Fig. 17) and plotting these values versus their respective heights. The results of this process are displayed in Fig. 18 at several representative times. In final analysis, this process was repeated at 5 s intervals throughout the duration of experiments thus providing the data set shown in the left graph of Fig. 19.

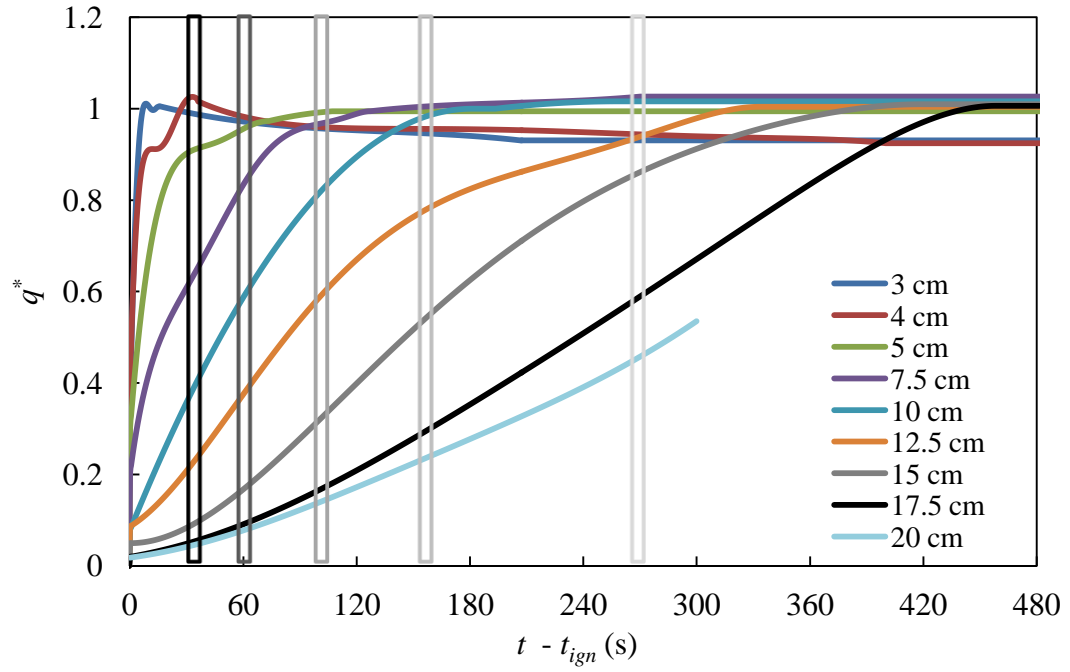


Figure 17. Evolution of flame to surface heat flux during upward flame spread over extruded PMMA

Note: legend entries indicate measurement location, y

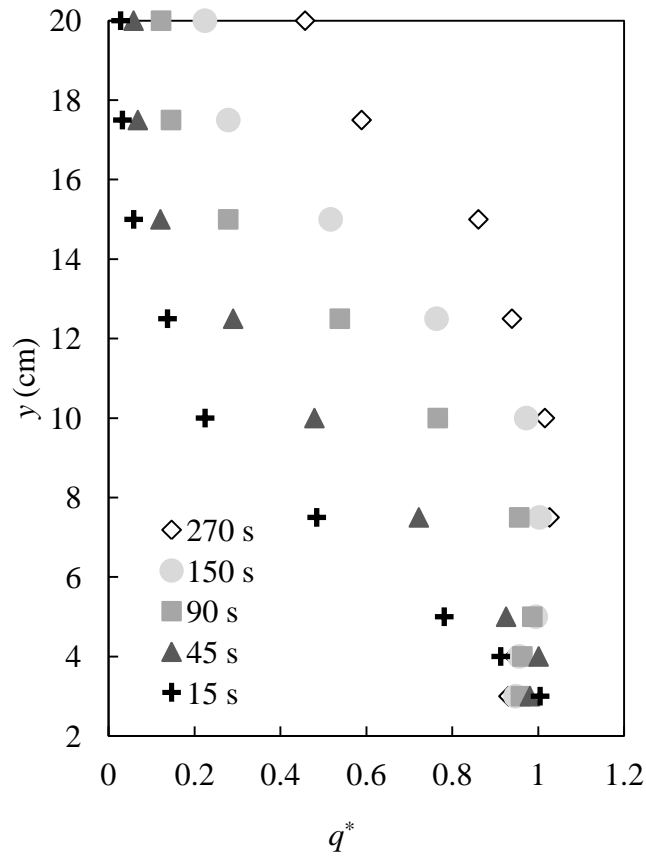


Figure 18. Normalized flame heat feedback profiles at $15 \leq t - t_{ign} \leq 270$ s

As shown in the right graph of Fig. 19 (open circles), a single characteristic heat feedback profile for the entire flame – representing measurements taken across the full height of samples from ignition until full sample involvement – becomes readily apparent when q^* is plotted against the normalized length scale,

$$y^* = \frac{(y + y_0)}{(y_f + y_0)} \quad \text{Equation 12}$$

where $y_0 = 2.2$ cm is an empirically derived constant.

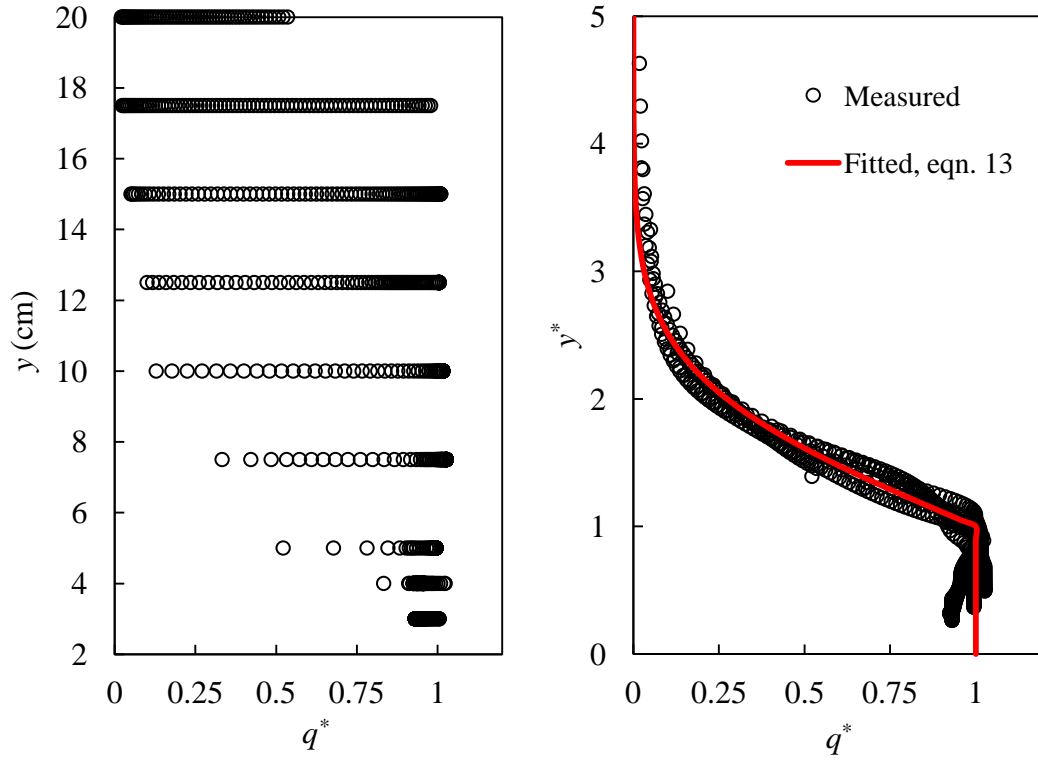


Figure 19. Normalized measured flame heat flux as a function of distance from the base of the sample

A single expression relating flame heat feedback as a function of material burning rate can thus be defined in the form

$$q''_{HFg} = q'' \left(y, \frac{dm'}{dt} \right) = \begin{cases} q''_{steady} , & y \leq y_f \\ (\alpha_f \times q''_{steady}) \left(e^{-\ln(\alpha_f) \times (y^*)^2} \right) , & y > y_f \end{cases} \quad \text{Equation 13}$$

where $\alpha_f = 1.54$ is an empirically derived constant obtained through fitting the data of the right graph of Fig. 19. Flame heat flux calculated using this expression can be

normalized as $q^* = \frac{q''_{HFg}}{q''_{steady}}$ to provide the 'Fitted' curve plotted in the right graph of Fig.

19. As seen here, eqn. 13 provides a constant heat flux in the continuous region of the

flame, $y \leq y_f$, and an exponentially decaying value farther downstream in the thermal plume, where the flame becomes intermittent. Collectively, eqns. 3, 11, 12, and 13 can be used to calculate a wall flame's entire heat feedback profile solely as a function of material burning rate.

As seen in Fig. 20, experimentally-measured and model-predicted q''_{HFg} show excellent agreement across the full length of the sample during all stages of the experiment. Fluctuations associated with flickering of the flame in the decay region (tail) of the heat feedback profile observed in experimental measurements are not accounted for in the model; however, overall behavior is well predicted with no systematic under- or over-prediction of the data. Total heat transfer to the material, $\int_{3cm}^{20cm} (q''_{HFg}) dy$, is calculated to within +/- 5% of measured values at any given time during experiments.

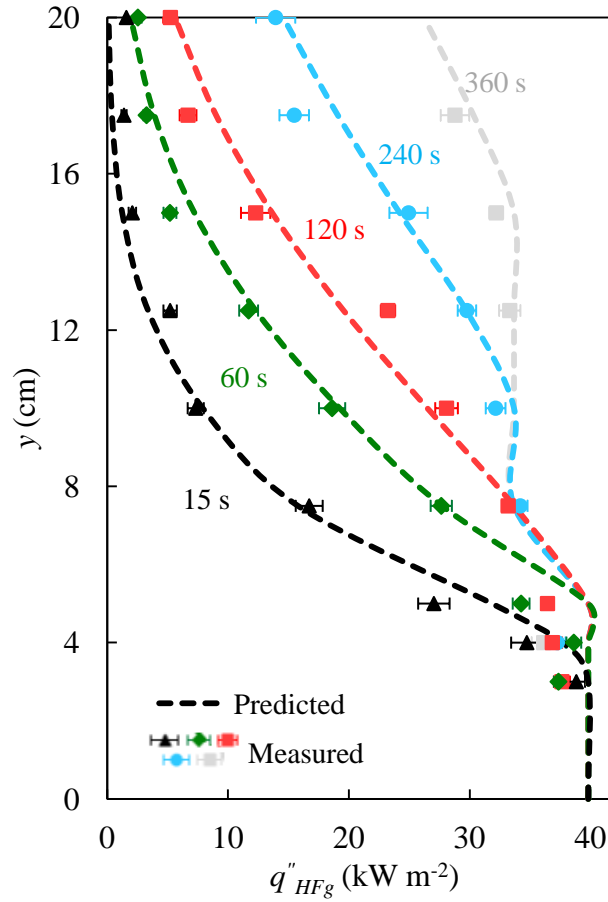


Figure 20. Comparison of experimentally-measured and model-predicted extruded PMMA heat feedback profiles during different stages of flame spread

Note: timestamps indicate time after sample ignition, $t - t_{ign}$.

3. Unified Model of Material Burning Behavior

3.1 Modeling Framework

A flexible computational solver, ThermaKin2D, was used in this study to calculate the response of PMMA – specifically, its temperature and mass loss rate – when subjected to external heat. ThermaKin2D computes the transient rate of gaseous fuel production by a one- or two-dimensional pyrolyzing object from fundamental physical and chemical properties of its constituents by solving a series of mass and energy conservation statements; conservation of momentum is introduced implicitly. In ThermaKin2D, materials are represented by a mixture of components. Each component is categorized as a solid, liquid, or gas and is defined by a set of temperature dependent properties. Up to 50 material components may be defined, each of which may interact physically and chemically in a series of reactions. Physical structures simulated in ThermaKin2D (material objects) are defined by an initial temperature and material composition, which may be spatially non-uniform. The key governing equations are summarized as follows:

$$\frac{\partial \xi_j}{\partial t} = \sum_{i=1}^{N_r} \theta_i^j r_i - \frac{\partial J_j^x}{\partial x} - \frac{\partial J_j^y}{\partial y} + \frac{\partial}{\partial x} \left(\xi_j \int_0^x \frac{1}{\rho} \frac{\partial \rho}{\partial t} dx \right) \quad \text{Equation 14}$$

$$r_i = A_i \exp\left(-\frac{E_i}{RT}\right) \xi_k \xi_l \quad \text{Equation 15}$$

$$J_g^x = -\rho_g \lambda \frac{\partial (\xi_g / \rho_g)}{\partial x} \quad \text{Equation 16}$$

$$\sum_{j=1}^N \xi_j c_j \frac{\partial T}{\partial t} = \quad \text{Equation 17}$$

$$\sum_{i=1}^{N_r} h_i r_i - \frac{\partial q_x}{\partial x} - \frac{\partial q_y}{\partial y} - \frac{\partial I_{ex}}{\partial x} + \frac{\partial I_{rr}}{\partial x} - \sum_{g=1}^{N_g} c_g \left(J_g^x \frac{\partial T}{\partial x} + J_g^y \frac{\partial T}{\partial y} \right) + c \rho \frac{\partial T}{\partial x} \int_0^x \frac{1}{\rho} \frac{\partial \rho}{\partial t} dx$$

$$q_x = -k \frac{\partial T}{\partial x} \quad \text{Equation 18}$$

$$\frac{\partial I_{ex}}{\partial x} = -I_{ex} \sum_{j=1}^N \alpha_j \xi_j \quad \text{Equation 19}$$

$$\frac{\partial I_{rr}}{\partial x} = \frac{\varepsilon \sigma T^4}{I_{ex}^0} \frac{\partial I_{ex}}{\partial x} \quad \text{Equation 20}$$

Eqn. 14 is the mass conservation statement of component j , formulated in terms of ξ_j , the concentration of the component expressed in the units of mass per unit volume. This statement accounts for all chemical reactions that produce or consume component j (term 1 on the right-hand-side), with reaction rates, r_i , defined by eqn. 15. In the absence of a second reactant in eqn. 15, ξ_l is set equal to 1. Terms 2 and 3 on the right-hand-side of eqn. 14 account for gas flow within the solid, the flux of which is defined by eqn. 16 (only gaseous components are considered to be mobile), and term 4 accounts for mass transfer associated with contraction or expansion of the material object. Eqn. 17 is the energy balance formulated in terms of temperature, T . On the right-hand-side of this equation, this balance includes: heat produced in chemical reactions (term 1); heat transfer due to conduction (terms 2 and 3), the flux of which is given by eqn. 18; radiative heat transfer from an external source (term 4), the absorption of which is defined by eqn. 19; re-radiation of energy to the environment (term 5), defined by eqn. 20; convection associated with gaseous component flow (term 6) and overall material

expansion/contraction (term 7). The last right-hand-side terms in the mass and energy conservation equations (eqns. 14 and 17) arise due to an application of the Eulerian (stationary) coordinate framework to a fluid that contracts or expands in response to density changes with respect to a specific plane (defined by $x = 0$).

The symbols in eqns. 14 - 20 are defined as follows. t is time; θ is a stoichiometric coefficient, which is negative when the corresponding component is a reactant and positive when it is a product. x and y are the Cartesian coordinates. ρ and c are density and heat capacity, respectively. h is the heat of reaction (positive when exothermic); A and E are the Arrhenius parameters; and R is the molar gas constant. λ , k , and α are gas transfer, thermal conductivity, and radiation absorption coefficients, respectively. ε is emissivity; σ is the Stefan-Boltzmann constant; and I_{ex}^0 is the external radiation through an object boundary (incident radiation minus reflected). Properties without a subscript indicate the property of mixture (rather than that of an individual component). The density of a mixture is defined as one divided by the sum of component mass fractions, each divided by its corresponding component density. The volumetric contribution of gaseous components to density can be scaled by a user defined factor, which can be related to the local composition. In all simulations performed in this study, gaseous components are set not to contribute to material volume. A detailed description of other aspects of ThermaKin2D physics and numerical solution methodology can be found elsewhere [30].

In numerical simulations of PMMA vertical burning and upward flame spread, the problem is treated as two-dimensional (i.e., burning behavior and flame heat flux are assumed to be perfectly uniform across the width of the sample). Heat flow is calculated

in both the x and y dimensions, while gas flow through the material object is only simulated in the x dimension – normal to the front (flame spreading) surface of the material. The insulation layer behind the PMMA sample is also included in the model. The insulation's top, bottom and back surfaces, as well as the top and bottom surfaces of PMMA, are treated as adiabatic. Boundary conditions at the PMMA front surface are defined to match the measured heat transfer conditions of either the propane burner or the wall flame supported by the material. This was made possible by further developing ThermaKin2D to include a flexible boundary condition formulation that is capable of providing a detailed analytical representation of the energy feedback from wall flames as based upon the flame model presented in Section 2 of this manuscript.

Here, both burner and PMMA flame heat flux, q''_{burner} and q''_{flame} , respectively, are assumed to be purely convective, as is often reported for laminar wall flames [21]. This assumption is supported by flame heat flux measurements presented in Section 2.4.2.4 of this manuscript, which showed that flame to surface heat transfer in this system is dominated by convection. Burner flame heat flux is defined as

$$q''_{burner} = h_{burner}(T_{fl}^{propane} - T_{surf}) \quad \text{Equation 21}$$

and prescribed start and end times that match the duration of burner exposure during experiments. In this expression, $T_{fl}^{propane}$ is the burner flame temperature and T_{surf} is the temperature of the surface of the material. The maximum value of $T_{fl}^{propane}$ is approximated as the adiabatic flame temperature [65] [66] of stoichiometric propane/air mixture, which has been calculated⁴ in this work using NASA's CEA solver [67] as 2265 K. The

⁴ See Appendix for input and output files detailing these CEA calculations

convective heat transfer coefficient, h_{burner} , is defined such that the calculated q''_{burner} is equal to the peak measured burner flame heat flux (see Fig. 4) when $T_{fl}^{propane} = 2265$ K and when T_{surf} equals the average temperature of water used to cool the heat flux gauge, $T_{HFg} = 291$ K. $h_{burner} = 0.025$ kW m⁻² K⁻¹ is kept constant across the sample's surface. Spatial variations in measured burner flame heat flux above the base of the sample are captured in the model by corresponding variations in the locally prescribed value of $T_{fl}^{propane}$. When calculating burner flame heat transfer into the surface of PMMA, in eqn. 21, T_{surf} is computed through eqns. 14 - 20.

Immediately after sample ignition, the external heat flux term of the propane burner is turned off to simulate burner removal. To simulate the presence of the wall flame supported by PMMA as it burns, an additional external heat flux term is specified when two criteria are reached: a critical mass flux of gaseous volatiles ($\dot{m}''_{crit} = 1$ g s⁻¹ m⁻² [68]) must be calculated in at least one point on the surface of the material object – the lowest position, y , where this is calculated defines the base of the flame – and calculated total mass flow out of the material object, $\frac{dm'}{dt}$, must be great enough such that eqn. 11 defines a positive flame height (i.e. $y_f > 0$). This critical ignition mass loss rate corresponds to the maximum $\frac{dm'}{dt}$ measured in experiments before ignition and steady flaming was observed (see discussion in Section 2.5 of this manuscript). PMMA wall flame heat flux is represented in ThermaKin2D as:

$$q''_{flame} = h_{flame} (T_{fl}^{PMMA} - T_{surf}) \quad \text{Equation 22}$$

The convection heat transfer coefficient, $h_{flame} = 0.0193 \text{ kW m}^{-2} \text{ K}^{-1}$, is defined as a constant value across the sample's surface such that q''_{flame} is equal to peak experimentally measured flame heat flux (q''_{steady}) when T_{fl}^{PMMA} equals the adiabatic flame temperature of PMMA, $T_{fl, adiabatic}^{PMMA} = 2363 \text{ K}$ and when $T_{surf} = T_{HFg} = 291 \text{ K}$. This adiabatic flame temperature is calculated⁵ assuming complete combustion of a stoichiometric mixture of methyl methacrylate (PMMA monomer) vapor in air to produce CO_2 and H_2O (no minor species) using a heat of combustion of PMMA equal to 25 kJ g^{-1} [69] and temperature dependent heat capacities as defined in the NIST Chemistry Webbook [70]. To account for spatial variations in q''_{steady} (see Fig. 11 and eqn. 3) the maximum value of T_{fl}^{PMMA} is defined as a function of this adiabatic flame temperature:

$$T_{fl, max}^{PMMA} = \begin{cases} T_{fl, adiabatic}^{PMMA} & \forall y \leq 5 \text{ cm} \\ 0.87 \times T_{fl, adiabatic}^{PMMA} & \forall y > 5 \text{ cm} \end{cases} \quad \text{Equation 23}$$

Lower flame heat fluxes (e.g. farther downstream in the unsteady regions of the flame) are captured by reductions in the locally prescribed value of T_{fl}^{PMMA} . By combining eqns. 13 and 22, net PMMA flame heat transfer is thus defined as:

$$q''_{flame} = q'' \left(y, \frac{dm'}{dt}, T_{surf} \right) = \begin{cases} h_{flame} (T_{fl, max}^{PMMA} - T_{surf}) & \forall y \leq y_f \\ h_{flame} \left(\alpha_f (T_{fl, max}^{PMMA} - T_{HFg}) e^{-\ln(\alpha_f) \times (y^*)^2} + T_{HFg} - T_{surf} \right) & \forall y > y_f \end{cases} \quad \text{Equation 24}$$

⁵ See Appendix for a detailed description of how these calculations were performed

Note that, in eqn. 24, replacing the material surface temperature (T_{surf}) with the temperature of the heat flux gauge ($T_{HFg} = 291$ K) effectively reduces this equation to the q_{HFg}'' model (eqn. 13). In ThermaKin2D, flame height, y_f , and the normalized flame length scale, y^* , are defined as per eqns. 11 and 12, respectively.

The development of the above expressions completes the set of equations needed to simulate upward flame spread in ThermaKin2D. This problem is solved numerically with calculations performed using a time step $\Delta t = 5 \times 10^{-3}$ s and a 5×10^{-5} and 1×10^{-3} m spatial discretization in the x (normal to heated sample's surface) and y (direction of flame spread) dimensions, respectively. Increasing or reducing these integration parameters by a factor of 2 did not produce significant changes in the results of simulations thus indicating convergence of the numerical solutions. Two-dimensional simulations of vertical burning and flame spread over 4 and 17.5 cm tall extruded PMMA samples required approximately 6 and 60 hours, respectively, of CPU time on a single core of a 2.0 GHz Intel Xeon processor.

3.2 Pyrolysis Model Parameterization

The pyrolysis model used to describe thermal degradation of extruded PMMA was parameterized using a combination of milligram-scale thermal analysis experiments [56] and gram-scale gasification tests [71] performed by colleagues in recent works. The results of the analysis of these experiments are summarized in Table 2. Extruded PMMA decomposition is represented here by a single first order reaction that yields one condensed phase and one gaseous product. The condensed phase product was produced in close to negligible mass yield, θ_{cond} . The derived kinetics (A and E) and thermodynamic parameters (h and c) were found to reproduce both thermogravimetric analysis (TGA, mass versus temperature) and differential scanning calorimetry (DSC, heat flow versus time) curves. Modeling of these experiments was performed using ThermaKin2D run in a thermally thin (non-dimensional) mode; see [56] for details of these simulations.

The density of PMMA was measured at 293 K. In the model, density was defined as a constant value, independent of temperature. Emissivity of extruded PMMA was assigned a value of 0.95, which is typical for common thermoplastics [72] [73]. By experimentally measuring transmitted radiation through a sample of PMMA of known thickness, the radiation absorption coefficient was determined to be approximately $\alpha = 1.94 \text{ m}^2 \text{ kg}^{-1}$. The thermal conductivity of extruded PMMA was assumed to be a piecewise-linear function of temperature and parameterized using an inverse modeling of temperature rise measured at the back of gasifying samples. Details of these exercises are described in a previous manuscript [71]. These properties are summarized in Table 2

alongside those of Kaowool PM insulation, which were obtained from the manufacturer and validated elsewhere [74].

The physical properties of the condensed phase product of extruded PMMA decomposition were assumed to be the same as those of the virgin polymer. The gas transfer coefficient for PMMA and its decomposition products was set at the upper bound of small molecule diffusivities, $\lambda = 2 \times 10^{-5} \text{ m}^2 \text{ s}^{-1}$ [75], to ensure that the flux of gas out of the sample was always equal to the rate of its production inside the sample (thus the concentrations of gas inside the sample was negligible). Kaowool PM was assumed to be impenetrable to gas flow. The heat capacity of the gaseous decomposition product of PMMA was assumed to be equal to $1.8 \text{ kJ kg}^{-1} \text{ K}^{-1}$, which is the mean heat capacity of a series of C1–C8 hydrocarbons at 400–500 K [70]. This heat capacity had a minor impact on simulation results because of the fast transport assumption implemented in the model

Table 2. Summary of extruded PMMA and Kaowool PM insulation material properties used in the pyrolysis model

Property	PMMA	Kaowool PM
ρ (kg m ⁻³)	1160	256
A (s ⁻¹)	$8.60 \times 10^{12} \pm 40\%$	N/A
E (kJ mol ⁻¹)	$188 \pm 2\%$	N/A
θ_{cond}	0.015	N/A
h (kJ kg ⁻¹)	$-846 \pm 5\%$	N/A
c (kJ kg ⁻¹ K ⁻¹)	$(0.60 + 0.0036T) \pm 11\%$	1.07
α (m ² kg ⁻¹)	1.94	1×10^3 (non-transparent)
ε	0.95	N/A
k (W m ⁻¹ K ⁻¹)	$T < 378 \text{ K: } (0.45 - 3.8 \times 10^{-4}T) \pm 10\%$ $T \geq 378 \text{ K: } (0.27 - 2.4 \times 10^{-4}T) \pm 13\%$	$0.052 - 4 \times 10^{-5}T + 1 \times 10^{-7}T^2$
λ (m ² s ⁻¹)	2×10^{-5}	0

This pyrolysis model parameterization was validated in a recent work [76] by simulating a series of radiation-driven gasification experiments in ThermaKin2D. In these tests, extruded PMMA samples were mounted on Kaowool PM insulation and exposed to either 20 or 60 kW m⁻² of radiant heat flux in an anaerobic environment. ThermaKin2D simulations results were compared to experimental-measurements of temperature rise at the back surface of samples and area-normalized sample mass loss rate, $\frac{dm''}{dt}$. From the beginning of radiant exposure until the sample had fully decomposed, model predictions of back surface temperature are excellent, matching experimental measurements at both radiant heat fluxes, on average, within 2%. Model-predicted $\frac{dm''}{dt}$ also closely follows experimentally measured mass loss dynamics, differing from observed values by less than 12%, on average, from the onset of mass loss until the time when 85% of sample mass has been consumed. At each incident heat flux, ThermaKin2D accurately predicts the time to onset of mass loss and peak mass loss rate; however, at the higher heat flux, it slightly over-predicts the time to peak mass loss rate.

3.3 Prediction of Vertical Burning and Upward Flame Spread

3.3.1 Steady Flaming Conditions

Before attempting a full simulation of upward flame spread, measured steady state flame heat flux, q''_{steady} , was validated. A comparison of wall flame heat fluxes measured in this work to literature values is not straightforward as considerable variations exist between values reported in different studies – e.g. two recent studies of PMMA report peak flame heat flux as low as 18 kW m⁻² [77] (measured just above the tops of 20 cm

tall samples) and as high as 75 kW m^{-2} [78] (used to characterize heat transfer across 10 cm tall samples in the UL-94 configuration). Such discrepancies may be partially explained by variations in measurement technique or device, terminology (e.g., net versus incident flame heat flux), and, especially in the case of small, primarily laminar flames (for which flame to surface heat transfer is dominated by convection) differences between sensor and sample surface temperature.

These complications were avoided in a study conducted by Ito and Kashiwagi [9] in which net heat transfer through a 30 cm tall burning PMMA slab was determined through holographic interferometry. By monitoring the temperature field within the material as it burned, net heat flux (conduction) through the material's top surface was quantified. The net heat flux measured under the steady region of the flame sheet in that work, $q_{net}'' = 28 \text{ kW m}^{-2}$, can be compared to values obtained here by ignoring in-depth radiative heat transfer and accounting for radiative heat losses using the assumption of surface absorption/emission:

$$q_{net}'' \approx h_{flame} (T_{fl,max}^{PMMA} - T_{surf}) - \varepsilon \sigma (T_{surf}^4 - T_{HFg}^4) \quad \text{Equation 25}$$

Setting $T_{surf} = 650 \text{ K}$, the pyrolysis temperature of PMMA [17], and all other parameters as determined in the current study, produces a value of q_{net}'' that is within 4 kW m^{-2} of that reported by Ito and Kashiwagi.

Measured steady state flame heat flux was further validated by comparing experimental measurements and ThermaKin2D calculations of mass loss rate as a flame spread over 4 cm tall, 5 cm wide PMMA samples burning in the vertical configuration. On average, y_f reached 3 and 4 cm, in 6 and 24 s, respectively, after sample ignition; consequently, these smaller samples faced primarily steady flaming conditions

throughout the length of experiments. Effectively, these tests validate q''_{steady} by deemphasizing the dynamics of flame spread and the importance of heat transfer downstream of y_f . For 4 cm tall samples, ThermaKin2D simulations were run for 480 s of modeling time; the predicted mass loss rate history is plotted in Fig. 21 (dashed line) along with experimentally measured $\frac{dm''}{dt}$. The modeling results show excellent agreement in terms of predicted ignition time and initial mass loss rate and its development throughout the test as the sample continues heating in depth.

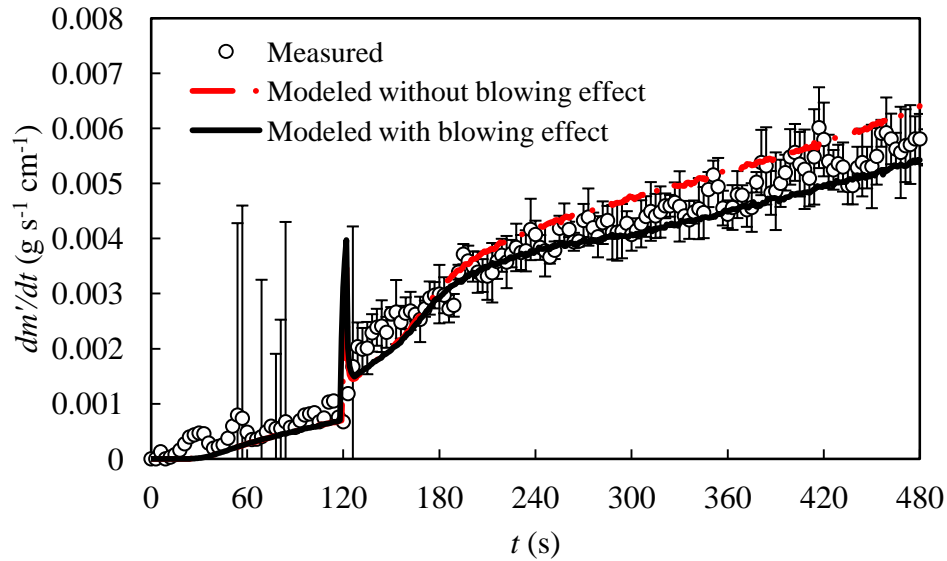


Figure 21. Experimentally-measured and model-predicted mass loss rate observed during vertical burning of 4 cm tall extruded PMMA samples

A closer review of flame heat flux measurements (see Fig. 10) reveals that, although y_f quickly reaches and advances above $y = 4$ cm, q''_{HFg} measured at this location decreases by roughly 3 kW m^{-2} (a 7.5 % decrease with respect to q''_{steady}) as the sample continues burning. This minor reduction in measured flame heat flux was observed at all $y \leq 5$ cm after y_f has advanced above the measurement location. This decrease in flame

heat flux occurs as the average mass flux in that region roughly doubles. One explanation for this correlation is a ‘blowing effect’ that pushes the flame sheet farther away from the sample’s surface as gaseous products of pyrolysis are expelled normal to this surface at an increasing velocity [40]. The impact of this ‘blowing effect’ is visualized in Fig. 22, which provides a side view of upward flame spread over a 10 cm tall PMMA sample. As seen here, not only does flame standoff distance (thickness) increase along the length of the flame but, as mass flux at the base of the sample increases throughout the duration of the test, the flame thickens there as well.

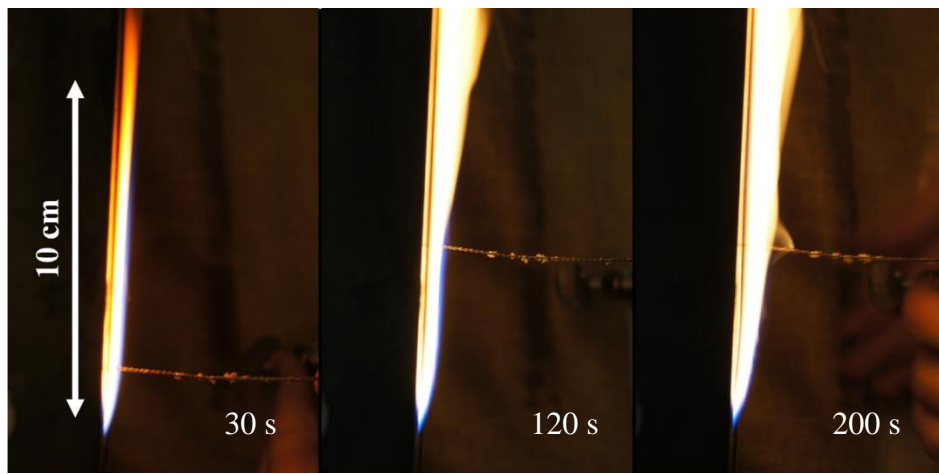


Figure 22. Side view images of upward flame spread over a 10 cm tall PMMA sample

Note: timestamps indicate time, $t - t_{ign}$, after sample ignition

This blowing effect has been observed in previous works by Ahmad and Faeth for both laminar [79] and turbulent [52] wall flames supported by fuel soaked wicks. In these works, their theoretical predictions of flame heat flux match experimental measurements within 15 – 20%; however, they report a reduction in measured flame to surface heat transfer in the pyrolysis region by a factor of two to three. Such a significant reduction is

not observed for any of the samples tested in our work and it cannot be validated to accurately predict material burning behavior in this system. Marxman [80] has proposed a blowing correction term in which flame heat flux in the pyrolysis region is scaled by the ratio $\frac{\ln(1+B)}{B}$, where B is the Spalding B number. This correction term was used in a recent work [81] that studied the burning rates (and flame standoff distances) of flat plates burning in various orientations. When applied to our work, this theory predicts a decrease in flame heat transfer and burning rate of PMMA wall slabs by a factor of two. Thus this theory appears to overestimate the impact of this blowing effect and consequently it does not show good agreement with our experimental measurements.

In our work, to account for this blowing effect, an additional time-dependent heat flux term is thus defined as a boundary condition in ThermaKin2D simulations⁶ to provide the measured (up to 3 kW m^{-2}) reduction in flame heat flux at $y < 5 \text{ cm}$. The difference between the two simulation cases is slight (see Fig. 21); however, by accounting for this measured reduction in flame heat flux, model predictions of sample mass loss rate better retain their similarity to measured values throughout the length of the experiment. Overall, these results confirm the accuracy of measured values of q''_{steady} and their parameterization in ThermaKin2D.

⁶ See appendix (Section A 6.2) for an explicit definition of this heat flux term.

3.3.2 Upward Flame Spread

A 17.5 cm tall material object was defined in ThermaKin2D to test the model's ability to predict upward flame spread over PMMA, from preheating and ignition to total sample involvement. To account for soot deposition beneath the flame at the material's front surface, PMMA was set to be non-transparent by prescribing a very high absorption coefficient ($\alpha = 1 \times 10^4 \text{ m}^2 \text{ kg}^{-1}$) for $y > 4$ cm. The emissivity of PMMA was not changed as it approximately equals to that of soot [82]. Simulations of flame spread over 17.5 cm tall samples were conducted with and without a heat flux term to account for the 'blowing effect'; this term was defined as a time dependent boundary condition identically as in the simulations of 4 cm tall samples.

As seen in Fig. 23, model predictions of sample burning behavior are in good agreement with experimentally observed results, especially when the 'blowing effect' correction is applied. Time to ignition and initial mass loss rate are both well predicted and model calculations of the rate of rise and peak mass loss rate also show a reasonable agreement with the experimental measurements. As flame to surface heat transfer is the primary controlling mechanism of upward flame spread at this length scale, and because the magnitude of q''_{steady} and its method of parameterization in ThermaKin2D have been validated, the similarity of measured and predicted mass loss rates indicates that the overall formulation of the flame heat feedback model developed here and represented by eqns. 11, 12, 23, and 24 is valid.

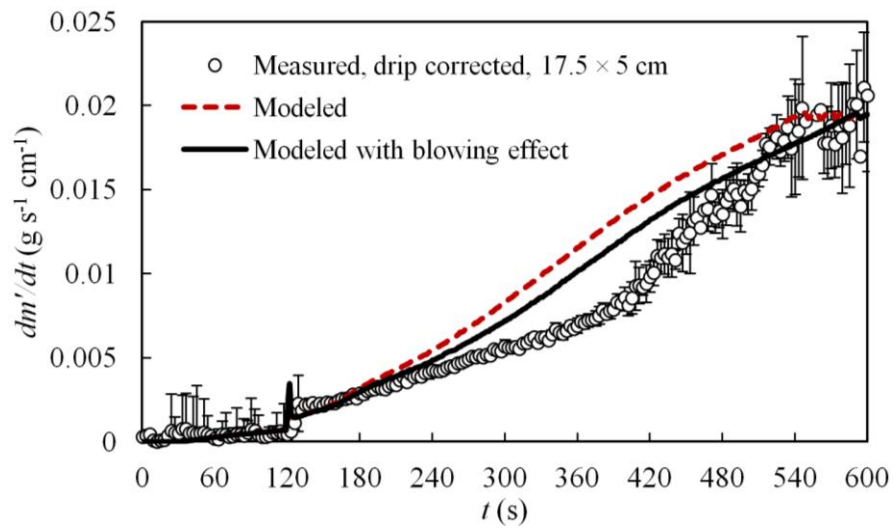


Figure 23. Experimentally-measured and model-predicted mass loss rate during upward flame spread over 17.5 cm tall extruded PMMA samples

3.4 Analysis of Factors Affecting Flame Spread Predictions

Although a good overall agreement exists between experimentally observed and model-predicted $\frac{dm'}{dt}$, during the middle stages of flame spread tests on 17.5 cm tall PMMA samples, our model overestimates the experimental measurements (see Fig 23). One assumption that may contribute to this discrepancy is an assignment of the adiabatic (effectively, maximum possible) flame temperature to $T_{fl,max}^{PMMA}$ for $y \leq 5$ cm. As seen in Fig. 24, a reduction in this maximum temperature by 200 K (accompanied by recalculation of other model parameters – e.g. h_{flame} – to ensure that the model still reproduces measured q''_{HFg}) improves the average agreement between numerical simulations and experimental results; however, this change would result in slightly less accurate predictions of the burning behavior of 4 cm tall samples in response to steady flaming conditions. Additionally, while this change lowers the predicted $\frac{dm'}{dt}$ curve, it does not fundamentally alter its shape such that ThermaKin2D predictions significantly better capture experimentally measured burning behavior of 17.5 cm tall samples. In each of the simulations shown in Fig. 24, and all those that follow, the ‘blowing effect’ is accounted for as described previously.

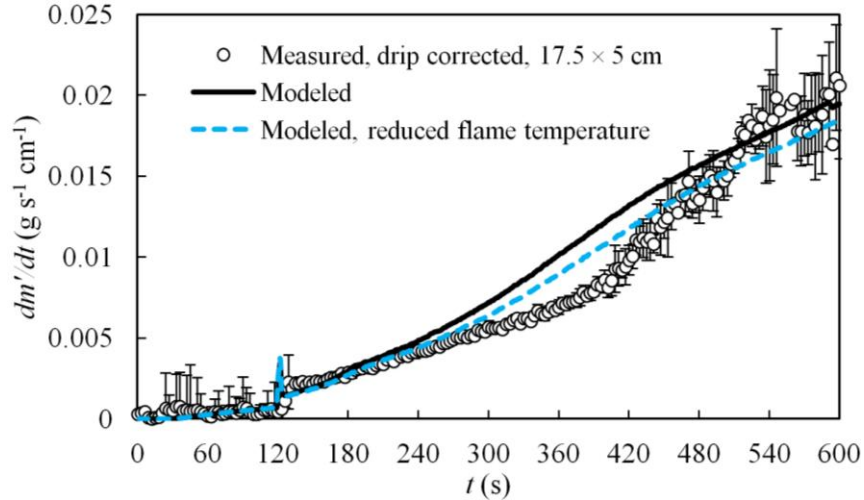


Figure 24. Impact of assumed maximum flame temperature on ThermaKin2D predictions of mass loss rate during upward flame spread over PMMA

Although a correction has already been applied to remove the impact of drip pool burning on $\frac{dm'}{dt}$ measurements, one behavior that is present in experiments but not accounted for in the model is the downward flow of extruded PMMA. This flow is not observed on smaller samples, hence its effects were not simulated for 4 cm tall samples of PMMA; however, this behavior is significant for larger samples. As 17.5 cm tall samples continue heating throughout each test, a viscous layer of polymer melt forms and flows downwards at the sample's front surface, carrying with it the energy provided by the flame. This exposes a cooler layer of PMMA that must be heated further before it can begin pyrolyzing, effectively slowing progression of the pyrolysis front and limiting the rate of rise of sample mass loss rate. As the flame spreads and the sample continues heating in depth, its entire front surface eventually begins pyrolyzing, despite this continued melt flow. This observation may explain why, at late stages of experiments on 17.5 cm tall samples, experimental and model-predicted $\frac{dm'}{dt}$ converge (see Fig. 23).

The melt flow rate (along the sample surface) was estimated by measuring the rate, $\frac{dm'_{drip}}{dt}$, at which PMMA dripped from the bottom of the sample to the mass balance below. To account for polymer melt flow in ThermaKin2D, an additional mass flux term was prescribed for $y > 4$ cm at the sample's front boundary:

$$J_{flow} = u \exp\left(-\frac{v}{RT_{surf}}\right) \quad \text{Equation 26}$$

where u and v are empirical constants that relate the mass flux of non-decomposed PMMA out of the sample to the material's surface temperature (T_{surf}). Removal of PMMA in this manner, before it can degrade to produce gaseous volatiles contributing to $\frac{dm'}{dt}$, provides a first order representation of the effects of melt flow. To parameterize

eqn. 26, $\frac{dm'_{drip}}{dt}$ was normalized by pyrolysis height, which was estimated throughout the length of experiments by video review. This calculation yielded a single value of $J_{flow} \approx 6 \times 10^{-4} \text{ g s}^{-1} \text{ cm}^{-2}$, which represents the observed time-averaged flux of polymer melt out of the pyrolysis region of burning samples. The constants in eqn. 26 were subsequently defined as $u = 600 \text{ g s}^{-1} \text{ cm}^{-2}$ and $v = 80 \text{ kJ mol}^{-1}$ such that $J_{flow} = 6 \times 10^{-4} \text{ g s}^{-1} \text{ cm}^{-2}$ when $T_{surf} = 700 \text{ K}$ (approximate burning PMMA surface temperature predicted in the flame spread simulations) and $J_{flow} = 6 \times 10^{-5} \text{ g s}^{-1} \text{ cm}^{-2}$ (factor of 10 lower) at $T_{surf} = 600 \text{ K}$. The latter temperature value was proposed by Kandola et al. [83] as the onset of PMMA dripping.

As seen in Fig. 25, inclusion of this flow term improves the average agreement between ThermaKin2D simulations and measured results. However, as was the case when reducing the flame temperature, it does not fundamentally alter the shape of the

predicted $\frac{dm'}{dt}$ curve such that it completely matches experiments. This exercise highlights the importance of accounting for the energy carried away by melt flow and shows that the simplified method by which this behavior was implemented in the current simulations does not fully capture its dynamics.

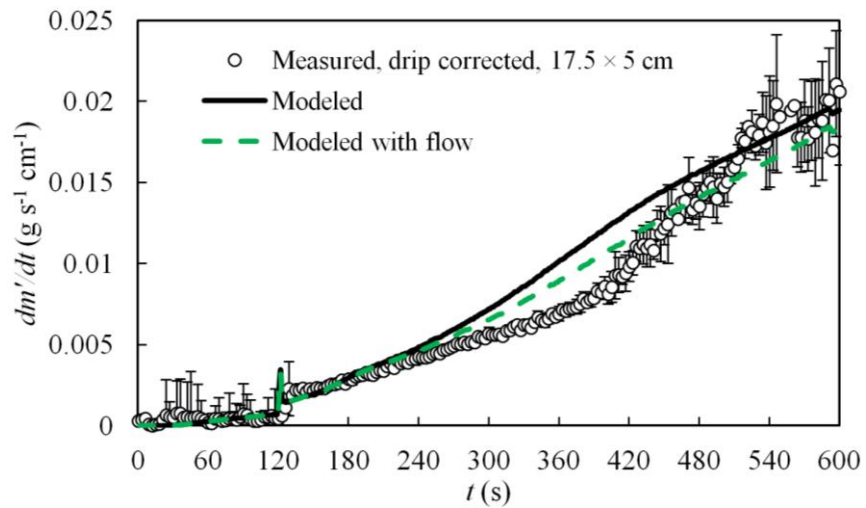


Figure 25. Impact of inclusion of melt flow on ThermaKin2D predictions of mass loss rate during upward flame spread over PMMA

4. A Generalized Wall Flame Model

4.1 Scaling Approach

The flame model developed in Section 2 of this manuscript has been shown to accurately predict the entire heat feedback profile of an upward spreading wall flame; however, it has one key limitation – it can only be applied to PMMA. Generalizing this model such that it can predict the behavior of flames supported by a wide range of materials represents a significant advancement in its utility. In a recent review of surface flame spread [84], Hasemi reports that wall flame length is generally expressed as a function of heat release rate. Numerous works [29] [35] [39] [40] [44] offer examples of such flame models. Our flame model requires a single input to calculate flame heat feedback – sample mass loss rate, which is directly related to heat release rate by a material's heat of combustion. Generalization of this flame model is thus attempted through scaling of the expressions that calculate flame height and maximum flame temperature on the basis of the heat of combustion of the gaseous volatiles produced by a pyrolyzing solid, ΔH_c^{MATL} .

A theoretical basis for the dependence of flame height on heat release rate was developed by Heskestad [85]. Building upon an existing capability to predict maximum gas velocities in buoyancy controlled turbulent diffusion flames, this work presented a flame height model based on a careful analysis of mass, momentum, and energy flux in the reacting part of fire plumes. Using this foundation, Zukowski et al. [86] analyzed the heights of diffusion flames supported by natural gas burners between 10 and 50 cm in diameter which supported heat release rates ranging from 10 to 200 kW. The results of this study validated the previously defined dependence of flame height on heat release

rate. Around the same time, Delichatsios [43] developed an integral model capable of calculating turbulent flows, including flame heights, of burning walls. This work further validated the dependence of flame height on heat release rate, not just for unconfined fire plumes but for wall fires as well.

Following this approach, our flame height expression is re-expressed here as:

$$y_f = a \left(\frac{\Delta H_c^{MATL}}{\Delta H_c^{PMMA_{EXT}}} \frac{dm'}{dt} \right)^P + b \quad \text{Equation 27}$$

Here, ΔH_c^{MATL} represents the heat of combustion of the material of interest (that which is being modeled) and $\Delta H_c^{PMMA_{EXT}}$ represents the heat of combustion of extruded PMMA, the material for which this flame model was originally developed. It is important to note that, effectively, the constant a in eqn. 27 implicitly includes $\Delta H_c^{PMMA_{EXT}}$ thus scaling the flame height expression by the ratio $\frac{\Delta H_c^{MATL}}{\Delta H_c^{PMMA_{EXT}}}$ accounts for the increase or decrease in fire size supported by materials that are more or less energetic than extruded PMMA.

In our generalized wall flame model, ΔH_c^{MATL} is also used to calculate $T_{fl,adiabatic}^{MATL}$ the adiabatic flame temperature of the material of interest, which is used to determine peak flame heat flux as per eqns. 28 and 29:

$$T_{fl,max}^{MATL} = \begin{cases} T_{fl,adiabatic}^{MATL} & \forall y_{eff} \leq 5 \text{ cm} \\ 0.87 \times T_{fl,adiabatic}^{MATL} & \forall y_{eff} > 5 \text{ cm} \end{cases} \quad \text{Equation 28}$$

$$q''_{flame} = q'' \left(y_{eff}, \frac{dm'}{dt}, T_{surf} \right) = \begin{cases} h_{flame} (T_{fl,max}^{MATL} - T_{surf}) & \forall y_{eff} \leq y_f \\ h_{flame} \left(\alpha_f (T_{fl,max}^{MATL} - T_{HFg}) e^{-\ln(\alpha_f) \times (y^*)^2} + T_{HFg} - T_{surf} \right) & \forall y_{eff} > y_f \end{cases} \quad \text{Equation 29}$$

Note: eqns. 28 and 29 are identical to eqns. 23 and 24 except for the replacement of $T_{fl,adiabatic}^{PMMA}$ by $T_{fl,adiabatic}^{MATL}$ and y by y_{eff} .

When our flame model was originally developed, experimentally observed dripping of extruded PMMA samples was considered minimal and thus not assumed to impact flame heat feedback. However, a closer review of sample behavior in these tests reveals that the base of the flame moves downwards throughout the duration of experiments. Thus, although the original model captured experimentally measured heat feedback of extruded PMMA flames very well, its predictions of flame heat flux at a given location, y , were implicitly coupled with the downward movement of the base of the flame as this material burned. Consequently, without adjustment, the predictions of this original model would be inaccurate for any material for which the base of the flame does not move identically as during these tests on extruded PMMA.

Throughout the duration of tests in which the base of the flame steadily moves downwards, the heat flux gauge – which is located at a fixed position, y – effectively measures flame heat feedback at a position that is progressively farther from the base of the flame. To account for this, the location of the gauge with respect to the base of the flame, y_{eff} , is calculated as

$$y_{eff} = y - y_b \quad \text{Equation 30}$$

where y_b represents the location of the base of the flame. With this definition, flame height, y_f , is redefined here as per the procedure presented in Section 2.5 of this manuscript as the highest position, y_{eff} , where measured flame heat flux reaches 97.5 % of q''_{steady} .

4.2 Material Selection

To develop our generalized wall flame model, sample mass loss rate and flame heat feedback during upward flame spread and the heat of combustion of seven polymeric materials, two of which are glass reinforced composites, are measured experimentally. Each material is widely used in industry and, collectively, they present a diverse range of burning behaviors including dripping, polymer melt flow, sample burnout, and heavy soot and solid residue formation. All samples were purchased in the form of 6.0 mm +/- 0.5 mm thick sheets, which are free of any dyes or flame retardants. All materials were stored in a desiccator in the presence of Drierite for a minimum of 24 hours prior to use in any experiments. A summary of manufacturer and distributor information for each of these seven materials is provided in Table 3. Note: to disambiguate between cast PMMA, which was studied here during model generalization experiments because it does not support dripping or polymer melt flow, and extruded PMMA, the material for which this flame model was originally developed, the subscripts 'CAST' and 'EXT' are used throughout the remainder of this manuscript.

Table 3. Materials used to obtain data for flame model generalization

Material	Manufacturer	Distributor
Acrylonitrile Butadiene Styrene (ABS)	Westlake Plastics	Modern Plastics
Fiberglass Reinforced Polyester Resin (FRP)	Prepared In-House	Fibre Glast
High Impact Polystyrene (HIPS)	Spartech Plastics	Professional Plastics
Polybutylene Terephthalate (PBT)	BASF	BASF
Cast Poly(Methyl Methacrylate) (PMMA_{CAST})	Evonik Industries	Evonik Industries
Extruded Poly(Methyl Methacrylate) (PMMA_{EXT})	Evonik Industries	US Plastic Corporation
Polyoxymethylene (POM)	Ensinger	Curbell Plastics
Polypropylene (PP)	Compression Polymers Corporation	US Plastic Corporation

The PBT and FRP samples tested in this work are both glass-reinforced composite materials. PBT samples were produced by BASF in the form of 14.5 x 5 cm slabs consisting of 25% (by mass) chopped glass fibers. FRP samples were prepared in-house using wax-free, general purpose unsaturated polyester (UP) resin and a plain weave fiberglass fabric. Both the UP resin and fiberglass fabric were purchased from Fibre Glast. The fiberglass used to reinforce FRP samples is style 7500 – indicative of a 10 oz fabric layer with a specified thickness of 0.0154 inches [87]. The exact composition of this UP resin is not provided by the distributor as it is considered proprietary information. In this work, UP resin is thus assumed to be representative of the general composition and standard fabrication process of the most common general purpose UP resin [88]. This polymer system consists of phthalic anhydride, maleic anhydride, and styrene, which polymerizes into a thermosetting network of polyester chains with polystyrene cross-

links. The resin is formulated to cure when combined with methyl ethyl ketone peroxide (MEKP), a commonly used initiator, in the amount of 1.25% of the mass of the resin. Here, FRP samples were prepared using a hand-layup method at an approximate composition ratio of 50 % (by mass) of resin to glass. 16 layers of fiberglass fabric and polyester resin were applied, one at a time in alternation, to achieve a sample thickness of approximately 6 mm. The orientation of the fabric was not varied between alternating layers to facilitate the consistent behavior of layers within the composite. FRP samples were allowed to cure at room temperature for twenty-four hours followed by a post-cure in an oven for one hour at 343 K.

4.3 Methods

4.3.1 Upward Flame Spread Experiments

Each of the materials listed in Table 3 – ABS, FRP, HIPS, PBT, PMMA_{CAST}, POM, and PP – support stable, self-sustaining flames that are uniform across their width (i.e. two-dimensional). Detailed measurements of flame heat flux and sample mass loss rate during upward flame spread over these materials were thus obtained in independent tests conducted identically as described in Section 2.2 of this manuscript. All materials were ignited using the non-premixed propane burner in its final configuration, which was applied just long enough for sustained, uniform ignition of each sample along its bottom edge. In these tests, samples were allowed to burn until completely involved (i.e. pyrolysis observed across their entire surface), until steady state measurements of flame heat flux were recorded for at least 60 s, or until secondary burning behavior (e.g. polymer melt flow, sample burnout, or significant residue formation at the sample's

surface) impacted measured material burning behavior. This cutoff time is explained in detail, as needed, in subsequent sections of this manuscript.

Previously, it has been shown (Fig. 7) that the burning dynamics controlling the development of the pyrolysis zone is not altered between PMMA_{EXT} samples of different heights, provided that they are ignited and a flame is allowed to spread across their surfaces identically. This result means that $\frac{dm'}{dt}$ measured at a single height, that of the largest samples tested, can be used to accurately characterize the mass loss rate of all smaller samples (up to the point in time when the surface of the smaller samples becomes fully involved). This observation of similar burning is verified here by an additional series of mass loss rate experiments conducted on ABS and PP samples ranging in height between 7 and 15 cm tall.

Throughout the duration of experiments, each of the seven materials tested here supports flames that are primarily uniform across their width; that is, across the width of the flame, burning behavior is fairly uniform. However, due to burnout along their base and sides, FRP samples support an increasingly narrow flame as tests progress. To correctly calculate $\frac{dm'}{dt}$ during FRP experiments, measured mass loss rate is therefore normalized at each time step by the maximum flame width observed at the corresponding time in the test. FRP flame width is determined throughout the duration of each experiment by subsequent video review. For all seven materials, mass loss rate tests are repeated three times each for all sample heights of interest. Signal noise is reduced by applying a 5 s running average to $\frac{dm'}{dt}$ measurements from each individual test;

measurements from repeated tests are averaged together and this combined dataset is further smoothed using a 5 s running average prior to further analysis.

For each material, spatially resolved measurements of q_{HFg}'' are obtained by preparing samples of different heights (between 5 and 15 cm), igniting them identically, and measuring flame heat flux at the top of each sample, as a flame spreads across their surface. Heat flux experiments are repeated three times for each sample height of interest. Measurements from repeated tests are averaged together and this combined dataset is smoothed using a 5 s running average prior to further analysis. Heat flux measurements recorded at all sample heights are related to the measured mass loss rate of the largest samples tested. This process is described in further detail in Section 4.4 of this document.

HIPS and ABS flames produce a significant amount of soot. In upward flame spread experiments, flames are in direct contact with the surface of the virgin material, downstream of the pyrolysis zone. Thus, as ABS and HIPS samples burn in the vertical configuration, soot from their flames continuously deposits across the surface of the material, forming a layer that can grow several millimeters thick. A detailed description of this soot deposition and its impact on material burning behavior is provided in Section 4.4.1.3 of this document. By the end of tests on each of these two materials, a similar and significant residue layer also formed on the surface of the heat flux gauge; this layer produced a noticeable decrease in measured flame heat flux. In several tests, the growth of deposits on the gauge's front surface was partially mitigated by using 75 °C water to cool the heat flux gauge; however, a 1 mm thick residue layer still formed.

To more effectively protect the heat flux gauge from deposits, at each measurement location of interest, an additional series of experiments was performed in

which the gauge was shielded using a thin, custom cut and fitted piece of insulation. This insulation shield prevented the buildup of a residue layer on the gauge without affecting material burning behavior. In separate tests, this shield was removed at different times after sample ignition and a ‘clean gauge’ measurement of flame heat flux was recorded as the maximum value measured within 10 s of shield removal. Unshielded heat flux measurements of ABS and HIPS flames are analyzed only during the time period before soot deposition had a notable impact on gauge readings – this cutoff is defined as the latest time in experiments when measured flame heat flux increases by at least $0.05 \text{ kW m}^{-2} \text{ s}^{-1}$. At later times in the experiment, a curve representing flame to surface heat flux that would be measured in the absence of soot deposition is defined by interpolating between the last measurements recorded before soot deposits impacted unshielded measurements and clean gauge readings recorded in shielded tests.

As HIPS, PMMA_{EXT}, POM, and, PP samples burn, the base of the flame moves downward due to the downward flow and continued burning of the polymer as it softens and drips. Conversely, as FRP and PBT samples burn, the base of the flame moves upwards due to burnout of the material near its base. When our flame model was originally developed for PMMA_{EXT}, the location of the base of the flame, y_b , was assumed to remain fixed at $y = 0$ throughout the duration of experiments. This assumption had no impact on the accuracy of model predictions of PMMA_{EXT} flame heat flux at a fixed location, y , because the model implicitly included the effects of experimentally observed changes in y_b for this material. However, in order to compare model-predicted and experimentally-measured flame heat fluxes for a range of materials – each of which supports different behavior of the base of the flame – y_b must be

carefully tracked throughout experiments on each material. In this analysis, y_b is defined as the lowest position of the continuous flame sheet that is at least as wide as 60% of the maximum flame width. By analyzing videos of each test, y_b was measured throughout the length of all mass loss rate and heat flux experiments and a function was defined that describes the average time-dependent position of the base of the flame supported by each material tested here. These measurements were used to redefine our flame height model such that it can account for movement of the base of the flame.

4.3.2 Heat of Combustion Measurements

In this study, the heat of combustion of the gaseous volatiles produced by eight polymeric materials – ABS, FRP, HIPS, PBT, PMMA_{CAST}, PMMA_{EXT}, POM, and PP – is determined experimentally on the basis of oxygen (O₂) consumption calorimetry experiments [89] conducted in a Govmark CC1 Cone Calorimeter [3]. Initial measurements indicated that heat of combustion measurements obtained in cone calorimeter tests may be sensitive to material burning orientation. Thus, in this work, two series of experiments are performed in the cone calorimeter on materials burning either vertically or horizontally. Tests are repeated in each orientation both with and without the application of an external heat flux of $q_{ext}'' = 30 - 50 \text{ kW m}^{-2}$ to the sample's surface. Repeating heat of combustion tests in both the presence and absence of external heating is necessary because in standard tests [3] (and for most values reported in the literature) an external heat flux is used, however, an external heat flux is not applied during most of the flame spread experiments conducted in this work. In cone calorimeter experiments,

carbon monoxide (CO) and carbon dioxide (CO₂) concentrations (in percent by volume) in the sample exhaust stream are also measured.

Fig. 26 illustrates each of these four burning configurations and highlights the naming convention used for each test measurement; here, A_s represents sample surface area exposed to the flame. When samples are exposed to an external heat flux during cone calorimeter testing, heat of combustion measurements are denoted by the subscript “heat”. Heat of combustion measurements obtained in tests without an external heat flux are denoted by the subscript “0”. Tests conducted in the horizontal and vertical orientations are denoted by the subscripts “H” and “V”, respectively.

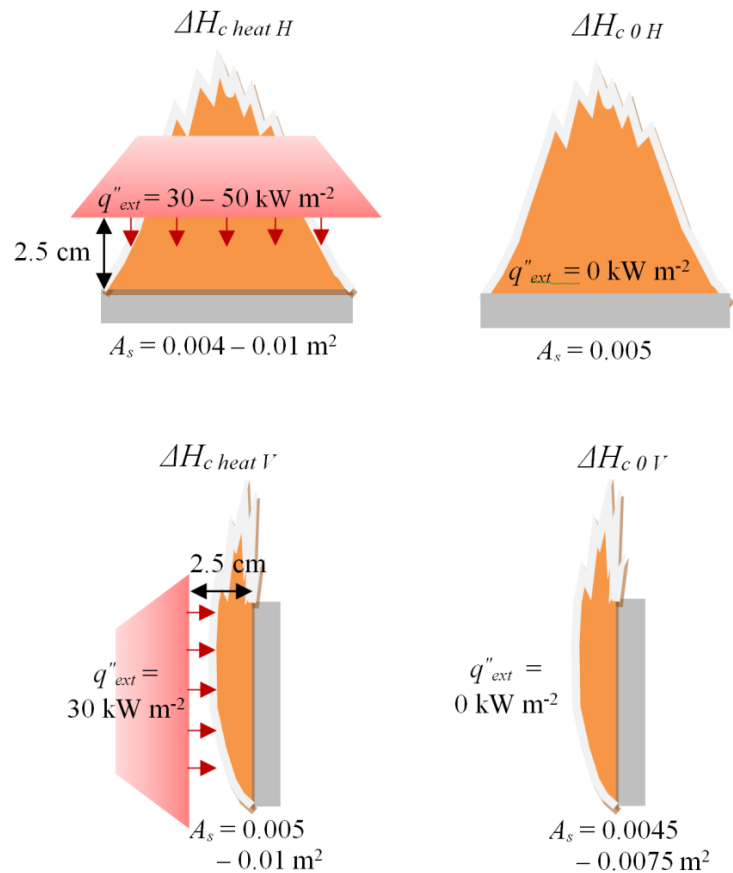


Figure 26. Cone calorimeter heat of combustion test configurations

The majority of heat of combustion tests were performed on 10×5 cm samples; these dimensions match the average sample size used in flame spread experiments. Additional tests were also performed in the horizontal configuration using 10×10 cm samples; these dimensions correspond with the values prescribed in the cone calorimeter test standard [3]. In the vertical configuration, it has been shown that samples of finite width may support shorter flames [49] and slower flame spread [53] than samples that can be treated as infinitely wide. It is possible that this results from the diffusion (outflow without burning) of gaseous volatiles away from the sides of these narrow flames. To assess the impact of such behavior on the heat of combustion measurements obtained here, several experiments were thus also performed on 10 cm wide samples burning in the vertical configuration. No significant difference was observed between these tests – in both the vertical and horizontal configurations, for samples 5 and 10 cm wide, heat of combustion measurements differ, on average, by less than 3 % for each of the materials tested. Because these measurements are nearly identical, they have been averaged together when presented in Section 4.4.3 of this work. Table 4 summarizes the number of heat of combustion tests performed on each material in each of these four configurations.

Table 4. Test matrix of heat of combustion experiments performed in the cone calorimeter

Material	Horizontal	Horizontal	Vertical	Vertical
	$q_{ext}'' = 30 - 50 \text{ kW m}^{-2}$	$q_{ext}'' = 0 \text{ kW m}^{-2}$	$q_{ext}'' = 30 \text{ kW m}^{-2}$	$q_{ext}'' = 0 \text{ kW m}^{-2}$
ABS	5	---	6	2
FRP	3	---	1	4
HIPS	4	---	3	3
PBT	3	---	---	2
PMMA _{CAST}	3	2	3	3
PMMA _{EXT}	3	---	3	4
POM	4	---	3	4
PP	3	2	4	4

At the beginning of each day of testing, the cone calorimeter was set up and calibrated in accordance with the relevant standard [3]. The cone calorimeter's O₂ analyzer was calibrated by measuring its response to alternating, five-minute-long exposures to pure nitrogen and ambient air with an oxygen concentration of 20.95% (by volume). The CO and CO₂ analyzers were similarly calibrated by measuring their responses to a well-defined mixture of CO and CO₂ – 0.8 % and 8.0 % (by volume), respectively – for five minutes preceded and followed by a five minute exposure to pure nitrogen. At both the beginning and at the end of each day of testing, validation tests were performed by measuring $\Delta H_{c, heat H}$ of a 10 × 10 × 1.2 cm sample of black PMMA_{CAST} to ensure that this value was within 5% [89] of the established literature value of 25 kJ g⁻¹ [69].

For all tests conducted with an external heat flux, prior to sample insertion beneath or next to the cone calorimeter heater, incident heat flux at the location of the sample's top or front (burning) surface was measured by a 1.27 cm diameter, water-cooled Schmidt-Boelter heat flux gauge. As the cone calorimeter heater warmed up, samples used in horizontal tests were removed from the desiccator, weighed, wrapped around their bottom and sides by a 0.05 mm thick sheet of aluminum foil, weighed again,

and placed on top of four 6 mm thick Kaowool PM sheets supported by a steel sample holder. All samples burned in the vertical configuration were mounted onto Kaowool PM insulation and supported in a sample holder identically as in the flame spread tests described in Section 2.2 of this manuscript.

After the cone heater reached a steady temperature, data acquisition systems were turned on. One minute after measurement recording began, the heater was temporarily shielded by a layer of insulation and the sample holder was positioned such that the top (or front) surface of the sample was 2.5 cm away from the base of the heater, as specified in the standard [3] (Fig. 26). After the sample holder was secured, the heater shield was removed and a spark igniter was positioned over the center of the sample, 0.5 cm away from its surface. As soon as sustained flaming was observed, the spark igniter was removed and sample ignition time was recorded. Following the standard test procedure, horizontal tests were allowed to continue until the entire sample was consumed, at which point sample extinction time was noted. In the vertical configuration, material burning behavior was carefully and continuously monitored and samples were extinguished when significant polymer melt flow, dripping, or solid residue formation at the sample's surface was observed. For all tests, measurements were recorded for at least two minutes after flame extinction. After each test, the aluminum foil (or sample insulation) and any remaining residue were weighed on a separate mass balance.

Samples used for heat of combustion tests that did not use an external heat flux were prepared and allowed to burn identically as those that did, with the following modifications to the ignition procedure. In each of these experiments, the cone heater was removed from its standard position so that it would not heat up during tests and reradiate

energy back into samples as they burned. Samples that were burned horizontally were placed in the sample holder and ignited away from the cone calorimeter by a premixed propane flame that was applied to their top surface just long enough for sustained, uniform ignition (between 45 and 90 s; material dependent). The sample holder was then placed on the mass balance, under the cone calorimeter exhaust hood. Samples that were burned vertically were prepared, supported in the sample holder, and ignited identically as in flame spread tests described in Section 2.2 of this manuscript.

In cone calorimeter tests, heat of combustion was calculated throughout the duration of experiments as

$$\Delta H_c^{MATL} \Big|_{t_i} = \frac{\int_{t_i}^{t_i+\Delta t} Q(t) dt}{m_{t_i} - m_{t_i+\Delta t}} \quad \text{Equation 31}$$

where Q [kW] and m [g] are measured heat release and sample mass, respectively, t [s] is time, and $\Delta t = 1$ s is the time interval over which measurements are obtained. As seen in Fig. 27, quasi-steady heat of combustion measurements are obtained during the majority of experiments; however, shortly after sample ignition and towards the final stages of tests – when material burning behavior becomes non-ideal (e.g. due to sample burnout) – heat of combustion measurements (calculated as per eqn. 31) are no longer accurate. To eliminate the impact of these behaviors, measurements reported in this work – $\Delta H_{c\ heat\ H}$, $\Delta H_{c\ heat\ V}$, $\Delta H_{c\ 0\ H}$, and $\Delta H_{c\ 0\ V}$ – are calculated as the time-averaged heat of combustion measured only during this quasi-steady period of burning. In using only these measurements, it is implicitly assumed that deviations in heat of combustion measured

during the initial and final stages of tests are manifestations of secondary burning behavior and not a result of changes in the gaseous volatiles produced by the sample.

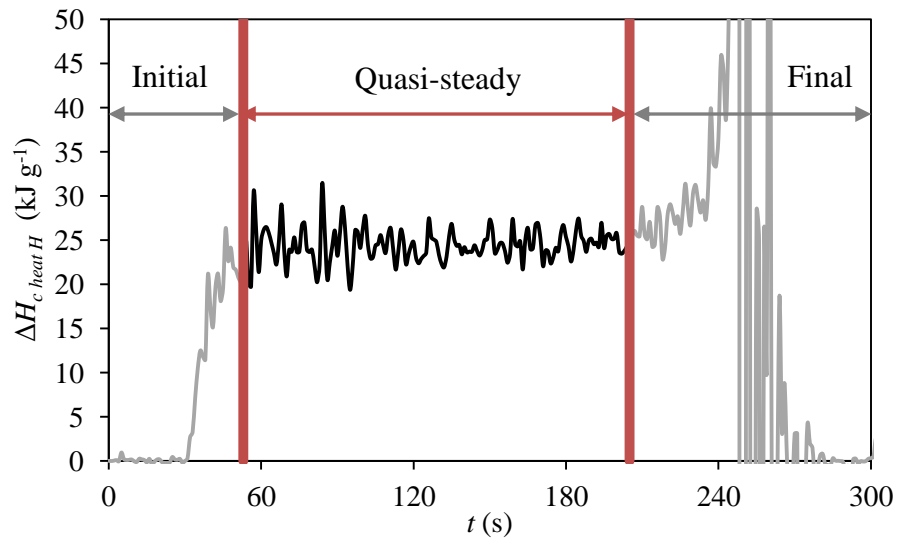


Figure 27. Measured heat of combustion, $\Delta H_{c, heat H}$, of a 10 x 10 cm cast PMMA sample burning in the standard (horizontal) configuration in the cone calorimeter

4.4 Results

4.4.1 Material Burning Behavior, Qualitative Observations

4.4.1.1 PMMA_{CAST}

Fig. 28 shows typical fire growth during upward flame spread over a 15 cm tall sample of PMMA_{CAST}. Timestamps in this and all other figures of material burning behavior (Figs. 28 – 36) indicate time after sample ignition. PMMA_{CAST} samples can be uniformly ignited across their base by a 125 s exposure to the propane burner. PMMA_{CAST} samples did not require an external heat flux to support upward flame spread. Much like for PMMA_{EXT}, a thin layer (< 0.5 mm) of soot was observed to quickly deposit between the flame and the surface of PMMA_{CAST} samples, downstream of the pyrolysis front at $y > 4$ cm. This layer did not appear to impede flame spread but it effectively transformed PMMA_{CAST} slabs from clear to non-transparent. As samples continued burning, the flame transitioned away from purely laminar behavior. For PMMA_{CAST}, unlike PMMA_{EXT}, the base of the flame remained fixed to the lower edge of the sample ($y = 0$) throughout the duration of experiments. Approximately 600 s after ignition, burnout of the base of the material allowed for ignition of the epoxy layer behind the sample, thus necessitating sample extinction.

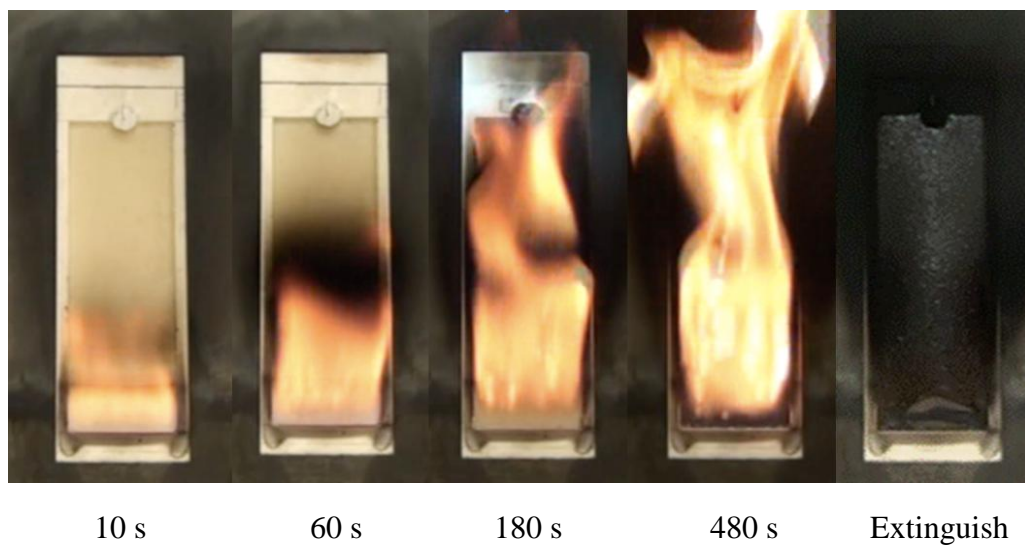


Figure 28. Representative test of flame spread over a 15 cm tall sample of PMMA_{CAST}

4.4.1.2 Materials Exhibiting Significant Melt Flow: PP and POM

PP samples supported sustained, uniform ignition across their base following a 110 s exposure to the propane burner. PP melts at approximately 435 K [56] and consequently began flowing downwards early on in experiments – by the time samples ignited, the base of the flame was located 0.5 cm below the bottom edge of the sample slab ($y_b = -0.5$ cm). As seen in Fig. 29, as PP burned, a soot layer quickly formed at the material's surface, both directly beneath the flame and beyond the farthest reaches of flame tips. Although this soot layer remained rather thin throughout each test, it appears to have inhibited flame spread – during the early stages of tests, in the absence of external heating (i.e. when $q_{ext}'' = 0$), the pyrolysis front did not advance beyond the region of the sample originally preheated by the propane burner. However, as PP samples continued burning, the front-most layer of samples softened and flowed downwards thus fragmenting the attached soot layer. This exposed the virgin material behind at which point the pyrolysis front was observed to advance. Although PP samples melt readily, the base of the flame never extended below $y = -2$ cm. At later times in each test, melted PP began dripping from the sample slab to the base of the sample holder. The resulting drip pool did not burn and thus did not contribute to measured sample mass loss rate.

In several tests, an external heat flux was applied to polypropylene samples to enhance the rate of upward flame spread. When $q_{ext}'' = 5$ kW m⁻², the wall flame grows quicker; however, pyrolysis remains primarily restricted to the region of the sample preheated by the burner. In these tests, at the time of wall flame extinction, 45% of total mass lost from the sample has simply dripped to the base of the sample holder, without burning. When $q_{ext}'' = 10$ kW m⁻², fire growth is further enhanced but significant dripping

is observed. Under these conditions, approximately 68% of the mass lost from the sample by the end of each test remained in a drip pool at the bottom of the sample holder. Measurements of sample mass loss rate and heat feedback during upward flame spread over PP are thus obtained from experiments conducted without an external heat flux. These results are analyzed only during the first 400 s after sample ignition, prior to significant polymer melt flow.

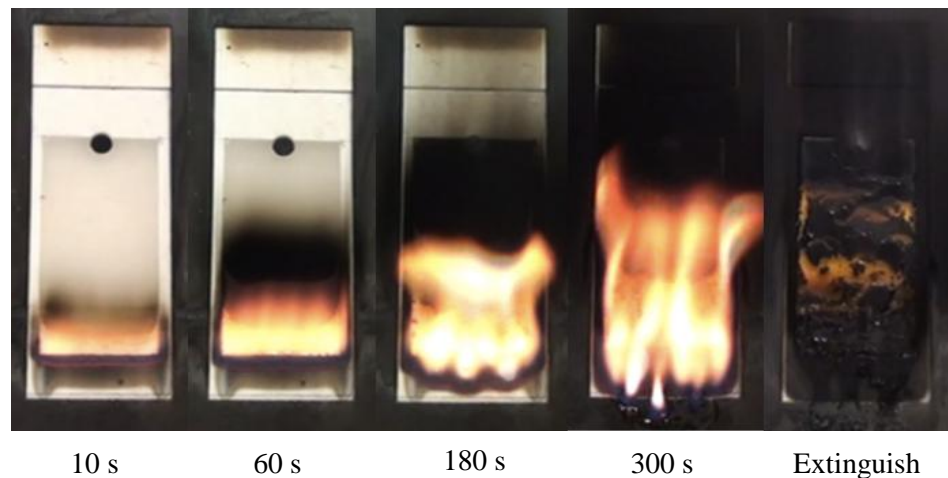


Figure 29. Representative test of upward flame spread over a 10 cm tall PP sample

Note: in this figure, $q_{ext}'' = 0$

POM samples required a 135 s exposure to the propane burner to achieve uniform ignition across their base (thus, for POM, $t_{ign} = 135$ s). POM did not require an external heat flux to support upward flame spread. As seen in Fig. 30, POM does not produce soot while burning and thus it maintained a transparent blue flame throughout the duration of tests. Shortly after ignition, POM samples supported a very small (approximately 1 cm tall) flame; however, within 180 s of sample ignition, a strong, steady flame, with tips extending up to $y = 6 - 8$ cm, was observed. Prior to chemical decomposition, POM melts

when heated above ~ 455 K [56]. Consequently, as POM burns in the vertical configuration, the polymer readily melts and flows downwards, bringing with it the base of the flame. 240 s after sample ignition, a layer of polymer melt had collected on the edge of the steel holder beneath the sample ($y = -2$ cm). At $t - t_{ign} \approx 300$ s, the pyrolysis front neared the top of 12.5 cm tall samples. Between $390 < t - t_{ign} < 430$ s a sudden and significant melt flow event was consistently observed – typically, a region of the sample’s base (approximately 3 cm wide, and 1.5 cm tall) quickly flowed down forming a large, flaming drip pool at the base of the holder stand. Shortly after this event, the drip pool and wall fire were both extinguished.

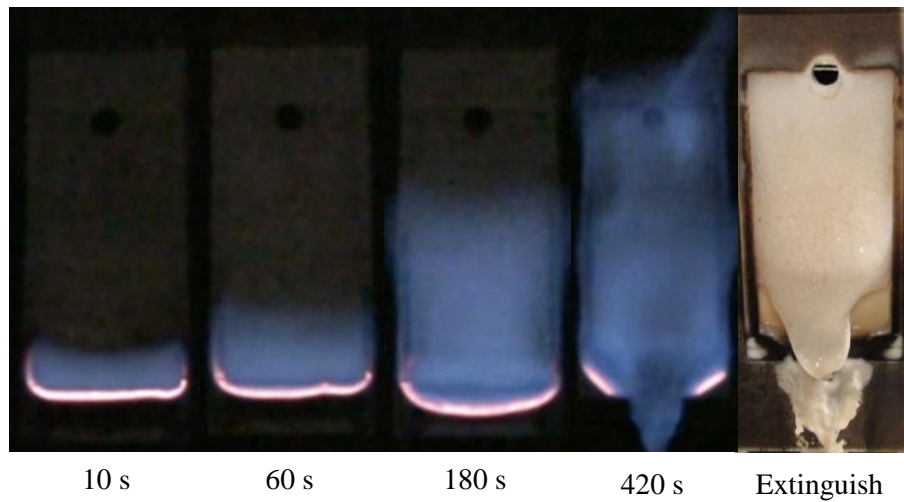


Figure 30. Representative test of upward flame spread over a 10 cm tall POM sample

Note: in this figure, and in all tests on POM, $q_{ext}'' = 0$

4.4.1.3 Heavily Sooting Materials: ABS and HIPS

Sustained, uniform ignition of ABS samples required a 205 s application of the propane burner. Within 10 s of sample ignition, a dark layer of soot deposited across the full length of 15 cm tall samples; these deposits extended well beyond even the upper most location of transient flame tips. As seen in Fig. 31, as ABS samples continued burning, soot continued to deposit across the unburnt polymer creating a dark, low density layer that measured at least 1 mm thick across the sample's surface within 120 s of sample ignition. Further soot growth appeared to remain fairly uniform across the sample's surface resulting in a 3 – 3.5 mm thick soot layer that was slightly thicker towards the sample's base. Although a continuous flame sheet could be observed up to $y = 8 - 10$ cm for several minutes after sample ignition, in the absence of an external heat flux, this soot layer effectively inhibited progression of the pyrolysis front, ultimately causing sample extinction when the initial pyrolysis zone reached burnout. After extinction, a thin layer of char was observed at the material's front surface, behind the soot layer. The growth of the underlying char layer is difficult to track temporally; at extinction, this layer measured between 0.5 and 1 mm thick.

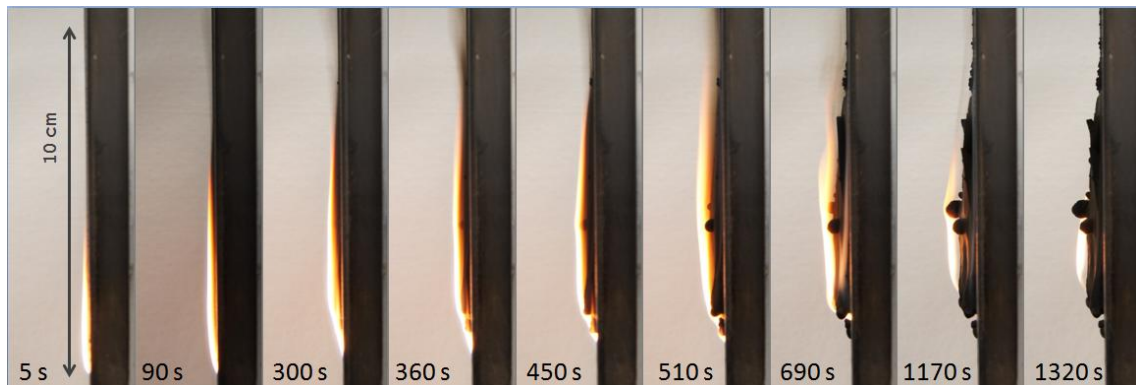


Figure 31. Auto-suppression of upward flame spread over ABS by soot deposition

Note: in this figure, $q_{ext}'' = 0$

Applying an external radiant heat flux of $q_{ext}'' = 10 \text{ kW m}^{-2}$ to the surface of ABS samples immediately after ignition induced flame spread over the material. Under these conditions, flame heat flux and sample mass loss rate measurements could be analyzed for up to 480 s after sample ignition. Although heavy soot deposition was still observed in these tests, small fractures in the soot layer began to form and extend upwards from the base of the sample as it continued burning. As seen in Fig. 32 (which shows the front surface of four ABS samples, each extinguished at progressively later times after ignition) as ABS samples continued burning under these conditions, these fractures widened, indicating higher rates of pyrolysis in those regions of the sample, and small fractures developed farther downstream. The propagation of fractures in the surface layer of soot deposits in this manner, similar to the more uniform propagation of the pyrolysis front during flame spread over PMMA, indicates that flame spread in this system was dominated by flame to surface heat transfer, and not by the influence of the external heater, which applied a uniform heat flux across the material's surface. It should be noted that high molecular weight decomposition products, which appear as white smoke, were only observed to flow out through these cracks following flame extinction. This suggests that flammable products of pyrolysis escape primarily through these cracks, and not through the soot layer itself.

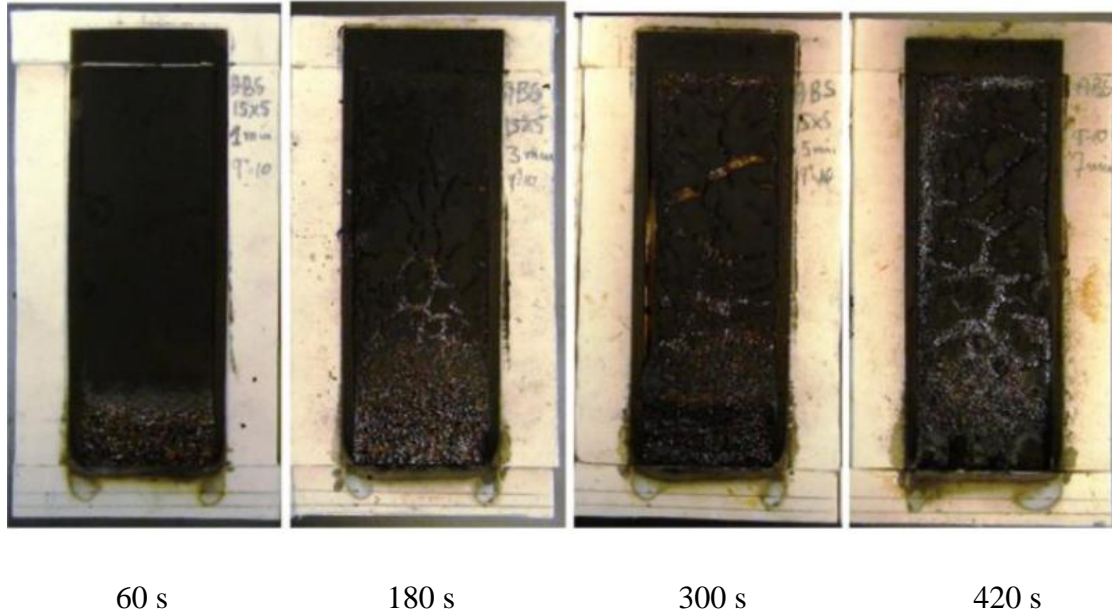


Figure 32. Evolution of soot deposition during upward flame spread over 15 x 5 cm ABS samples exposed to an external heat flux of $q_{ext}'' = 10 \text{ kW m}^{-2}$

Sustained, uniform ignition of HIPS samples required a 120 s application of the propane burner. When burning in the vertical configuration, much like ABS, the soot produced by HIPS flames readily adhered to the surface of the virgin polymer, forming a smooth, flat layer across the full length of 15 cm tall samples within 10 s of sample ignition. This soot layer extended beyond the flame tips, and grew thickest directly beneath the flame (up to 2 cm thick, at the time of sample extinction). Unlike ABS, this soot layer did not grow uniformly to maintain a smooth top surface. Instead, as seen in Fig. 33, thin strands of soot attached themselves to the sample (and the insulation and sample holder). Soot continued to agglomerate at these points, forming thicker and longer structures, which grew as far as 2 cm normal to the material's surface. During the early stages of soot layer growth on HIPS samples, flames could be found near the polymer's surface, in between individual soot structures. Although flames remained fairly uniform

across the width of the sample as it burned, as this soot layer thickened, it produced an increasingly effective physical and thermal barrier that better separated the flame from the polymer's surface, ultimately causing flame extinction.

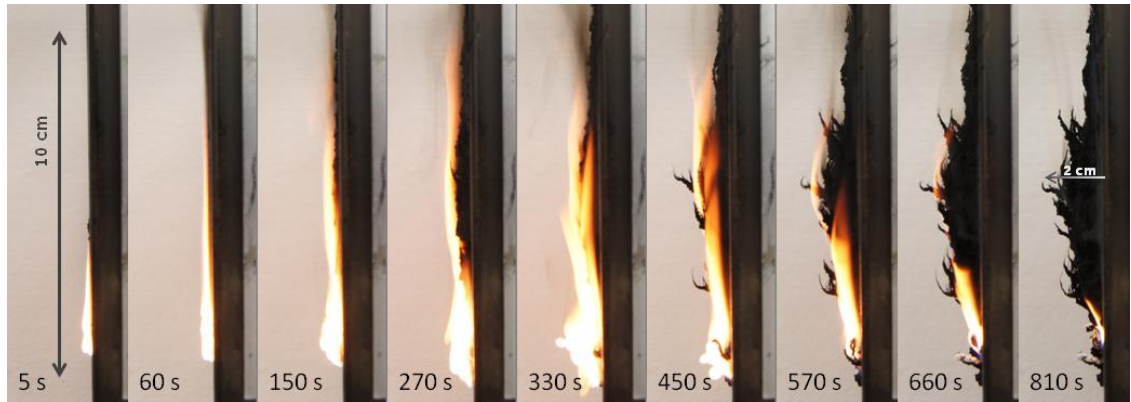


Figure 33. Auto-suppression of upward flame spread over HIPS by soot deposition

Note: in this figure, $q_{ext}'' = 0$.

Numerous attempts were made to induce flame spread over HIPS samples including angling the sample up to 20 degrees away from the vertical (to limit soot deposition), increasing the size and duration of the burner exposure, and exposing samples to an external heat flux of up to $q_{ext}'' = 15 \text{ kW m}^{-2}$. Although some of these measures allowed for the development of larger fires, one-dimensional upward propagation of the flame front could not be achieved. When a radiant heat flux of $q_{ext}'' = 15 \text{ kW m}^{-2}$ is applied to the surface of HIPS samples following ignition, fractures were observed to form in the soot layer; however, they do not evolve identically as for ABS samples. As seen in Fig. 34, fractures in the layer of soot that deposits across HIPS samples form both along the sample's edges and across the sample's surface, with no preferred propagation direction. This suggests that the dynamics of flame spread in this

system is inconsistent with one dimensional advancement of the flame front. By extinction, the entire surface of the sample is pyrolyzing. Because each of our attempts to induce flame spread increased the complexity of the experimental procedure without providing a corresponding improvement in material burning behavior, HIPS flames were studied without the application of an external heat flux, following the experimental procedure described in Section 2.2 of this manuscript. However, because heavy soot deposition was not mitigated in these experiments, HIPS flame heat flux measurements were analyzed only until 180 s after sample ignition.

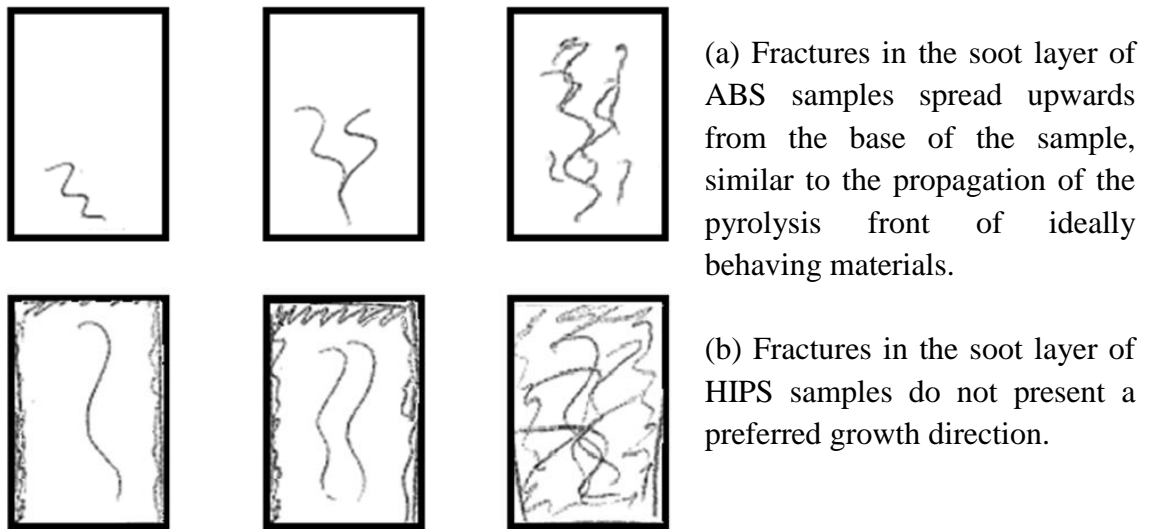


Figure 34. Sketch of fracture propagation in soot layer formed across the surface of (a) ABS and (b) HIPS samples as they burn in the vertical configuration

4.4.1.4 Composite Materials: FRP and PBT

Fig. 35 shows typical fire growth over a 10 cm tall FRP sample. Uniform ignition of this material at its base required a 135 s exposure to the propane burner. FRP samples did not require an external heat flux to support upward flame spread. The initial flame was approximately 2 cm tall and it remained fairly weak throughout the test (FRP flames could be easily extinguished by perturbations of local air entrainment). Within 60 s of ignition, a thin layer of soot had deposited across the surface of FRP samples despite the absence of direct flame impingement towards the top of the material. As tests continued, burnout was observed near the base and along the sides of the sample resulting in a progressively narrower flame. Despite this observed burnout, samples maintained their original shape throughout experiments, leaving behind a residual structure (layers of fiberglass reinforcement). To avoid complications that could arise with very narrow flames, sample mass loss rate and flame heat flux measurements were analyzed only during the first 240 s after sample ignition, when the flame remained at least 4 cm wide.

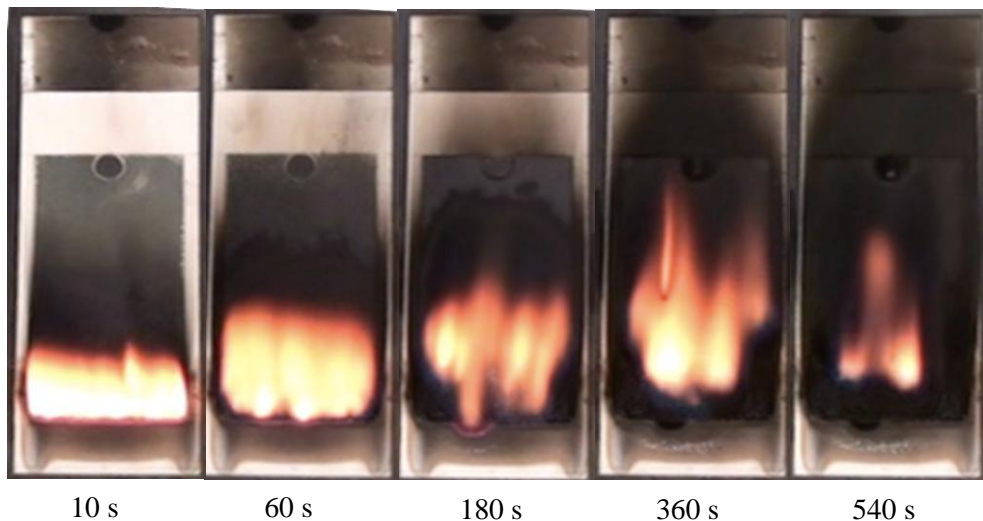


Figure 35. Representative test of upward flame spread over a 10 cm tall FRP sample

Note: in this figure, and in all tests on FRP, $\dot{q}_{ext}'' = 0$

Fig. 36 shows typical fire behavior during upward flame spread over PBT. Sustained, uniform ignition of this material was achieved by a 120 s application of the propane burner. PBT samples did not require an external heat flux to support upward flame spread. Within 90 s of ignition, flame tips were observed up to $y = 6$ cm and a thin, dark layer of soot had deposited farther downstream, across the full length of the sample. Although this soot layer developed quickly, it remained less than 1 mm thick and did not appear to inhibit flame spread. Throughout the duration of tests, the flame sheet supported by PBT samples remained continuous and laminar across its length. Burnout was first observed near the bottom corners of the sample, approximately 150 s after sample ignition. Because the PBT tested in this work is a composite material, which is reinforced by chopped glass fibers, samples maintained their original shape throughout experiments and left behind a residual structure after burnout. Sample extinction occurred when burnout caused the base of the flame to advance up towards the top of the sample. Shortly before sample extinction, PBT flames narrowed due to burnout along the edge of the sample; however, flame heat flux measurements were only analyzed during the first 270 s after sample ignition, prior to the development of this behavior.

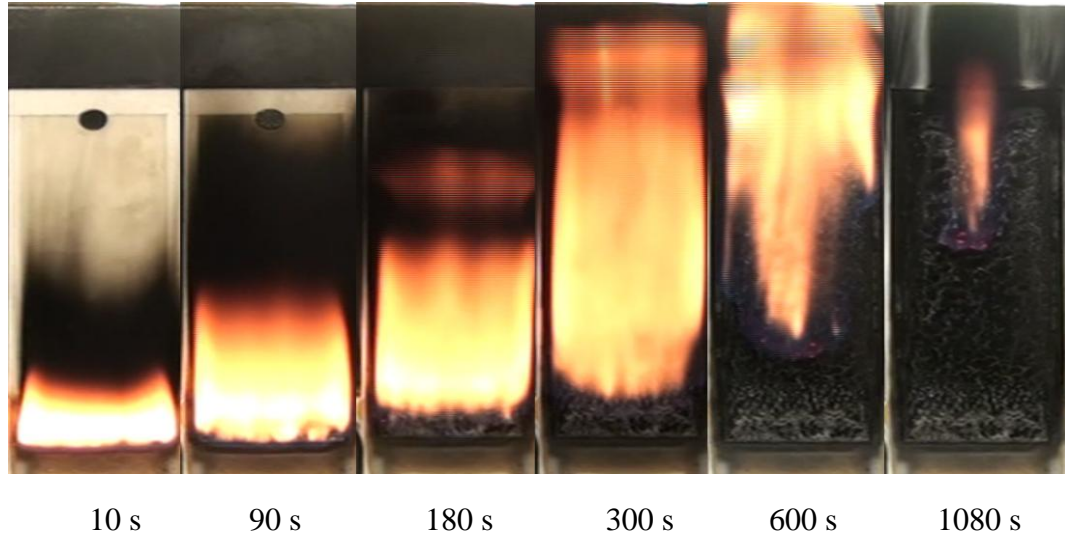


Figure 36. Representative test of upward flame spread over a 14.5 cm tall PBT sample

Note: in this figure, $q_{ext}'' = 0$

4.4.2 Upward Flame Spread

4.4.2.1 Mass Loss Rate

Measured width-normalized mass loss rate of 7, 10, and 15 cm tall samples of PP and ABS are plotted in Figs. 37 and 38. For PP, $\frac{dm'}{dt}$ of samples of all three heights is identical throughout the first 400 s after sample ignition. This suggests that the pyrolysis front never advances beyond $y = 7$ cm in this time, a behavior confirmed by visual observations of material burning behavior (see Section 4.4.1.2). For ABS, $\frac{dm'}{dt}$ of samples of all three heights is identical until approximately 45 s after ignition, at which point, measured mass loss rate of 7 cm tall samples no longer continues to increase at the same rate as that of larger samples. Later in the test, approximately 120 s after ignition, the measured mass loss rate curve of 10 cm tall ABS samples similarly breaks away and no longer continues to increase at the same rate as that of 15 cm tall samples.

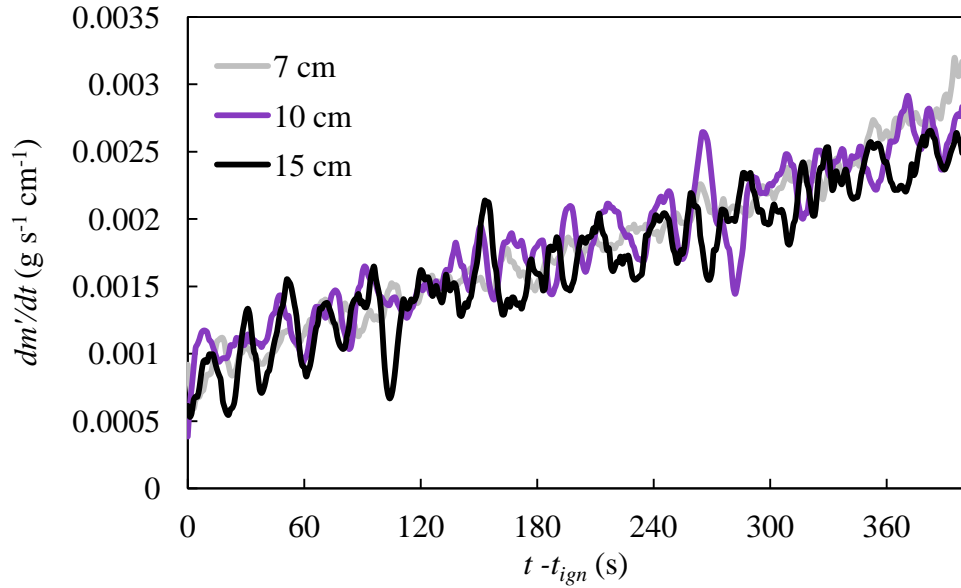


Figure 37. Measured width-normalized mass loss rate of PP samples of different heights

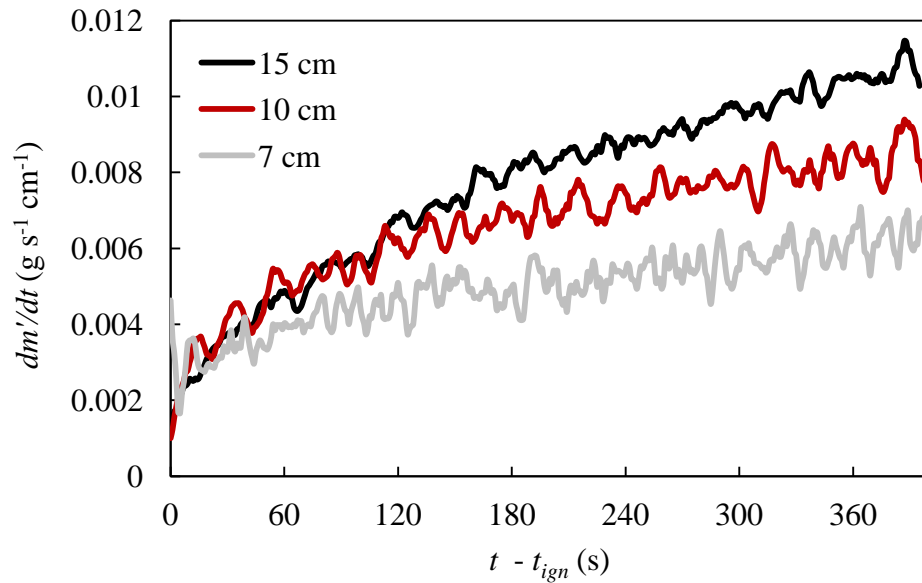


Figure 38. Measured width-normalized mass loss rate of ABS samples of different heights

These results validate previous observations on PMMA_{EXT} (see Section 2.4.1) thus confirming that the development of the pyrolysis zone during flame spread over a material is not altered between samples of different heights, provided that they are ignited

and a flame is allowed to spread across their surfaces identically. Consequently, $\frac{dm'}{dt}$ measured at a single height – that of the largest samples tested – is used here to accurately characterize the mass loss rate of all smaller samples. Fig. 39 shows measured width-normalized mass loss rate of the largest samples of each of the materials tested in this work. Here, solid lines indicate experimental measurements (average of three repeated tests) and dashed lines represent fitted curves, which smooth these measurements for use in further analysis. Except for ABS, for which $q_{ext}'' = 10 \text{ kW m}^{-2}$, all measurements presented here were obtained as samples burned without external heating. Sample height of each material in this figure is listed in Table 5. Fitted $\frac{dm'}{dt}$ curves are piecewise defined by a series of second to fifth order polynomials of the form

$$\frac{dm'}{dt} = c_0 + c_1(t - t_{ign}) + c_2(t - t_{ign})^2 + c_3(t - t_{ign})^3 + c_4(t - t_{ign})^4 + c_5(t - t_{ign})^5 \quad \text{Equation 32}$$

where $\frac{dm'}{dt}$ is measured in $\text{g s}^{-1} \text{ cm}^{-1}$ and $t - t_{ign}$ (time after sample ignition) is measured in s. The coefficients $c_0 - c_5$ used to define these fitted curves, the time ranges for which these expressions are valid, and the sample ignition times, t_{ign} , of each material are provided in Table 5.

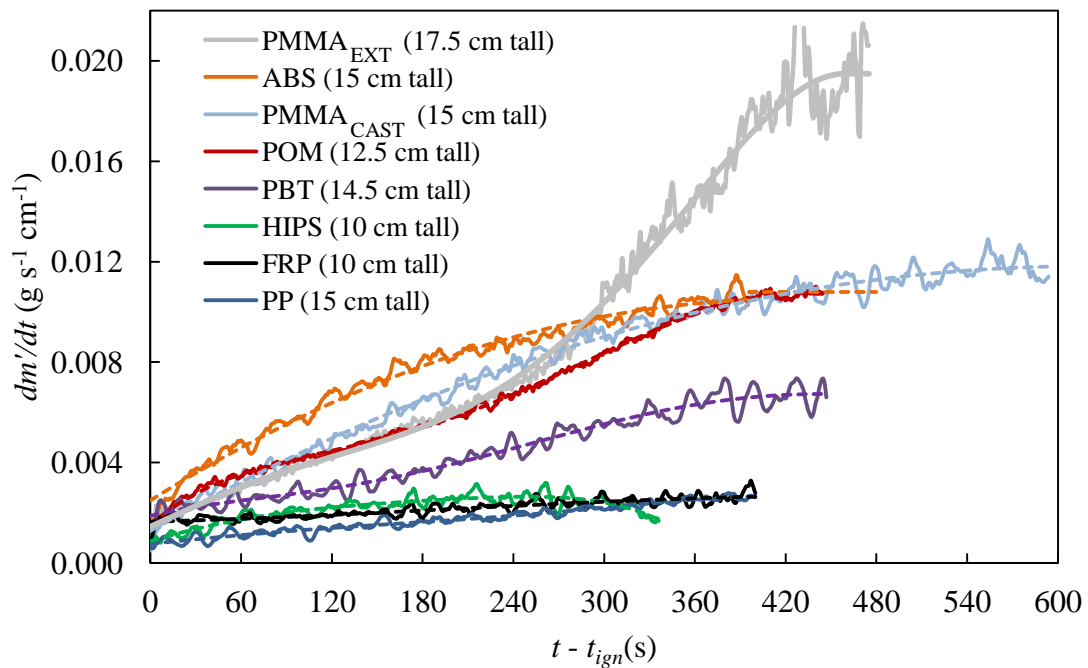


Figure 39. Width-normalized sample mass loss rate of each polymer tested in this work

Note: Legend entries in parentheses indicate sample height

Table 5. Coefficients used with eqn. 32 to describe $\frac{dm'}{dt}$ during upward flame spread

Material	Sample height (cm)	t_{ign} (s)	Valid for $t - t_{ign}$ (s)	c_0	c_1	c_2	c_3	c_4	c_5
				($\text{g s}^{-1}\text{cm}^{-1}$)	($\text{g s}^{-2}\text{cm}^{-1}$)	($\text{g s}^{-3}\text{cm}^{-1}$)	($\text{g s}^{-4}\text{cm}^{-1}$)	($\text{g s}^{-5}\text{cm}^{-1}$)	($\text{g s}^{-6}\text{cm}^{-1}$)
ABS ¹	15	205	0 - 50	1.56×10^{-3}	9.13×10^{-5}	-6.84×10^{-7}	0	0	0
			50 - 400	4.74×10^{-3}	-4.12×10^{-5}	9.58×10^{-7}	-5.55×10^{-9}	1.36×10^{-11}	-1.20×10^{-14}
			400 - 480	1.08×10^{-2}	0	0	0	0	0
FRP ²	10	135	0 - 415	1.65×10^{-3}	1.49×10^{-6}	7.87×10^{-9}	-1.35×10^{-11}	0	0
HIPS	10	120	0 - 330	8.67×10^{-4}	1.77×10^{-5}	-4.85×10^{-8}	-2.20×10^{-10}	1.82×10^{-12}	-3.38×10^{-15}
PBT	14.5	120	0 - 450	1.87×10^{-3}	1.47×10^{-5}	-1.14×10^{-7}	7.58×10^{-10}	-1.72×10^{-12}	1.24×10^{-15}
PMMA _{EXT}	15	125	0 - 460	1.45×10^{-3}	2.79×10^{-5}	4.75×10^{-9}	-8.13×10^{-10}	4.35×10^{-12}	-5.40×10^{-15}
PMMA _{CAST}	20	125	0 - 600	1.27×10^{-3}	3.40×10^{-5}	-2.74×10^{-8}	0	0	0
POM	12.5	135	0 - 445	1.51×10^{-3}	5.18×10^{-5}	-3.98×10^{-7}	1.78×10^{-9}	-3.07×10^{-12}	1.64×10^{-15}
PP	15	110	0 - 400	7.65×10^{-4}	5.79×10^{-6}	6.36×10^{-9}	-1.59×10^{-10}	6.66×10^{-13}	-8.11×10^{-16}

¹ Measured with $q_{ext}'' = 10 \text{ kW m}^{-2}$

² For FRP, $\frac{dm'}{dt}$ is normalized by flame width (between 4 and 5 cm)

4.4.2.2 Flame Heat Flux

Figs. 40 - 47 show measured flame heat flux, q_{HFg}'' , during upward flame spread over PMMA_{CAST}, PP, POM, ABS, HIPS, FRP, and PBT. In each figure, q_{HFg}'' is measured at several locations, y ; this length scale indicates distance from base of the sample to the center of the heat flux gauge. Each data set plotted in these figures represents an average measurement obtained from three independent experiments. Error bars in each figure indicate two standard deviations of the mean; for many of the measurements presented here, error bars are comparable in size to data symbols.

For all materials tested in this work, at each sample height, q_{HFg}'' increases with time as the flame spreads towards the heat flux gauge. As expected, it takes progressively longer for peak, steady flame heat fluxes to be recorded at higher sample heights; the delay corresponding to the additional time needed for the flame to spread upwards to that measurement location. For ABS and HIPS samples, however, heat flux measurements do not remain steady, and instead show a continuous decrease with time after a peak value is recorded. This reduction in measured heat flux can be attributed to the soot layer that deposits on the surface of each material as they burn and a similar (and significant) residue layer that forms on the heat flux gauge's surface by the end of each test.

For ABS and HIPS samples, to mitigate the effects of this soot deposition, an additional series of tests was performed in which the gauge was shielded using a custom fitted piece of insulation. In Figs. 43 – 45, the maximum flame heat flux measured within 10 s of shield removal in these tests is plotted as discrete data points labeled 'Shielded'. As seen in these figures, at each of these removal times, shielded measurements are 5 to 20 kW m⁻² greater than unshielded ones. This difference indicates that the insulating

effect of this deposition layer is significant, and that it can develop soon after sample ignition. Unshielded heat flux measurements of ABS and HIPS flames are analyzed until the latest time in experiments when measured flame heat flux increases by at least $0.05 \text{ kW m}^{-2} \text{ s}^{-1}$. At later times in the experiment, a curve representing flame to surface heat flux that would be measured in the absence of soot deposition is defined by interpolating between the last measurements recorded before soot deposits impacted unshielded measurements and clean gauge readings recorded in shielded tests. This shielded interpolation is plotted in Figs. 43 – 45 as a dashed line.

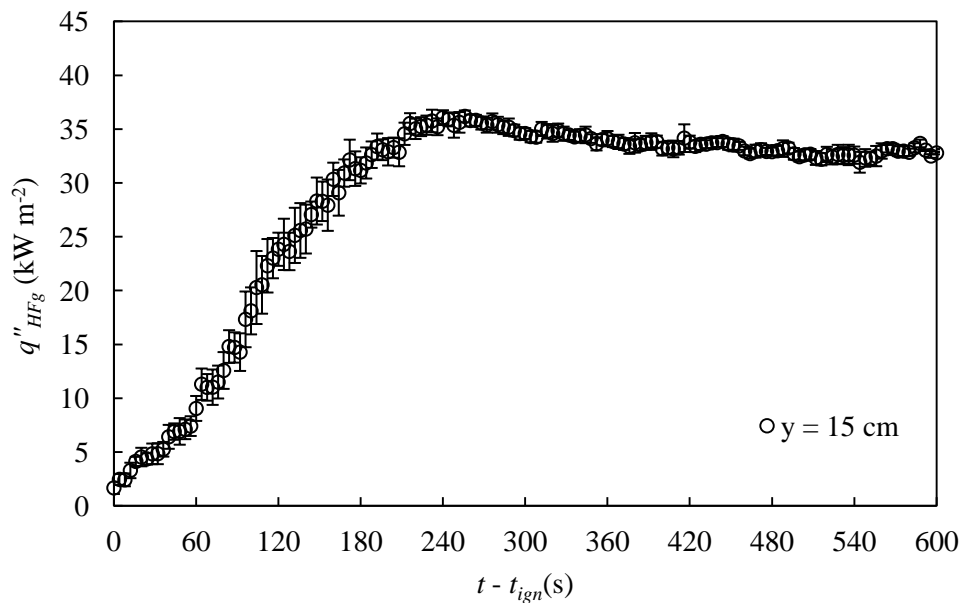


Figure 40. Measured PMMA_{CAST} flame heat flux at $y = 15 \text{ cm}$

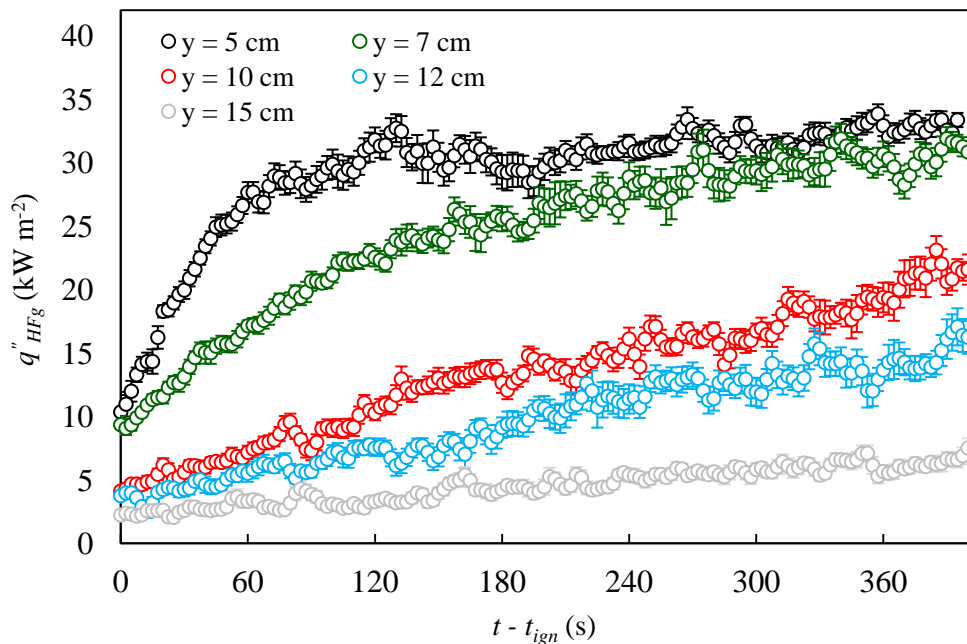


Figure 41. Measured PP flame heat flux at $y = 5, 7, 10, 12,$ and 15 cm

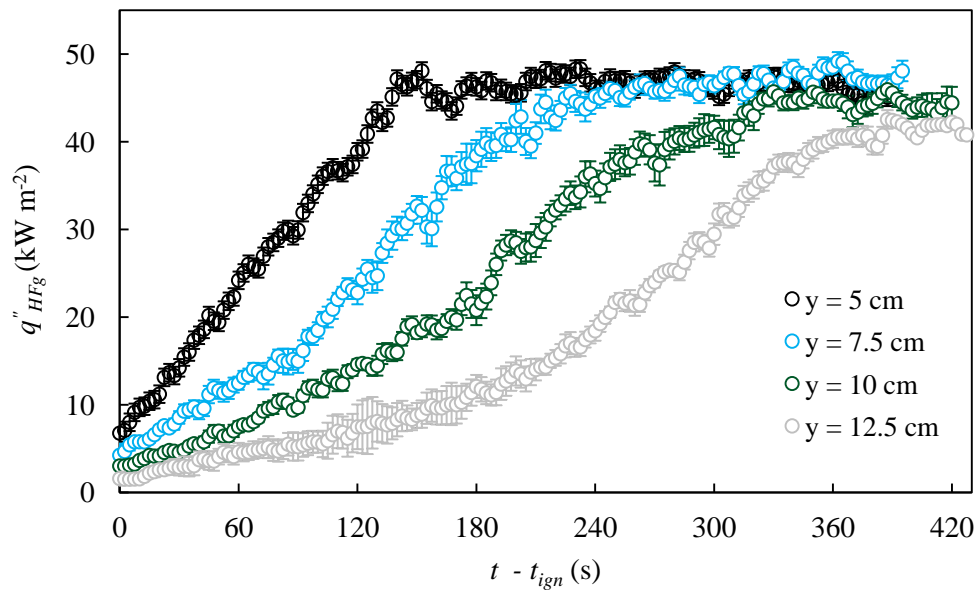


Figure 42. Measured POM flame heat flux at $y = 5, 7.5, 10,$ and 12.5 cm

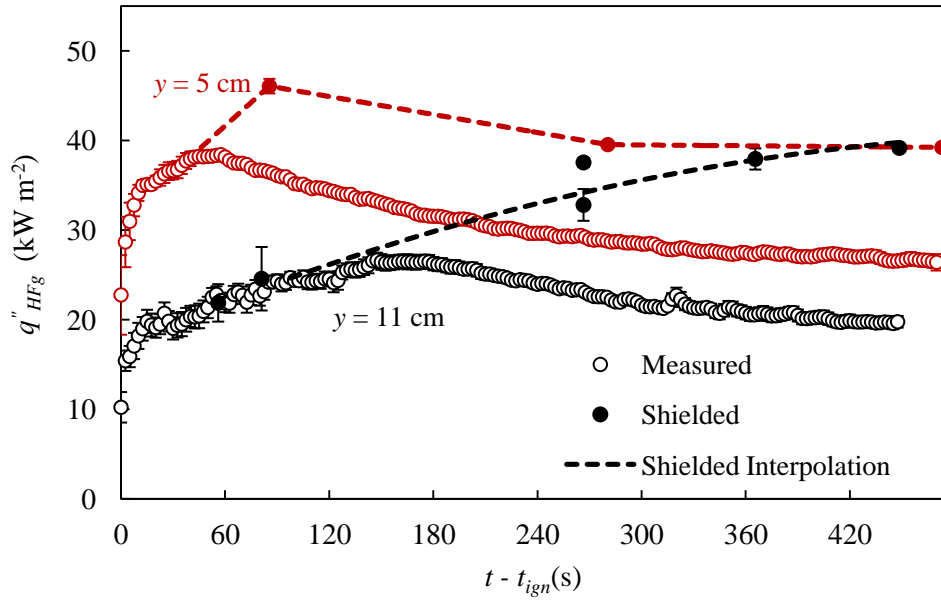


Figure 43. Measured ABS flame heat flux at $y = 5$ and 11 cm

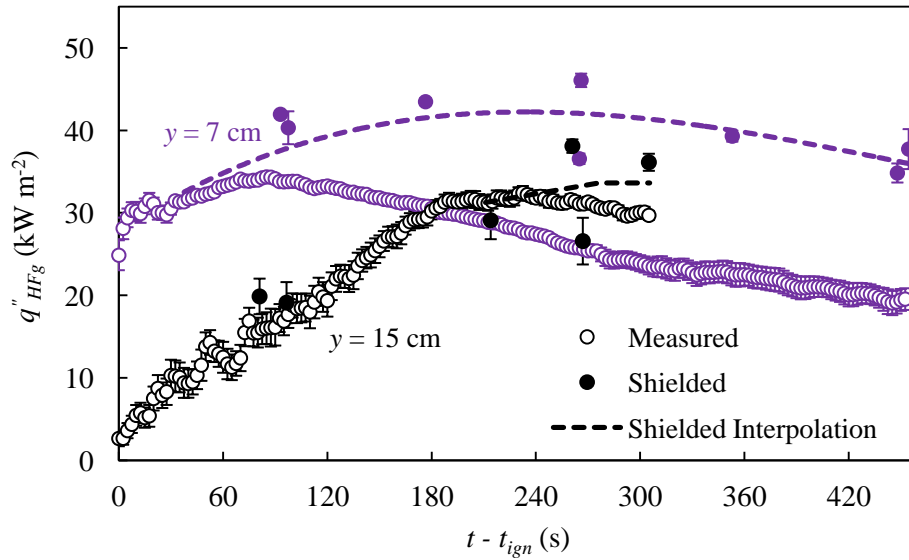


Figure 44. Measured ABS flame heat flux at $y = 7$ and 15 cm⁷

⁷ Note: Figs. 43 and 44 both contain heat flux measurements from the same material, ABS. These results have been separated into two figures for clarity (to avoid overlap in plotted values).

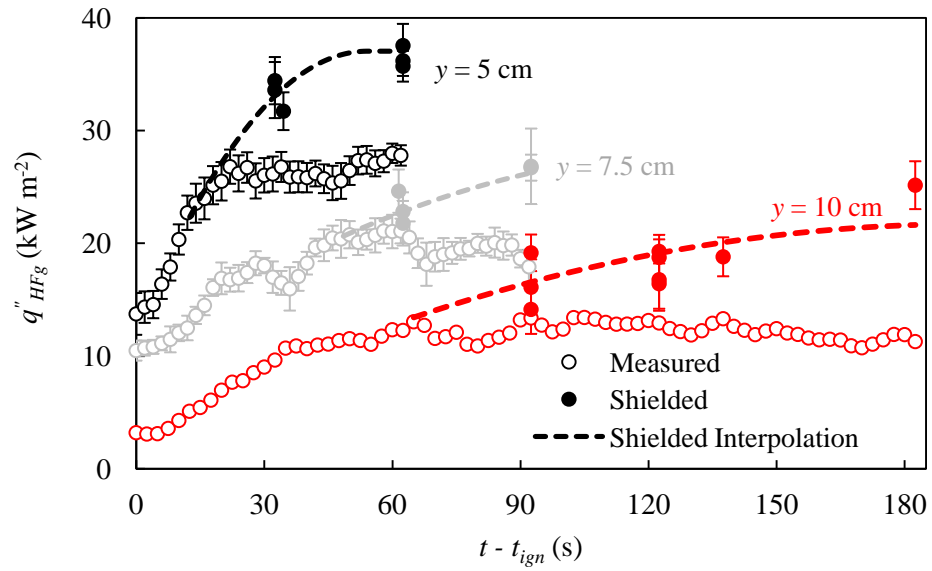


Figure 45. Measured HIPS flame heat flux at $y = 5, 7.5,$ and 10 cm

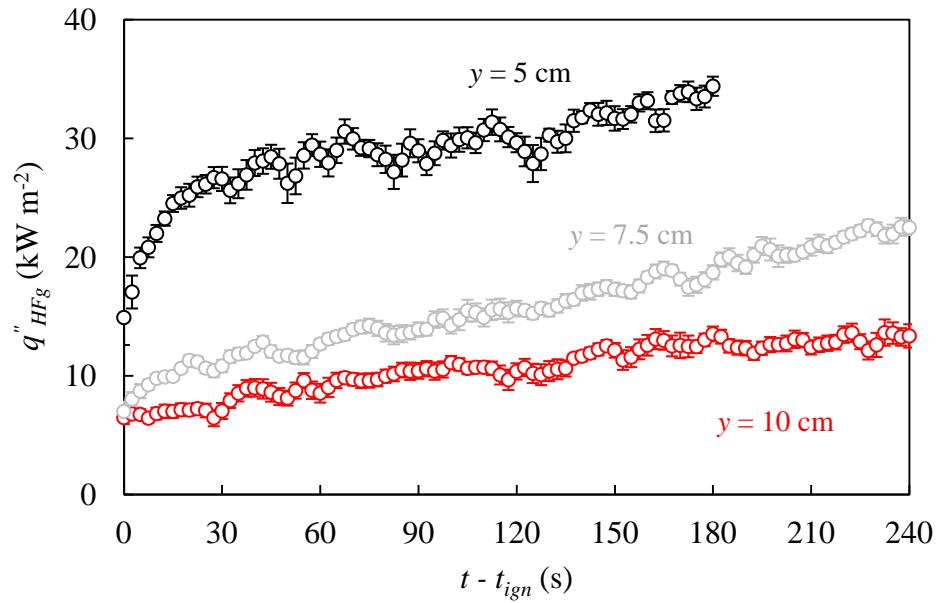


Figure 46. Measured FRP flame heat flux at, $y = 5, 7.5,$ and 10 cm

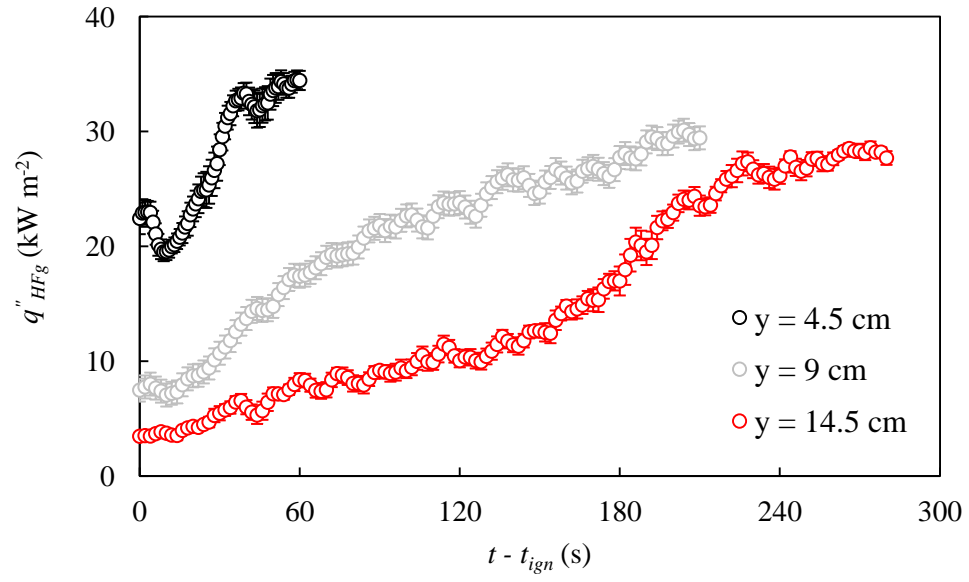


Figure 47. Measured PBT flame heat flux at $y = 4.5, 9,$ and 14.5 cm

4.4.2.3 Accounting for movement of the base of the flame

Throughout the duration of experiments, for all materials tested in this work except ABS and PMMA_{CAST}, the base of the flame either moved upward, due to sample burnout, or downward, due to polymer melt flow. The location of the base of the flame, y_b , was tracked throughout the duration of each experiment (both mass loss rate and flame heat flux tests) by video review and the time at which it reached 0.5 – 1.0 cm intervals above or below the base of the sample ($y = 0$) was recorded. As seen in Fig. 48, a representative time needed for y_b to reach each measurement location can be calculated as the average time (red square) recorded from all individual tests (black circles), and an expression can be fitted (solid line) to these results to capture the dependence of y_b on t . This analysis was repeated, as needed, for each of the materials tested here and the resulting fitted profiles are piecewise defined as per eqn. 33 with the constants provided in Table 6.

$$y_b = d_0 + d_1(t - t_{ign})$$

Equation 33

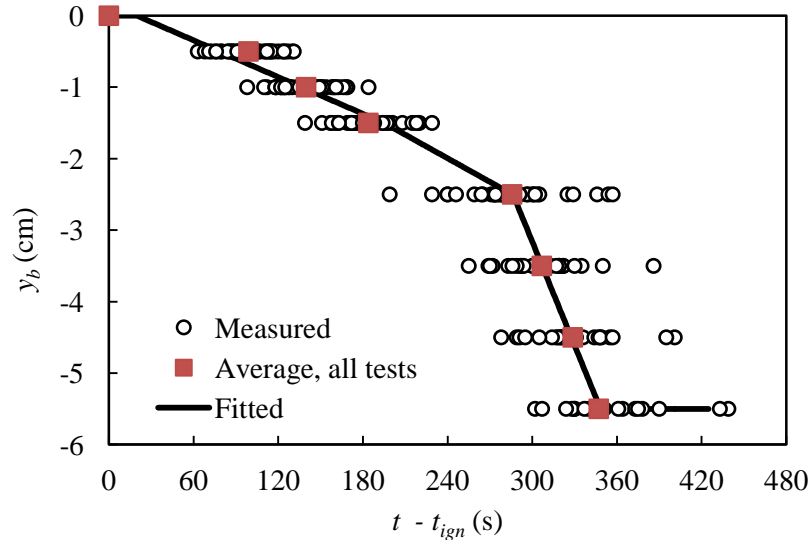


Figure 48. Base of flame location, y_b , during upward flame spread over PMMA_{EXT}

Table 6. Coefficients used in eqn. 33 to define the location of the base of the flame, y_b , supported by each material as it burns during flame spread experiments

Material	Valid for	d_0 (cm)	d_1 (cm s ⁻¹)	Movement Direction
	$t - t_{ign}$ (s)			
ABS	0 - 480	0	0	–
FRP	0 - 287	0	1.74×10^{-3}	Upward
	287 - 415	-0.72	4.24×10^{-3}	
HIPS	0 - 182	0	-2.74×10^{-3}	Downward
	182 - 330	0.35	-4.66×10^{-3}	
PBT	0 - 188	0	2.66×10^{-3}	Upward
	188 - 450	-1.07	8.36×10^{-3}	
PMMA _{CAST}	0 - 600	0	0	–
PMMA _{EXT}	0 - 20	0	0	Downward
	20 - 195	0.17	-8.57×10^{-3}	
	195 - 286	0.65	-1.10×10^{-2}	
	286 - 348	11.4	-4.84×10^{-2}	
POM	348 - 480	-5.5	0	Downward
	0 - 126	0	-3.97×10^{-3}	
	126 - 365	0.29	-6.28×10^{-3}	
PP	365 - 430	-2.0	0	Downward
	0 - 50	-0.34	-3.13×10^{-3}	
	50 - 325	-0.23	-5.44×10^{-3}	
	325 - 400	-2.0	0	

4.4.3 Heat of Combustion

Table 7 provides measured heats of combustion – $\Delta H_{c \text{ heat } H}$, $\Delta H_{c \text{ heat } V}$, $\Delta H_{c \text{ } 0 \text{ } H}$, and $\Delta H_{c \text{ } 0 \text{ } V}$ – for each of the materials studied in this work. In the horizontal configuration, tests are repeated with an external heat flux of $q_{ext}'' = 30 - 50 \text{ kW m}^{-2}$. Variation of q_{ext}'' within this range produced no significant impact on measured heat of combustion thus the results of these tests were averaged together to provide a single measured value of $\Delta H_{c \text{ heat } H}$. $\Delta H_{c \text{ heat } H}$ measured here shows excellent agreement with reference values [90], differing, on average, by less than 4%, which is within the accuracy of this measurement technique [89]. In fires, combustion is never complete [69]; thus each of these heats of combustion, which were obtained in cone calorimeter experiments, are less than their respective heats of complete combustion, $\Delta H_{c \text{ complete}}$. In this work, $\Delta H_{c \text{ complete}}$ measurements are obtained from colleagues' recent publications [60] [90] [91] based on experiments conducted in a Microscale Combustion Calorimeter (MCC) [92]; these measurements are included in the second column of Table 7.

The MCC heats 2 – 5 mg samples through controlled thermal decomposition at a constant heating rate (here, between 10 and 60 K min⁻¹) under anaerobic conditions. Gaseous volatiles produced by the sample are mixed with an inert carrier gas (nitrogen) and then brought to a 900 °C combustion chamber where they are forced to complete combustion in an oxygen rich environment. $\Delta H_{c \text{ complete}}$ is determined by measurement of oxygen consumption in the carrier gas stream and total sample mass loss; this value may be referred to in the literature as the “specific heat of combustion of specimen gases ($h_{c, \text{gas}}$)” [92]. For POM, which is heavily oxygenated – oxymethylene consists of more than 50%, by mass, oxygen – heat of combustion measurements obtained by oxygen

consumption calorimetry are inaccurate. Thus, for POM, $\Delta H_{c \text{ complete}}$ is determined on the basis of bomb calorimetry measurements [93].

Table 7. Heat of combustion (reported in units of kJ per gram volatilized mass)

Material	$\Delta H_{c \text{ complete}}$	$\Delta H_{c \text{ heat } H}$	$\Delta H_{c \text{ heat } V}$	$\Delta H_{c \text{ } 0 \text{ } H}$	$\Delta H_{c \text{ } 0 \text{ } V}$
ABS	36.5 ^A	28.4	29.3	---	31.0
FRP	22.2 ^B	20.5	20.4	---	23.9
HIPS	39.2 ^A	27.8	30.2	---	30.1
PBT	23.1 ^C	21.6	---	---	20.2
PMMA _{EXT}	24.5 ^A	23.8	24.2	---	20.0
PMMA _{CAST}	24.5 ^A	24.4	24.0	25.3	21.3
POM	15.9 ^D	14.9	14.6	---	11.8
PP	41.0 ^A	37.9	37.7	40.2	31.7

^A Lyon et al. [90]; in this reference, no distinction is made between cast and extruded PMMA

^B Martin et al. [60]

^C Raffan et al. [91]

^D Walters et al. [93]

To highlight the impact of burning conditions on measured heats of combustion, Fig. 49 plots experimentally measured $\Delta H_{c \text{ complete}}$, $\Delta H_{c \text{ heat } H}$, $\Delta H_{c \text{ heat } V}$, and $\Delta H_{c \text{ } 0 \text{ } V}$ of each material tested in this work. Here, error bars indicate the $\pm 5\%$ accuracy associated with calculating heat release from a fire on the basis of oxygen consumption measurements [89]. $\Delta H_{c \text{ } 0 \text{ } H}$ measurements are not included in this figure as they were only obtained for two materials studied here. One notable result of these tests is the reduction in measured heat of combustion – $\Delta H_{c \text{ } 0 \text{ } V}$ versus $\Delta H_{c \text{ heat } H}$ – by approximately 14%, on average, for PBT, PMMA_{CAST}, PMMA_{EXT}, POM, and PP. This indicates a decrease in combustion efficiency as these materials burn in the vertical configuration used for flame spread experiments versus in the standard configuration [3] of cone

calorimeter tests. ABS, FRP, and HIPS samples do not show this reduced combustion efficiency when burning in the vertical configuration without an external heat flux.

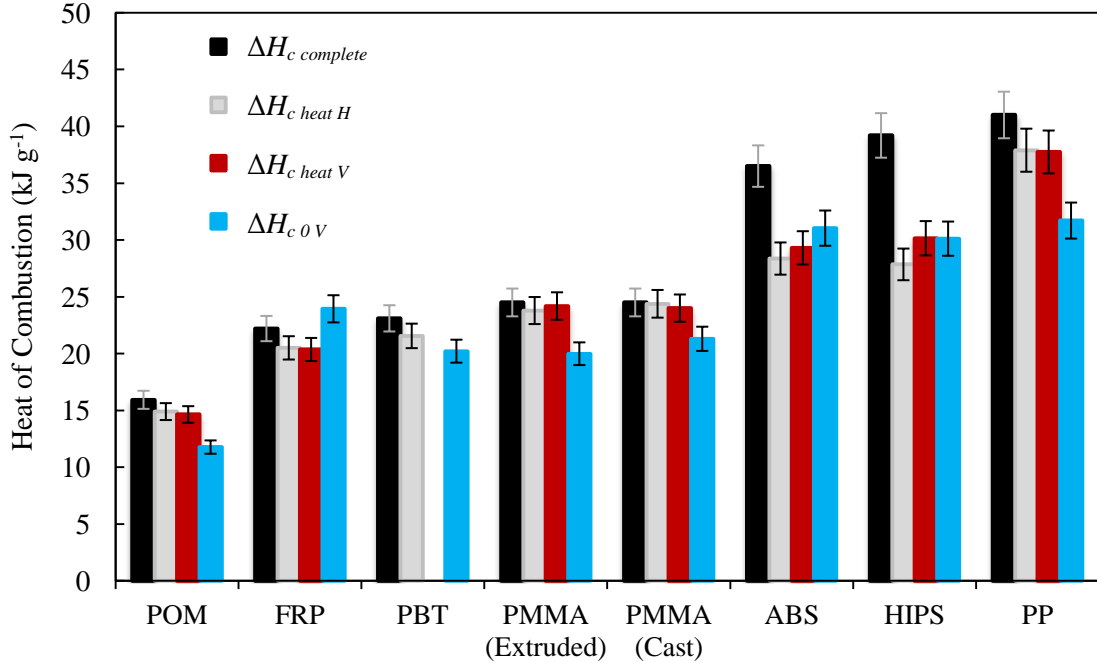


Figure 49. Measured heat of combustion (kJ per gram volatilized mass) of ABS, FRP, HIPS, PBT, PMMA, PMMA_{CAST}, PMMA_{EXT}, POM, and PP

It is possible that the reduction in combustion efficiency measured as PBT, PMMA, POM, and PP samples burn in the vertical configuration without external heating is due, at least in part, to the flame's contact with the comparatively cooler surface of a material that is not yet pyrolyzing. In these tests, samples are ignited at their base and a flame is allowed to propagate upwards in the absence of an external heat flux. Thus, throughout a majority of these experiments, the flame is in contact with, and loses energy to, the relatively cooler surface of the material, which must heat up before it begins pyrolyzing. In $\Delta H_{c \text{ heat V}}$ tests, however, samples are exposed to an external heat flux of $q_{\text{ext}}'' = 30 \text{ kW m}^{-2}$ prior to (and throughout) burning and so they uniformly ignite across

their entire surface. Consequently, throughout the duration of these tests, flames are never in contact with a surface below the pyrolysis temperature of the material, typically between 650-725 K [56]. Correspondingly, a decrease in combustion efficiency due to flame cooling is not expected or observed in these tests.

For ABS, FRP, and HIPS samples burning in the vertical configuration, a reduction in combustion efficiency is not observed regardless of the application of external heat; however, throughout the majority of tests on these materials, flames are separated from the polymer by an inert layer, which can heat up quickly. For ABS and HIPS samples, this layer develops due to deposition of a dark, thick, low density soot layer across the surface of the material. FRP samples are composed of 50 % (by weight) glass, which is embedded in the material in layers parallel to and no more than 0.5 mm from its front surface. As the polyester resin in these samples burns away, a residual glass matrix is left behind. Both this glass layer and the soot deposited on the surface of ABS and HIPS samples can act as thermal insulators that can maintain a high temperature, without degrading, when in direct contact with a flame. Consequently, these materials likely support higher surface temperatures while burning and thus the combustion efficiency of the flames that they support should not be reduced due to cooling of the flame at the sample's surface.

When materials burn in the horizontal configuration, regardless of the presence or absence of external heating, flames are not in direct contact with the sample's top surface. Thus, in this configuration, a decrease in combustion efficiency will not be caused by flame cooling due to flame contact with the sample's surface. This was verified by burning PMMA and PP samples in the horizontal configuration in separate cone

calorimeter experiments both with and without an external heat flux. Heat of combustion measurements were similar between these tests with $\Delta H_{c,0,H}$ measuring, on average, 5% higher than $\Delta H_{c,heat,H}$ (note: this difference is just within the uncertainty of these measurements [89]). In tests without an external heat flux, peak sample burning rate was approximately one third of that measured in tests with an external heat flux. Thus, it is speculated that this slight increase in $\Delta H_{c,0,H}$ with respect to $\Delta H_{c,heat,H}$ is a result of the smaller, and therefore more efficient flames supported throughout the duration of horizontal burning experiments when $q_{ext}'' = 0$.

Measurements of CO and CO₂ production – presented in Table 8 as the ratio of the mass fraction of CO in the carbon oxides of combustion ($CO_x = CO + CO_2$) – can be used as a quantitative measure of combustion efficiency. CO/CO_x ratios presented in this table were calculated on the basis of the average CO and CO₂ concentrations measured during the same time period analyzed for heat of combustion measurements (see Fig. 27 and the related discussion in Section 4.3.2). CO/CO_x ratios measured in this study agree reasonably well (within 30%, on average) with reference values found in literature, which were measured in over-ventilated cone calorimeter tests conducted in the horizontal configuration under a 50 kW m⁻² external heat flux [90].

Table 8. CO/CO_x ratios (%) as a function of material and burning configuration

Material	Method 1	Method 2	Method 3	Method 4
	Horizontal	Horizontal	Vertical	Vertical
	$q_{ext}'' = 0 \text{ kW m}^{-2}$	$q_{ext}'' = 30 - 50 \text{ kW m}^{-2}$	$q_{ext}'' = 0 \text{ kW m}^{-2}$	$q_{ext}'' = 30 \text{ kW m}^{-2}$
ABS	---	3.2	3.1	3.7
FRP	---	2.4	2.9	3.8
HIPS	---	3.3	3.1	3.0
PBT	---	2.1	2.4	---
PMMA _{EXT}	---	0.7	2.1	0.6
PMMA _{CAST}	0.7	0.7	2.1	0.7
POM	---	0.3	1.5	1.0
PP	1.1	1.4	2.3	1.2

Fig. 50 plots a selection of these results in order to better visualize the relationship between changes in CO/CO_x ratios (relative CO production) and heats of combustion measured as samples burn in the vertical configuration without external heating (Method 3, $\Delta H_{c,0V}$) versus in the horizontal configuration with an external heat flux (Method 1, $\Delta H_{c,heat,H}$). As seen here, there is an inverse relationship between CO/CO_x ratio and heat of combustion in each of these burning configurations. In other words, for each material tested here, relative CO production increases as heat of combustion decreases and vice versa. Specifically, the most significant increase in relative CO production is measured in the same tests when the greatest reduction in heat of combustion (with respect to $\Delta H_{c,heat,H}$) is observed. This confirms that, for materials tested in this work, measured changes in ΔH_c^{MATL} that accompany variations in burning conditions are due, at least in part, to changes in gas phase combustion efficiency. Additionally, this result shows that reductions in $\Delta H_{c,0V}$ with respect to $\Delta H_{c,heat,H}$ are not due to the escape (without burning) of pyrolyzate from the sides of these wall flames (see discussion of the potential impact of this behavior in Section 4.3.2).

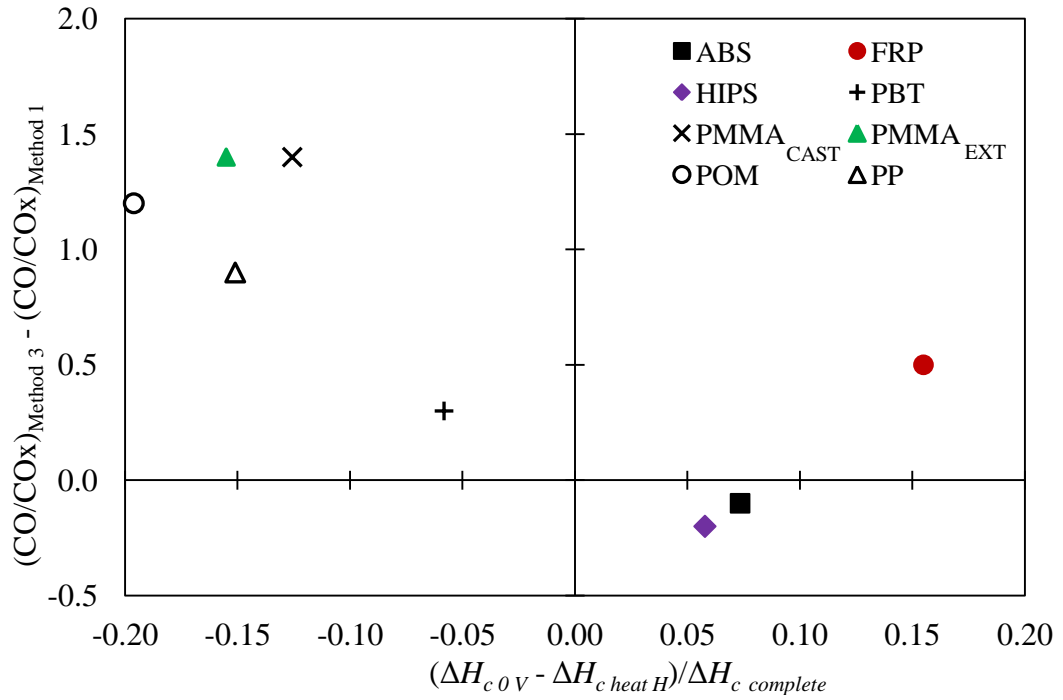


Figure 50. Changes in relative CO production and heat of combustion of samples burning in the vertical condition without external heating versus in the horizontal configuration with external heating

4.4.4 Model Generalization

Fig. 51, plots the dependence of flame height, y_f , on PMMA_{EXT} mass loss rate, $\frac{dm'}{dt}$. Here, red diamonds indicate original measurements (which assume that the base of the flame is fixed at the base of the sample, see Section 2.5), and black squares define flame height as the highest position, y_{eff} (distance from the base of the flame), at which measured flame heat flux reaches 97.5% of q''_{steady} . In this figure, error bars represent two standard deviations of the mean, as calculated based on a propagation of errors resulting from variations in the time at which y_f reaches the measurement location during each test and scatter in measured $\frac{dm'}{dt}$. As seen here, accounting for movement of the base of the flame has a notable impact on model predictions of data from larger flames. With this correction for movement of the base of the flame, the observed dependence of y_f on $\frac{dm'}{dt}$ is best captured by eqn. 34 where a , P , and b are empirical constants equal to 189, 0.459, and -6.91, respectively, when y_f and $\frac{dm'}{dt}$ are expressed in cm and $\text{g s}^{-1} \text{cm}^{-1}$.

$$y_f = a \left(\frac{\Delta H_c^{\text{MATL}}}{\Delta H_c^{\text{PMMA}_{\text{EXT}}}} \frac{dm'}{dt} \right)^P + b \quad \text{Equation 34}$$

Note: eqn. 34 is identical to eqn. 27 but is has been repeated here for clarity and to accompany the new values of the empirically derived constants a , P , and b defined here. Additionally, when this expression is used to define the behavior of PMMA_{EXT} flames,

the ratio $\frac{\Delta H_c^{\text{MATL}}}{\Delta H_c^{\text{PMMA}_{\text{EXT}}}}$ is simply equal to 1.

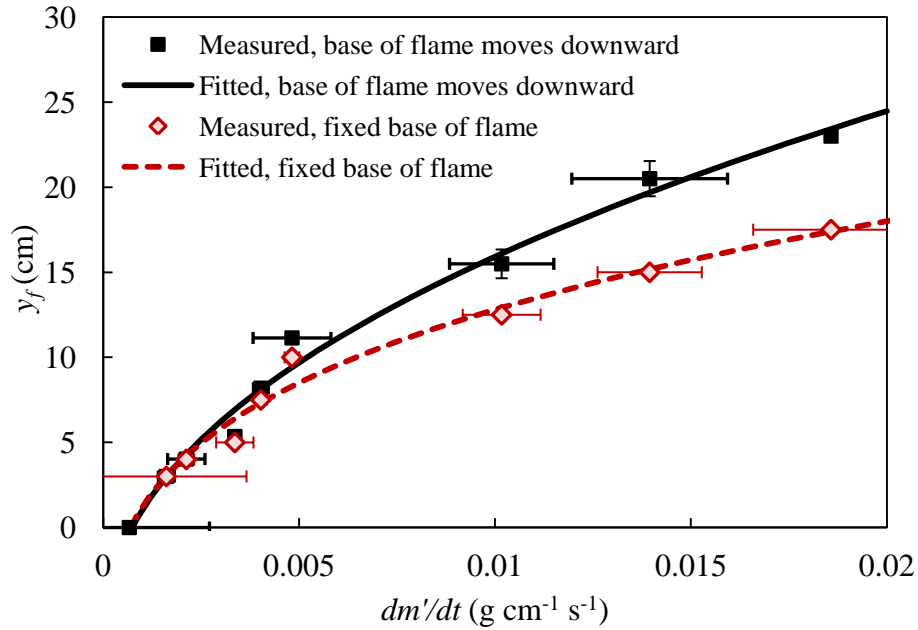


Figure 51. Effect of movement of the base of the flame on the relation between flame height and width-normalized mass loss rate during upward flame spread over PMMA_{EXT}

With this improved flame height expression, PMMA_{EXT} flame heat flux measurements, which were obtained at nine locations between $3 \leq y \leq 20$ cm, can be reevaluated following the analysis procedure described in Section 2.5 of this work. A single characteristic heat feedback profile for the entire flame – which captures measurements taken across the full height of samples, from ignition until full sample involvement – is still well captured by the original framework of our model when eqn. 12, which defines a normalized flame length scale, y^* , is adjusted to account for movement of the base of the flame as:

$$y^* = \frac{y_{eff} + y_0}{y_f + y_0} \quad \text{Equation 35}$$

Here⁸ $y_0 = 3.75$ cm is an empirically derived constant, which necessitates a corresponding definition of $\alpha_f = 1.79$ in eqn. 29. This refined flame model (eqns. 28 – 30, 34, and 35) accurately characterizes experimental measurements of PMMA_{EXT} flame heat flux with no systematic under- or over-prediction of the data. Total flame heat transfer across the surface of the material, $\int_{3cm}^{20cm} q_{HFG}''$, is calculated to within +/- 5% of measured values at any given time during experiments, which matches the accuracy of our original model predictions (see Section 2.5).

The ability of this refined flame model to predict heat feedback from flames supported by a variety of materials is validated here in two stages. First, its ability to account for polymer melt flow supported by a material for which the base of the flame does not move identically as during PMMA_{EXT} tests is validated by a series of experiments on PMMA_{CAST}. As described in Sections 2.3 and 4.4.1.1 of this work, PMMA_{EXT} and PMMA_{CAST} show markedly different dripping and polymer melt flow behavior while burning in the vertical configuration; however, scaling is not needed in the model to account for differences in heat of combustion between these two materials. Fig. 52 shows experimentally-measured and model-predicted flame heat flux at $y = 15$ cm during upward flame spread over PMMA_{CAST}; as seen here, the two show excellent agreement. As the development of this refined flame model is wholly independent from experimental measurements of PMMA_{CAST}, this demonstrates the model's ability to accurately calculate flame heat feedback regardless of changes in y_b as a material burns.

⁸ Note: although the form of eqns. 12 and 35 are similar, the constants y_0 and α_f are uniquely defined for each expression.

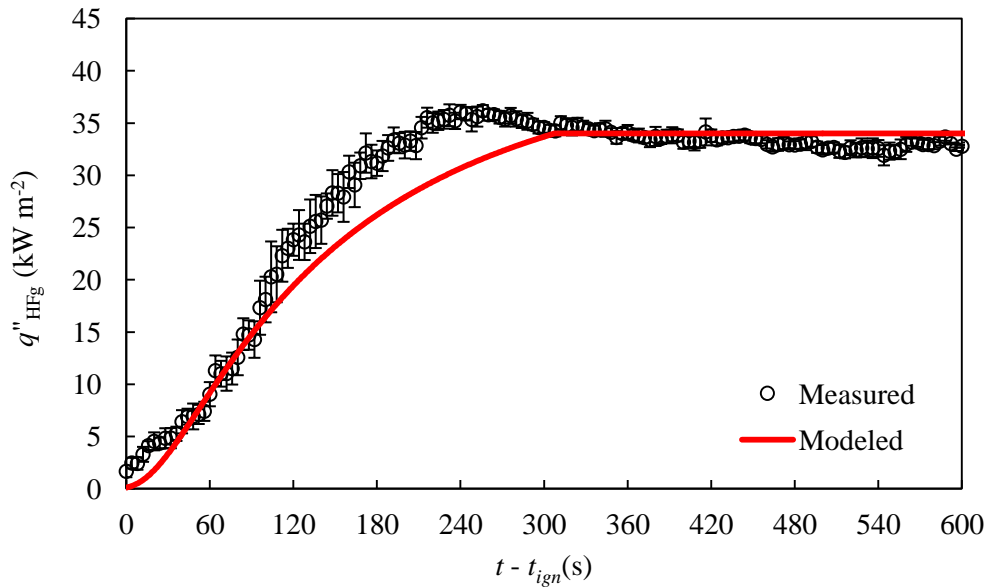


Figure 52. Experimentally-measured and model-predicted PMMA_{CAST} flame heat flux at $y = 15$ cm

Now that this flame model has been validated to accurately account for movement of the base of the flame, it is possible to analyze its ability to predict the flame heat feedback profile of a range of different materials. This generalized flame model calculates wall flame heat feedback by scaling of the expressions that calculate flame height and maximum flame temperature on the basis of a material's heat of combustion. As previously discussed, a material's heat of combustion can vary with burning conditions thus a parametric study was performed to determine which measured heat of combustion value allows the generalized model to provide, on average, the most accurate predictions of flame heat flux of each of the materials tested here. Five scaling methods were attempted. In methods 1 – 3, flame height and peak flame temperature were both calculated using either $\Delta H_{c \text{ complete}}$, $\Delta H_{c \text{ heat H}}$, or $\Delta H_{c 0 \text{ v}}$. These values were selected for this analysis because they represent, respectively, two widely used, standard definitions

of a material's heat of combustion and a value that captures combustion inefficiencies of materials burning in the vertical configuration used during flame spread tests.

In method 4, which is designed to account for radiative losses from the flame, $\Delta H_{c, \text{heat } H}$ of each material was reduced by one minus the material's radiant fraction as: $(1 - \chi_r) \times \Delta H_{c, \text{heat } H}$. This scaling approach recognizes that only a fraction $(1 - \chi_r)$ of the total energy release from a fire is carried within the fire plume itself while the remainder is radiated away in all directions [94]. For each material, χ_r was obtained as the average value reported in studies conducted by Tewarson [69] [95] [96] [97] and Quintiere et al. [98]; a detailed description of this determination of χ_r is provided in a colleague's recent work [99]. A final means of scaling was considered in method 5 in which $(1 - \chi_r) \times \Delta H_{c, \text{heat } H}$ was used in eqn. 34 so that flame height scaling would account for the reduced combustion efficiency of flames burning in this configuration but $\Delta H_{c, \text{complete}}$ was used to calculate $T_{fl, \text{adiabatic}}^{MATL}$ because, near the base of the flame where conditions are well-ventilated, complete combustion should occur.

Table 9 provides a summary of calculated $T_{fl, \text{adiabatic}}^{MATL}$ and h_{flame} values as along with reference values of χ_r for each material tested in this work. All other model parameters used in eqns. 28 – 30, 34, and 35 are defined without adjustment as introduced previously in this section. Peak flame heat feedback calculated by this model is calculated as a function of a material's adiabatic flame temperature, $T_{fl, \text{adiabatic}}^{MATL}$ as per eqns. 28 and 29. Here, $T_{fl, \text{adiabatic}}^{MATL}$ is calculated by assuming complete combustion of a stoichiometric mixture of the fuel (represented by its monomer) in air to produce CO₂ and H₂O (no minor species) with temperature dependent heat capacities as defined in the

NIST Chemistry Webbook [70]⁹. For all materials, h_{flame} is correspondingly defined as a single constant value across the length of the flame. For each scaling method, a unique value of h_{flame} is defined such that, when it is substituted into eqn. 29 along with the adiabatic flame temperature of PMMA_{EXT}, $T_{fl,adiabatic}^{PMMA_{EXT}}$, previously measured (see Section 2) values of q''_{steady} are correctly calculated. It is important to note that h_{flame} is an effective value that captures both the dominant convective and minor radiative components of flame to surface heat transfer.

Table 9. Flame model input parameters: $T_{fl,adiabatic}^{MATL}$, h_{flame} , and χ_r

Heat of combustion value used for calculation of $T_{fl,adiabatic}^{MATL}$ and h_{flame}	$\Delta H_{c\ complete}$	$\Delta H_{c\ heat\ H}$	$\Delta H_{c\ 0\ v}$	$(1 - \chi_r) \times \Delta H_{c\ heat\ H}$	
h_{flame} (kW m ⁻² K ⁻¹)	0.0196	0.0202	0.0236	0.0288	
Material	$T_{fl,adiabatic}$ (K)				χ_r [99]
ABS	2405	1977	2116	1261	0.46
FRP	2277	2140	2413	1549	0.35
HIPS	2457	1881	1998	1205	0.46
PBT	2286	2169	2059	1638	0.31
PMMA _{EXT}	2327	2275	1989	1678	0.33
PMMA _{CAST}	2327	2320	2087	1709	0.33
POM	2407	2288	1913	1928	0.20
PP	2294	2157	1882	1420	0.43

⁹ The MATLAB script used to perform these calculations is provided in the appendix.

To quantify the accuracy of each of these scaling methods, the absolute difference between experimentally-measured (or shielded interpolated) and model-predicted q_{HFg}'' was calculated at each time step throughout the duration of tests. Table 10 provides a summary of this analysis. As shown here, model generalization by Method 1 – $\Delta H_{c, complete}$ used to scale flame height (eqn. 34) and to calculate adiabatic flame temperature (eqn. 28) – provides the most accurate correlation between experimentally-measured and model-predicted flame heat flux. With this scaling approach, throughout the duration of tests, model-predicted flame heat feedback across the full length of the flames supported by all seven materials studied here differs from experimental measurements, on average, by just 3.9 kW m^{-2} .

Such high accuracy is particularly notable when compared to the wide variation in flame heat fluxes reported in other studies (both experimental and modeling) of flames at this scale. Consider a recent review by Pizzo et al. [100] that summarizes six studies in which peak flame heat flux was measured at $y < 30 \text{ cm}$: although only a single material, PMMA, was tested in each of these works, flame heat fluxes were reported to vary by up to 20 kW m^{-2} . Additionally, in a review by Tsai et al. [33] of ten different studies that modeled upward flame spread over a range of different wall materials, peak (steady) flame heat fluxes were shown to vary between 20 and 35 kW m^{-2} .

Table 10. Absolute difference between measured and model-predicted q''_{HFg} (kW m⁻²) for each material, averaged throughout the duration of experiments across all measurement locations, y

Material	Method 1	Method 2	Method 3	Method 4	Method 5
	$y_f \sim \Delta H_{c \text{ complete}}$ $T_{fl} \sim \Delta H_{c \text{ complete}}$	$y_f \sim \Delta H_{c \text{ heat H}}$ $T_{fl} \sim \Delta H_{c \text{ heat H}}$	$y_f \sim \Delta H_{c \text{ 0 v}}$ $T_{fl} \sim \Delta H_{c \text{ 0 v}}$	$y_f \sim (1-X_r) \Delta H_{c \text{ heat H}}$ $T_{fl} \sim (1-X_r) \Delta H_{c \text{ heat H}}$	$y_f \sim (1-X_r) \Delta H_{c \text{ heat H}}$ $T_{fl} \sim \Delta H_{c \text{ complete}}$
ABS	5.4	6.6	5.9	12.5	3.7
FRP	2.2	4.0	12.4	7.4	3.9
HIPS	3.7	9.2	2.4	14.7	10.7
PBT	5.2	5.1	6.3	3.4	6.0
PMMA _{CAST}	2.1	2.0	2.1	2.0	1.9
POM	7.4	7.7	8.6	7.1	8.0
PP	1.7	2.1	2.2	6.0	4.0
Average	3.9	5.2	5.7	7.6	5.4

Figs. 53 – 59 demonstrate the accuracy of model-predicted flame heat flux. Model predictions shown here are calculated on the basis of scaling by $\Delta H_{c \text{ complete}}$. From a material development perspective, it is particularly beneficial that model scaling by $\Delta H_{c \text{ complete}}$ provides the most accurate predictions of measured flame heat flux as this value can be determined using mg-scale tests conducted in the MCC. This suggests that flame behavior at this scale can be predicted on the basis of a small number of tests conducted using limited quantities of a material. Note: For clarity, unshielded measurements of ABS and HIPS flame heat flux are not plotted in Figs. 55 - 57 when shielded, ‘clean gauge’ data is available. A discussion on how the shielded interpolation curves plotted in these figures are calculated is included in Section 4.4.1.3 of this work.

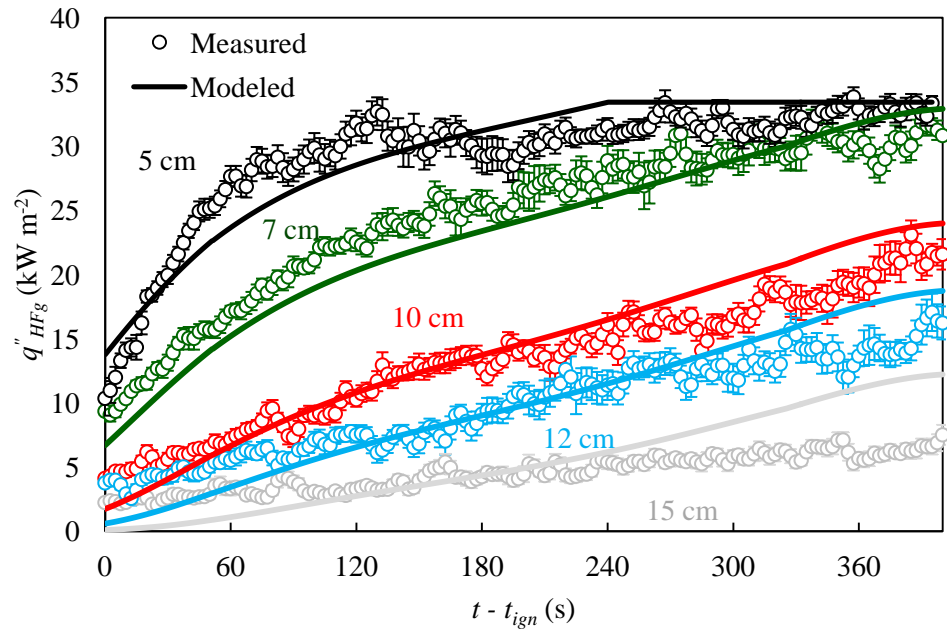


Figure 53. Experimentally-measured and model-predicted PP flame heat flux at five locations above the base of the sample, $y = 5, 7, 10, 12,$ and 15 cm

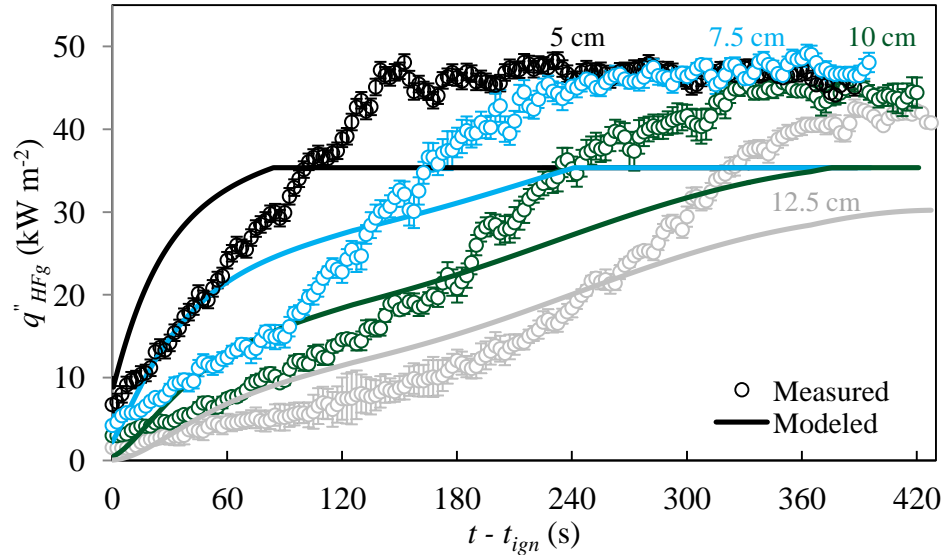


Figure 54. Experimentally-measured and model-predicted POM flame heat flux at four locations above the base of the sample, $y = 5, 7.5, 10,$ and 12.5 cm

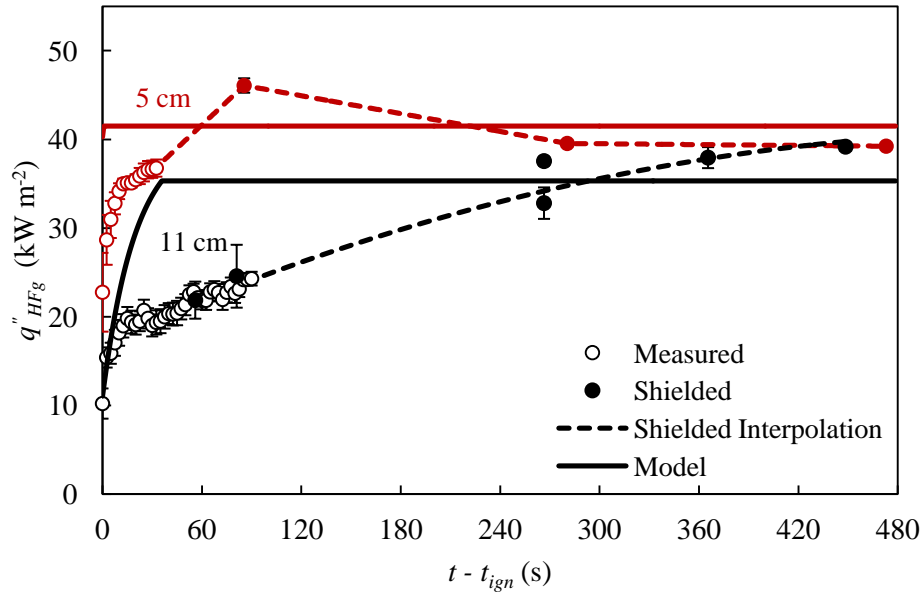


Figure 55. Experimentally-measured and model-predicted ABS flame heat flux at two locations above the base of the sample, $y = 5$ and 11 cm

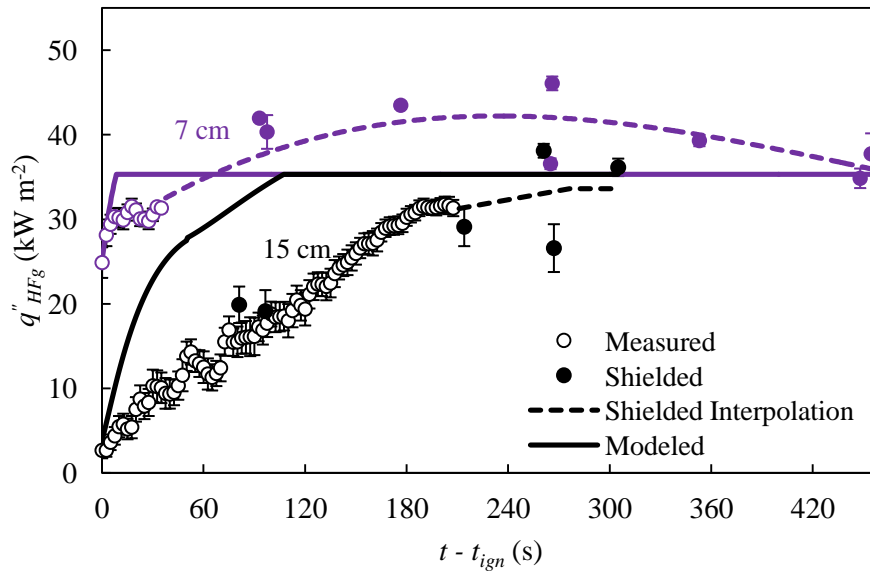


Figure 56. Experimentally-measured and model-predicted ABS flame heat flux at two locations above the base of the sample, $y = 7$ and 15 cm

¹⁰ Note: Figs. 55 and 56 both contain heat flux measurements from the same material, ABS. These results have been separated into two figures for clarity (to avoid overlap in plotted values).

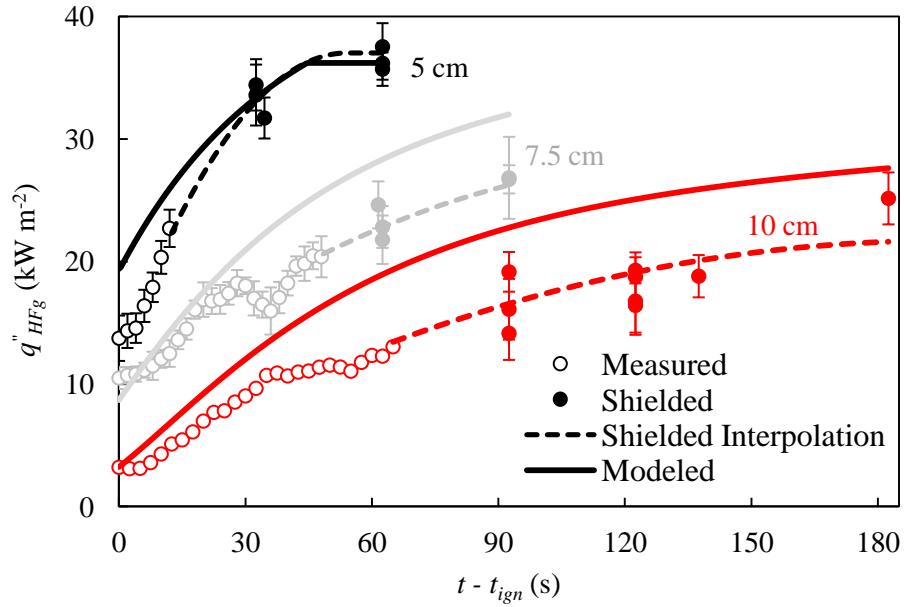


Figure 57. Experimentally-measured and model-predicted HIPS flame heat flux at three locations above the base of the sample, $y = 5, 7.5,$ and 10 cm

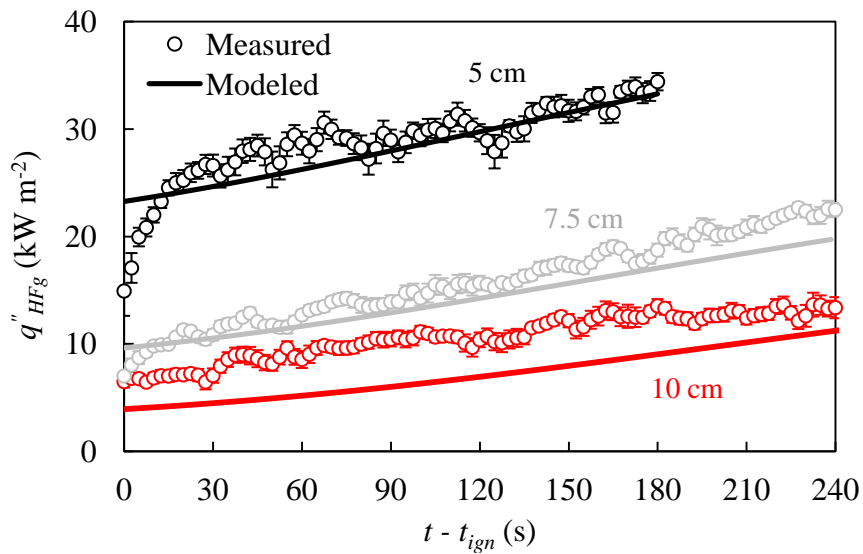


Figure 58. Experimentally-measured and model-predicted FRP flame heat flux at three locations above the base of the sample, $y = 5, 7.5,$ and 10 cm

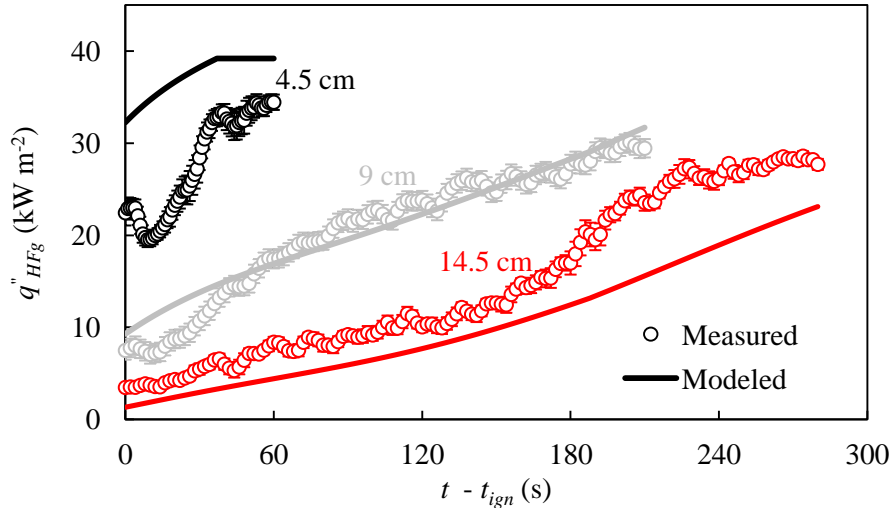


Figure 59. Experimentally-measured and model-predicted PBT flame heat flux at three locations above the base of the sample, $y = 4.5, 9,$ and 14.5 cm

Although the generalized flame model presented here is quite accurate, it systematically under-predicts measured POM flame heat fluxes. For this model to best match measurements of POM flames, model-predicted peak flame heat flux would have to increase by approximately 16 kW m^{-2} and the empirical parameters a , P , b , and y_0 in eqns. 34 and 35 would require a corresponding adjustment so as to avoid over-prediction of heat flux downstream of y_f . As heat transfer in this system occurs primarily by convection, higher POM flame heat fluxes may arise due to increases in either h_{flame} or $T_{fl,adiabatic}^{POM}$. A review of calculated flame temperatures (Table 9) shows that, even with corrections for radiation losses, $T_{fl,adiabatic}^{POM}$ is not expected to be significantly greater than $T_{fl,adiabatic}^{PMMA}$ so as to completely account for the observed differences in flame heat flux. This suggests that a reduction in h_{flame} can be expected for POM flames, likely as a result of a reduction in the flame to surface standoff distance or due to an increase in the temperature gradient in the gas phase near the wall. An analysis of flame standoff

distance was attempted by comparing a series of high resolution images taken from the sides of both POM and PMMA flames of several heights. Although PMMA flames thickened throughout the duration of experiments while POM flames did not, these results are insufficient to draw conclusions from. To definitively quantify the nature of this discrepancy in measured flame heat flux, highly spatially resolved measurements of the temperature gradient in these flames, normal to the material's surface, are necessary.

A key difference between POM flames and those supported by each of the other materials tested in this work is that they remain transparent and blue from their base up to their tips throughout the full duration of tests. The yellow color of flames supported by each of these other materials results from blackbody radiation from soot; this soot layer is found on the fuel rich side of the flame between the flame sheet (combustion zone) and the sample's surface. Fig. 60, which is based upon the thermal model of wall flame spread first presented in Fig. 1, presents a simplified depiction of the primary features of this system. Here, the flame sheet is represented as an ideal thermal boundary layer, TBL (red curve) and the presence of the soot layer is indicated by a thin dashed line, as is its impact on the temperature profile (black curve) in the gas phase of this system, normal to the sample's surface. Blackbody radiation from this soot layer removes a small fraction of energy from the flame sending some of it back towards the sample's surface and the rest out to the environment; this is indicated in Fig. 60 by the arrows labeled q_{rad}'' . Although radiative losses are not great for wall flames at this scale this energy removal reduces the temperature gradient, $\frac{\partial T}{\partial x}$, close to the surface of the sample. Because heat transfer in this system is dominated by $\frac{\partial T}{\partial x}$ at this location and because the cooling due to radiative

losses occurs here (at small x) minor decreases in temperature due to blackbody radiation may have a significant impact on measured flame heat flux and on heat transfer into the material itself.

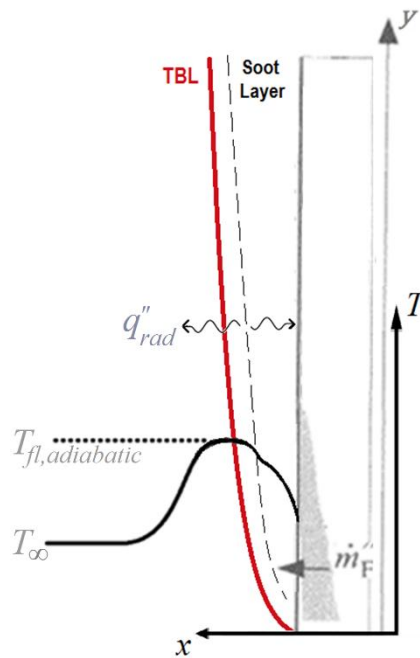


Figure 60. Simplified thermal model for surface flame spread highlighting flame heat losses due to blackbody radiation from soot

An independent series of experiments was conducted to test this hypothesis by measuring flame heat flux (q''_{HFg}) at two locations, $y = 3.5$ and 7 cm, from wall flames supported by 8 cm tall, vertically oriented wicks soaked with one of three fuels: methanol, ethanol, or heptane. In each experiment, y_f was well above the measurement location, y , thus q''_{HFg} remained fairly constant throughout the duration of experiments. Methanol and ethanol flames each remained primarily transparent across their length whereas heptane flames were bright yellow and produced soot in sufficient quantities

such that it could be observed rising beyond the flame tips in each test. Measured heat flux from heptane flames was significantly lower than that of flames supported by the other two fuels (approximately 32 versus 40 kW m⁻²). This decrease is similar to, though lower in magnitude than, the measured reduction in q''_{steady} of each of the polymeric materials tested in this work when compared to q''_{steady} of POM. Although these measurements are preliminary and additional testing is needed before definitive conclusions can be made, these results support the hypothesis that, even for small, primarily laminar wall flames, soot production (or lack thereof) may have a strong impact on flame to surface heat transfer.

Although a wall flame model could be developed on the basis of measurements of POM flames, such a model would not be representative of the burning behavior supported by each of the other materials tested here (or that of most non-premixed flames); the purely transparent, blue flames supported by POM are unique to this material. Thus, POM is not a suitable candidate to serve as the foundation material upon which our flame model is based even if, arguably, such a model might be considered simpler and more fundamental than one that implicitly includes reductions in flame heat transfer due to soot production. Consequently, the baseline wall flame model developed on the basis of extensive measurements of PMMA flames, which implicitly includes minor radiation effects on flame heat transfer in its definition of the heat transfer coefficient, h_{flame} , is maintained as the foundation for our generalized flame model.

The flame heat feedback modeled developed here can be compared to others in the literature by considering the flame heights predicted or measured in each work. To make this comparison, measured PMMA_{EXT} burning rate is scaled by its heat of complete

combustion, $\Delta H_{c, complete}$, such that flame heights measured here can be expressed as a function of width-normalized heat release rate: $Q' = (\Delta H_{c, complete}) \times \left(\frac{dm'}{dt}\right)$. These results are plotted in Fig. 61 along with a collection of related measurements from several theoretical and experimental studies. This study is unique in that it offers experimental measurements of small flames ($y_f < 8$ cm), because this model has been validated to describe the behavior of flames supported by a wide range of solid fuels, and because measurements are not confined to either the purely laminar or turbulent regimes.

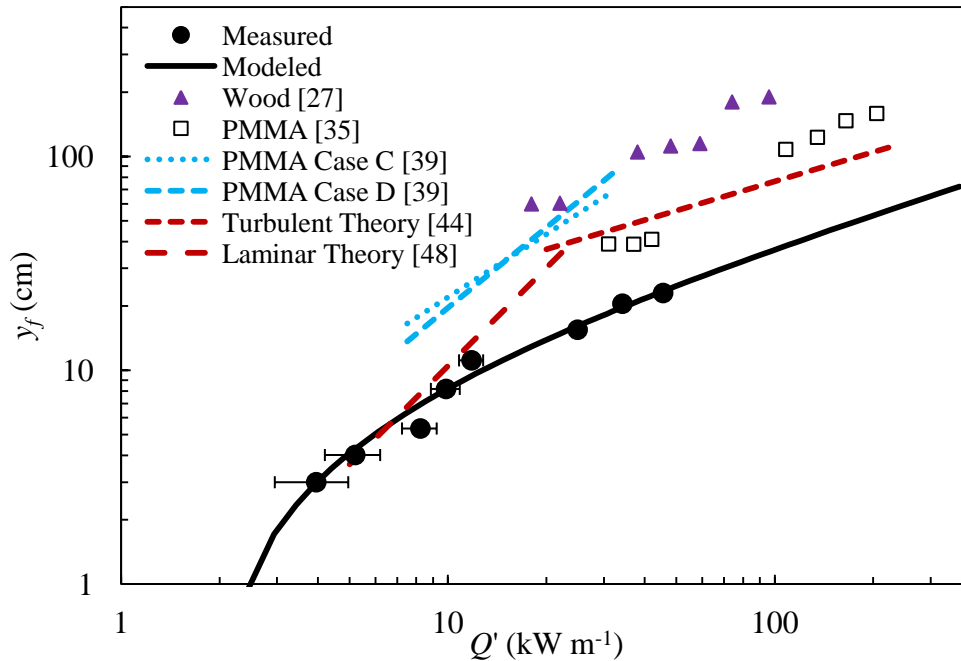


Figure 61. Comparison of flame height correlation developed in this work to literature values

As seen in Fig. 61, flame heights measured in this work and predicted by eqn. 34 are lower than those reported in other works; however, the functional dependence of y_f on

Q' observed here is consistent with these other studies. One key reason for this discrepancy is that, in this work, y_f is defined quantitatively as the highest position in the flame where measured flame heat flux is within 2.5% of q''_{steady} rather than by visual observations, which are subjective, often overestimate flame height, and may vary from one researcher to the next. In the reference works presented in Fig. 61, y_f is typically defined as the farthest extent of flame tips. As seen in Fig. 62, which shows a representative image of flame spread over a 15 cm tall PMMA_{EXT} sample 270 s after ignition, typically, visible flame tips extend well beyond y_f as defined by a threshold value of flame heat flux. Here, this sample supports a flame height of $y_f = 12$ cm (as defined by flame heat flux); however, flame tips can be seen reaching, on average, up to and beyond $y = 20$ cm.



Figure 62. Flame height comparison during upward flame spread over PMMA_{EXT}

5. Model Applications

5.1 Modeling of Standard Flammability Tests – UL 94 and ISO9705

The modeling framework presented in this manuscript offers a path for development of rigorous quantitative relationships between flammability test standards. A clear first choice to consider is the UL94V¹¹ Flammability Test [6], which is one of the most common standard test methods used to assess flammability of plastic materials. As seen in Fig. 63, UL94V is a bench scale test that is conducted by supporting small, rectangular samples of a material (125 ± 5 mm tall, 13.0 ± 0.5 mm wide; no thicker than 13 mm) in the vertical configuration and igniting them at their base by a premixed methane burner. Unfortunately, although widely applied, material performance in this test is assessed only on a qualitative ranking scale, thus limited information is gained that can elucidate the governing the dynamics of observed material burning behavior.

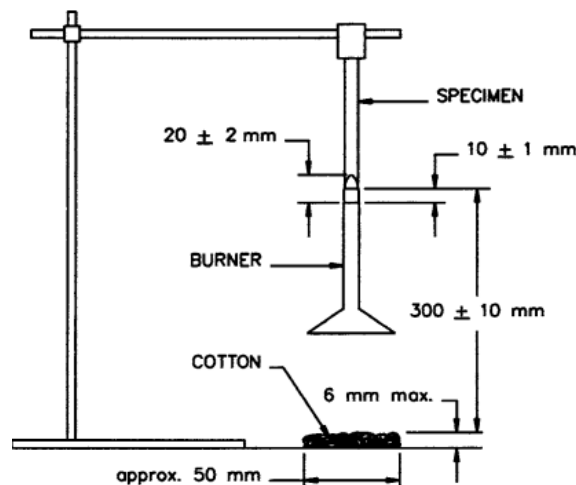


Figure 63. UL94 test setup for samples burning in the vertical configuration

¹¹ UL94 is actually comprised of several separate tests; here we focus only on the vertical burning test, UL94V, as it is most closely related to the upward flame spread system studied in this work.

Although this test is simple to perform, the controlling dynamics of material burning behavior during the experiment are remarkably complicated – in addition to the primary constituent processes controlling upward flame spread (detailed in Section 1 of this manuscript) three-dimensional burning effects alter ignitability and burning rate towards the edges and corners of samples, polymer melt flow and dripping often has a strong impact on material performance during the test, and small variations in the ignition procedure can produce significant changes in the test outcome. Two recent studies present advanced models designed to simulate material behavior in the UL94V test [78] [101]; however, each of these works is significantly limited in their predictive capabilities due to inadequate descriptions of heat feedback from the sample flame. In one [78], flame heat flux is simply defined as a constant value (between 58.6 and 74.9 kW m⁻²) from the base of the flame up to a measure of flame height, and zero farther downstream. In the other [101], flame heat flux is prescribed as “decreasing with the square of the path in the upward direction” from 150 kW m⁻² at the base of the sample. As demonstrated by experimental measurements presented in Sections 2 and 4 of this manuscript, neither of these descriptions is sufficient to accurately describe flame heat feedback in this system.

The flame model presented in this work provides an accurate, highly spatially resolved description of flame heat transfer at the length scale of interest in UL94V tests. A logical extension of our modeling capabilities is thus to simulate UL94V experiments in ThermaKin2D. This can be accomplished by approximating samples as two-dimensional material objects and prescribing our flame model as the boundary condition (after sample ignition) on either side of the material. Although such an approach assumes that the impact of three-dimensional burning effects is negligible, it offers a reasonable

estimation of heat transfer in this system, which is the primary controlling mechanism of the rate of upward flame spread. Further, in these experiments, sample thickness is typically 3 mm or below (samples are ~ 4 - 5 times thinner than they are wide) thus the application of a two dimensional model is a reasonable approximation. This approach is expected to provide accurate predictions of the relevant fire dynamics of this system.

A key limitation that prevents us from running this simulation in ThermaKin2D is the lack of reliable measurements of flame heat transfer from the methane burner used for sample ignition in these tests. This is critically important as it has been well known for decades [24] [25] that upward flame spread is sensitive to initial ignition conditions. Several recent works [78] [101] [102] provide experimental measurements or numerical models that approximate heat transfer from the UL94V burner; however, each is inconsistent with the other – reported peak burner heat fluxes in these three works vary between, 60, 94, and 125 kW m⁻². To address this challenge, we have constructed a test apparatus matching the specifications of the UL94 test standard [6] and we have begun the process of carefully characterizing heat transfer from the burner used for sample ignition at the start of these tests. Once accurate measurements of burner flame heat feedback have been obtained and these measurements validated, this information can be used to define the initial boundary conditions needed to simulate UL94V tests in ThermaKin2D.

In a colleague's recent work [103] our unified model of material degradation and burning was used to simulate burning behavior of medium density fiberboard (MDF) in the full scale ISO 9705 Room/Corner Test [104]. The goal of this project was to develop a method to measure the relevant properties of a material needed to define its degradation when subjected to the room corner test using milligram- and bench-scale experiments

conducted in the MCC and the cone calorimeter. Full scale experiments were also conducted in this work in which flame heat flux was measured across the length wall flames (up to 2 m tall) observed in these tests. These heat flux measurements could be accurately described using the expressions for flame height and heat flux distribution presented in Section 4 of this manuscript. The empirically derived constants in these equations – a , P , b , y_0 , and α_f – were adjusted to provide this agreement with experimental results; however, these minor changes can be expected given the change in scale (flames in the room corner test are fully turbulent unlike the laminar flames studied during wall flame model development) and sample configuration (radiative heat feedback from opposite walls and reduced air entrainment in the room corner test versus the open in wall flame model development experiments). Despite these differences in experimental conditions, the fundamental form of the wall flame model describing heat transfer in this system remains unchanged; this suggests that the wall flame model developed here accurately captures the relevant physics of the problem.

As seen in Fig. 64, model predictions (width-normalized heat release rate, Q') of initial material degradation in response to the methane burner used as an ignition source in the Room Corner Test as well as the rate of rise of heat release rate during upward flame spread over the wall lining material are quite accurate. Time to ignition could not be perfectly predicted by the model for all materials studied in these experiments; however, this value showed great variability in experiments, varying by up to a factor of four between similar materials. These results demonstrate the accuracy of the physics incorporated in our wall flame model.

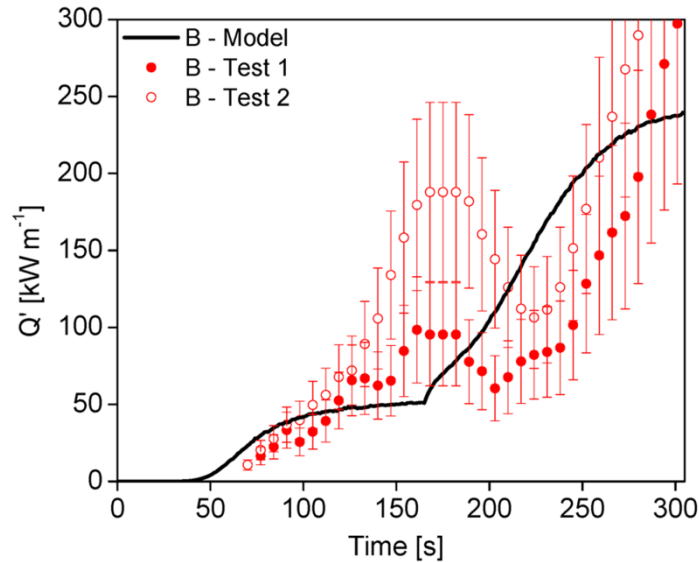


Figure 64. Measured and model-predicted width-normalized heat release rate, Q' , of medium density fiberboard samples during the ISO 9705 room corner test [103]

5.2 Mechanisms of Action of Flame Retardants During Upward Flame Spread

To improve their resistance and response to fire conditions or simply to meet fire safety regulations and standards, flame retardants are often added to combustible materials such as the polymers tested in this work. Typically, these flame retardants work by interfering with pyrolysis (e.g. promoting char formation) in the condensed phase of the material, reducing gas phase combustion efficiency, or both. In recent decades, the use of flame retardants has drastically increased, with market demand estimated at \$2.3 billion. Due to their relatively low cost and high effectiveness, approximately 36% of this market share can be attributed to brominated flame retardants (BFRs) [105] via. [106]. With the rapid expansion in their use, BFRs have been found across the environment in the atmosphere, soil and sediment, bodies of water, and in the tissue of invertebrates, fish, birds, and mammals [107]. This bioaccumulation has evoked growing concern with

regards to the environmental hazards these flame retardants pose [108] and thus industry is moving towards developing safer and equally effective replacements.

To develop new, efficient flame retardants, it is crucial to understand the exact mechanisms by which they inhibit flaming combustion. The experimental procedure and generalized flame model presented in this manuscript provide the foundation to quantify these mechanisms of action. Here, a series of experiments was conducted in which flame heat transfer and sample mass loss rate were measured as a flame spread over 7 cm tall, 5 cm wide glass-reinforced PBT samples manufactured with increasing amounts (12, 16, and 24 wt %) of the brominated flame retardant, poly(pentabromobenzyl acrylate) (trade name: FR 1025). In an additional series of tests, similar measurements were obtained for PBT samples manufactured with increasing amounts (8, 12, 16, and 20 wt %) of the phosphorous-based flame retardant, aluminum diethyl-phosphinate (trade name: DEPAL). These tests allow for the study of the impact of flame retardants on three key features of the system: flame height, peak flame heat flux, and flame stability.

PBT samples used in these tests were prepared and supported in the sample holder identically as per the procedure described in Section 2.2 of this manuscript. Sample ignition could not be achieved using the non-premixed propane burner and so a premixed burner was built. This premixed burner was positioned 1.5 cm below the bottom edge of samples and provided 0.6 and $0.3 \text{ L min}^{-1} \pm 1\%$ (at 1 atm and 298 K) of methane and oxygen, respectively. These flow rates were measured by a Bios Defender 530 flow meter and regulated using separate needle valves. To limit the area of the sample preheated by the burner and to provide reproducible and well-defined ignition conditions, the burner flame was restricted by a steel shield positioned horizontally above the base of

the sample. As seen in Fig. 65, this configuration provides a constant, well defined heat flux to the sample throughout the duration of its exposure that is, on average, approximately 60% higher (20 – 25 kW m⁻² greater) than that of the non-premixed propane burner in its final configuration.

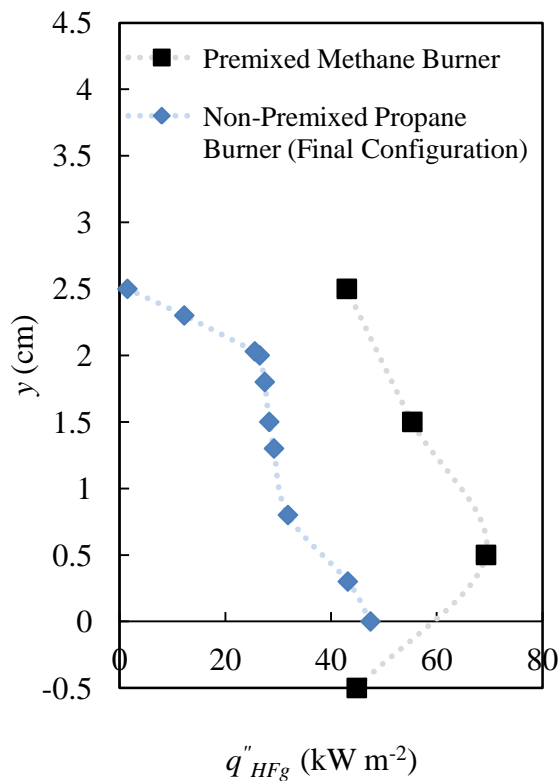


Figure 65. Measured heat feedback from burners used for sample ignition

In each test, prior to burner application, an external heat flux of 10 kW m⁻² was applied across the front surface of samples using a radiant heater (see Fig. 3). Following this preheating, the pre-mixed burner was positioned and left in place just long enough for sustained, uniform ignition of each sample along its bottom edge. After sample ignition, the burner was removed and the radiant heater was repositioned to provide a 20 kW m⁻² heat flux to the sample’s surface. Due to the application of the radiant heater prior to and after sample ignition, steady flaming conditions were observed across the

surface of the sample throughout the majority of experiments. A summary of preheat and burner application times required for ignition of each of these PBT samples is provided in Table 11. PBT samples with 24 wt % FR 1025 could not be ignited by the premixed methane burner; instead sample ignition was achieved by application of a handheld, premixed propane torch. In all tests, samples were allowed to burn until auto-extinction of the flame. Tests are repeated three times each; measurements from repeated tests are averaged together and this combined dataset is further smoothed using a 5 s running average prior to further analysis.

Table 11. Sample preheat and burner application times for PBT samples with various concentrations of bromine- and phosphorous-based flame retardants.

Flame Retardant Concentration	Sample Preheat Duration	Burner Application Duration (t_{ign})
12 % FR 1025	300 s	30 s
16 % FR 1025	600 s	20 s
24 % FR 1025	720 s	10 s *
8 % DEPAL	420 s	20 s
12 % DEPAL	420 s	40 s
16 % DEPAL	600 s	55 s
20 % DEPAL	600 s	70 s

*PBT samples with 24 wt % FR 1025 were ignited by a handheld, premixed propane torch applied to the lower 3 cm of the sample

Fig. 66 shows measured flame heat flux, q''_{HFg} , at $y = 7$ cm from flames supported by PBT samples with increasing concentrations of FR 1025. In these tests, steady flaming conditions are observed across the surface of each sample within 10 s of ignition thus measured q''_{HFg} remains quasi-steady throughout the majority of tests until sample

extinction. Note: in Fig. 66, q''_{HFg} has not been corrected to remove the additional heat provided by the radiant heater ($q''_{ext} = 20 \text{ kW m}^{-2}$). These small, primarily transparent flames should not absorb or block a significant amount of the radiation provided by the external heater thus, as a first order approximation, flame to surface heat transfer can be approximated by reducing q''_{HFg} measurements shown here by 20 kW m^{-2} . By this calculation, in tests on PBT samples with various concentrations of FR1025, $q''_{steady} \approx 30 \text{ kW m}^{-2}$, which is nearly identical to that measured from flames supported by PBT samples that are not treated with any flame retardant (Fig 47).

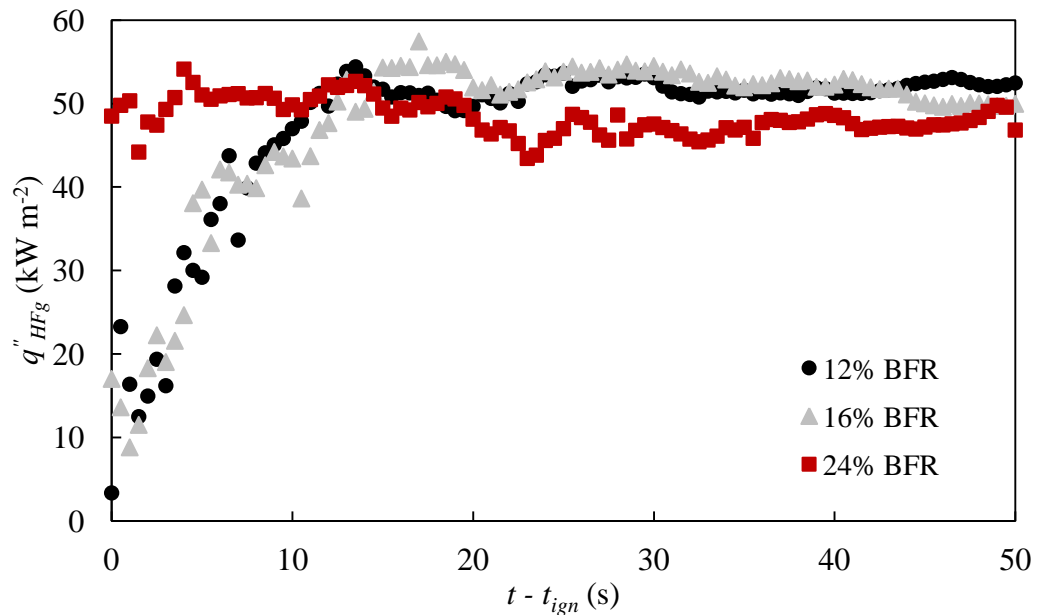


Figure 66. Measured flame heat flux at $y = 7\text{cm}$ from flames supported by PBT samples with increasing concentrations of a BFR, poly(pentabromobenzyl acrylate)

Note: Measurements shown here are not corrected to subtract the influence of the applied external heat flux, $q''_{ext} = 20 \text{ kW m}^{-2}$

These measurements highlight an important behavior – peak, steady flame heat flux, q''_{steady} , is not sensitive to BFR concentration. For PBT samples prepared with increasing concentrations of the phosphorous-based flame retardant DEPAL, char formation at the sample's surface produced non-uniform burning across the width of the sample; however, when steady flames could be observed in these tests, q''_{steady} was similarly unaffected by flame retardant concentration. These measurements indicate that bromine- and phosphorous-based flame retardants do not affect flame to surface heat transfer in this system, provided that a flame is present.

The results of these experiments are quantitative, reflect the dynamics of flame spread, and do not require oxygen consumption measurements (which are time consuming and complicated to obtain). Ongoing analysis of sample mass loss rate measured in these experiments is directed towards determining the minimum width-normalized mass loss rate required for sustained flaming ignition (a measure of flame stability) of these samples. Together, these results demonstrate the potential of small scale experiments to screen the performance of flame retardants, a useful tool for manufacturers of new, flame-resistant materials.

5.3 FDS Simulations

In this work, in addition to developing our empirical model of the flame, vertical burning and upward flame spread over 5 cm tall PMMA slabs has been modeled in a series of two-dimensional DNS simulations performed in the Fire Dynamics Simulator (FDS) developed by the National Institute of Standards and Technology (NIST) [32]. FDS simulations were performed at three mesh resolutions – fine, medium, and coarse; $\Delta x = \Delta y = 1 \times 10^{-4}$, 2×10^{-4} , and 4×10^{-4} m, respectively – using single-step, mixing-controlled combustion. Sample (material object) and model domain dimensions were identically defined for all FDS simulations to match those shown in Fig. 67. As seen here, a 5 cm tall, 5.9 mm thick PMMA sample was defined such that its back, top, and bottom surfaces were insulated by 6 mm thick layers of Kaowool PM insulation. Below the sample, this insulation layer extends downwards by 2 cm, followed by a 4 cm long, 1.6 mm thick layer of steel, which represents the sample holder; these dimensions match those used in experiments, providing a similar configuration to that shown in Fig. 2. A 5 cm tall Kaowool PM insulation layer was also defined at the sample's top edge to maintain a continuous surface downstream of the PMMA slab (as done in experiments). The presence of this insulation layer extended the top boundary of the modeling domain well beyond the top of the sample. This limited any losses of radiation heat transfer from the flame back to the sample and prevented flow instabilities that might arise at the top boundary of the domain from traveling back towards the sample. The modeling domain extends 6 cm outwards, normal to the front surface of the sample.¹²

¹² A copy of the input file defining a representative (fine grid) FDS simulation is provided in the appendix.

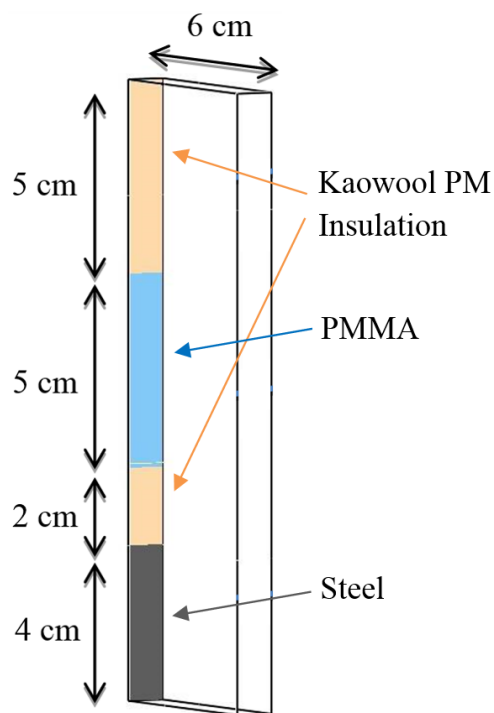


Figure 67. Visualization of material object and modeling domain in FDS simulations

Condensed phase material properties of the PMMA and Kaowool insulation used in these simulations are identical to those used in the ThermaKin2D simulations presented in Section 3.2 of this work (see Table 2). Material properties of the steel defined in this model have been obtained from the SFPE Handbook [109] and can be found in the appendix. PMMA is known to decompose by end-chain scission (unzipping) nearly completely (91 – 98 % by weight) to its monomer, methyl methacrylate (MMA) [110]. Thus, in these FDS simulations, the thermophysical properties of the gaseous volatiles produced by pyrolysis of PMMA are assumed to be equal to those of MMA vapor, which are obtained directly from material property handbooks [111] [112] or by using the correlations (i.e. structural grouping methods) of Joback or Fuller et al. [113]. A summary of these properties is provided in Table 12; here specific heat, thermal

conductivity, dynamic viscosity, and diffusivity (MMA vapor in air) are represented by the symbols, c , k , μ , and \mathcal{D} , respectively.

The propane burner used for sample ignition in these tests cannot be defined in FDS identically as in ThermaKin2D because, when flaming combustion is modeled in FDS, a convection heat transfer coefficient and a corresponding temperature (or temperature distribution) cannot be explicitly prescribed in the gas phase of the model domain. Thus, in FDS simulations, heat transfer from the propane burner (see Fig. 4) was defined as purely radiation. Although the prescribed burner heat flux profile matches experimentally measured values when the sample surface temperature equals that of the water cooled heat flux gauge used in experiments and even though FDS calculates reradiation from the sample's surface, when the burner flame is defined as purely radiation, net heat transfer into the sample is slightly overestimated as the sample's surface heats up. This occurs because, at this scale, flame to surface heat transfer is dominated by convection, which in turn is driven by the temperature gradient between the surface of the sample and the gaseous flow field above. As the sample's surface heats up, this convection heat transfer decreases; in these FDS simulations, this minor reduction in heat transfer from the burner flame is not simulated.

Table 12. Thermophysical properties of methyl methacrylate (MMA) vapor

Property	Temperature Range (K)	Value
c (kJ kg ⁻¹ K ⁻¹) ^A	$T < 288$	0.753
	$288 < T < 1000$	$(3.66 \times 10^{-11})T^3 - (1.44 \times 10^{-6})T^2 + (3.68 \times 10^{-3})T - 0.187$
	$T > 1000$	2.09
k (W m ⁻¹ K ⁻¹) ^B	$T < 373$	0.015
	$373 < T < 1000$	$(1.85 \times 10^{-8})T^2 + (5.64 \times 10^{-5})T - 0.0086$
	$T > 1000$	0.066
μ (kg m ⁻¹ s ⁻¹) ^C	$T < 373$	9.44×10^{-6}
	$373 < T < 1000$	$(5.09 \times 10^{-12})T^2 + (3.11 \times 10^{-8})T - 1.46 \times 10^{-6}$
	$T > 1000$	2.45×10^{-5}
\mathcal{D} (m ² s ⁻¹) ^D	$T < 288$	7.64×10^{-6}
	$288 < T < 1000$	$(3.80 \times 10^{-10})T^{1.75}$
	$T > 1500$	1.37×10^{-4}

^A Method of Joback via [113]^B Yaws [111]^C Yaws [112]^D Method of Fuller et al. via [113]

To reduce the computational costs of these FDS simulations, the first 80 s of sample preheating in response to the propane burner, prior to ignition, was simulated in ThermaKin2D, which was previously validated (see Section 3.3 of this work) to accurately calculate time to ignition and initial mass loss rate of PMMA samples. The in-depth temperature profile across the length of the sample calculated by ThermaKin2D was then used as an input to define the initial state of the material object in FDS. In FDS, the fine grid resolution simulation was run for approximately 3 months on four cores of a 3.1 GHz Intel Core I5 processor to provide 18 s of modeling time; medium and coarse grid resolution simulations were each run (on two and one core(s), respectively, of a 3.1 GHz Intel Core I5 processor) for approximately two months to provide 55 and 128 s of modeling time, respectively. In contrast, ThermaKin2D simulations required just 6 hours of CPU time on a single core of a 2.0 GHz Intel Xeon processor to provide 480 s of

modeling time; this represents a reduction in computational costs by two orders of magnitude with respect to FDS.

A preliminary analysis of simulation results is performed here by comparing net flame to surface heat feedback calculated in FDS and ThermaKin2D simulations. Recall: the flame model used in ThermaKin2D has been validated (see Sections 2.5 and 3.3.1 of this work) to accurately reproduce experimentally measured flame heat transfer in this system. A direct comparison of sample mass loss rates calculated by each model is not made here due to differences in predicted ignition time (t_{ign}) between FDS and ThermaKin2D simulations. Likely, the reduced ignition time calculated in FDS results from the different heat transfer mechanism (radiation vs. convection) used to describe the propane burner flame in either simulation tool.

Fig. 68 plots net flame heat flux, q_{net}'' , calculated by each FDS simulation (fine, medium, and coarse grid resolutions) at $y = 1$ and 5 cm both during burner application (sample preheating) and after burner removal (sustained flaming). Here, results are plotted versus time, $t - t_{preheat}$, where $t_{preheat} = 80$ s, the duration of sample preheating simulated in ThermaKin2D. As seen here, predicted flame heat fluxes are consistent between FDS simulations at each grid resolution: sample ignition is predicted to within 1 s between each simulation and, on average, throughout the length of simulations when measurements are available at each resolution, model-predicted q_{net}'' differs by less than 1 kW m⁻². Because of this similarity, flame heat fluxes predicted in the coarse simulation (which offers a longer modeling time and thus a larger dataset for analysis) can be treated as representative of FDS results obtained at finer resolutions. Thus coarse FDS simulations are used for comparison to ThermaKin2D simulations.

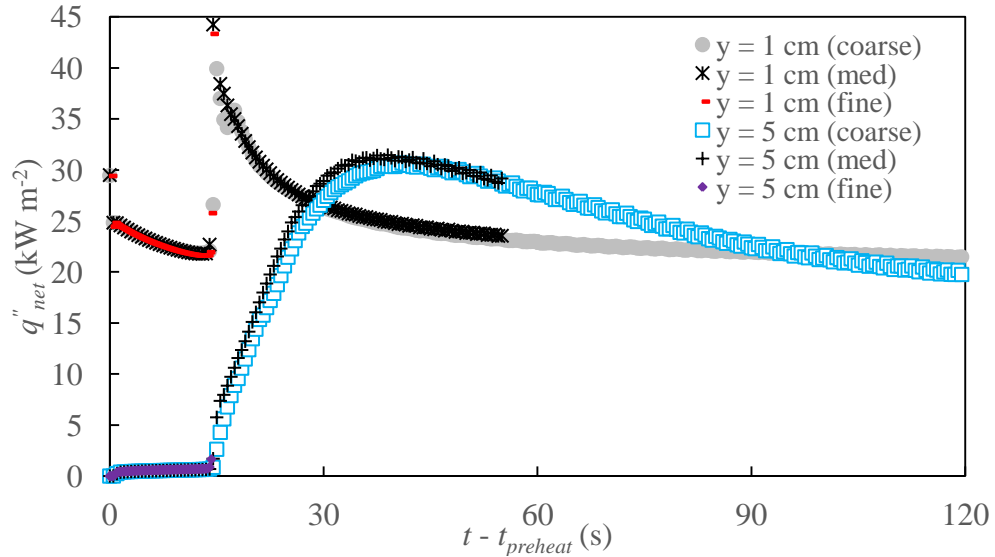


Figure 68. Predicted net flame heat flux in fine, medium, and coarse FDS simulations of vertical burning and upward flame spread over 5 cm tall PMMA samples

Fig. 69 presents net flame heat flux, q''_{net} , calculated by FDS and ThermaKin2D at $y = 1, 3,$ and 5 cm. Here, results are plotted versus time, $t - t_{ign}$, where t_{ign} represents the earliest time in each simulation at which a flame was observed. As seen in this figure, both maximum and steady flame heat fluxes are consistent between FDS and ThermaKin2D simulations. Similarly as in experimental tests, both models predict flame spread across the length of the sample within 30 s of sample ignition (as indicated by the measurement of peak flame heat flux at the top edge of the sample and thus the arrival of y_f at this location). Unlike experimentally-measured q''_{HFg} (see Figs. 10 and 11), however, model-predicted flame heat fluxes shown here decrease after peak values are observed, eventually reaching a steady value of approximately 23 kW m^{-2} at $1 \leq y \leq 5$ cm. These results are not inconsistent; this simply highlights the effect that increased sample surface temperature (due to pyrolysis) has on net heat flux into the material as it burns. At the

measurement locations shown here, quasi-steady net heat flux calculated in both FDS and ThermaKin2D (at $t - t_{ign} > 90$ s) are consistent with (differ by less than ~ 5 kW m⁻²) experimentally measured net heat flux from PMMA wall flames at this scale reported by Ito and Kashiwagi [9].

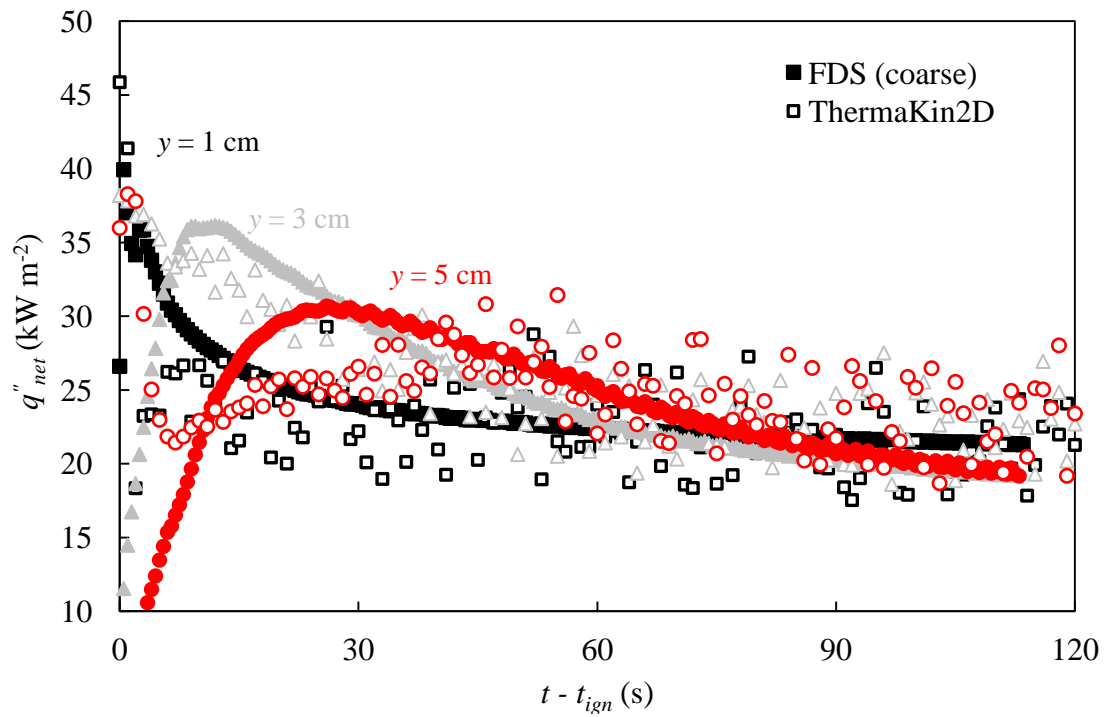


Figure 69. Predicted net flame heat flux in FDS and ThermaKin2D simulations of vertical burning and upward flame spread over 5 cm tall PMMA samples

It is important to emphasize that ThermaKin2D provides comparable accuracy as FDS in modeling the behavior of wall flames at this scale; however, ThermaKin2D offers a reduction in computational costs by two orders of magnitude. Although DNS modeling offers a more detailed description of the physics of the fire induced flow in this system, these simulations require a large amount of empirical data to produce accurate results – e.g. knowledge of the solid phase degradation mechanism and the primary products of pyrolysis as well as thermophysical properties of solid and gas phase constituent components of the reaction – which are not readily available for most fuels. Ongoing work is focused on exploring the sensitivity of FDS simulation results to these user inputs and determining the level of detail and accuracy needed in experiments and model parameterization to obtain reliable predictions of flame spread in this configuration.

6. Conclusions

In this work we present a new model of upward flame spread that was developed by combining a highly spatially resolved empirical model of flame heat feedback with a state-of-the-art computational pyrolysis solver. This unified model has been shown to accurately predict the relevant fire dynamics of this system without the prohibitive computational costs of CFD simulations. To create the flame heat feedback model used here, detailed measurements of mass loss rate and flame heat flux were carefully obtained as a flame spread vertically upwards over 20 cm tall, 5 cm wide samples of extruded PMMA. Flame heat flux was measured at nine locations above the base of the sample, $3 < y < 20$ cm. This sample size was selected as it represents the critical length scale at which, in likely ignition scenarios, flame spread is the most important hazard determining fire growth.

Peak, steady state flame heat flux, q''_{steady} , measured in these tests is highest near the sample's base and decreases slightly farther downstream, where it averages to a single value at larger heights ($5 < y < 20$ cm). This trend in q''_{steady} is consistent with the structure of the flame, which is thinnest (and thus closest to the material's surface) at the base of the sample. Using heat flux measurements recorded across the length of the flame, an analytical expression was defined that calculates a flame's entire heat feedback profile, expressed as a function of the distance from the base of the flame, solely as a function of width-normalized material mass loss rate. Model-predicted total flame heat flux, q''_{HFg} , is calculated within 5% of measured values at any given time during experiments.

Although wall flames have been studied for decades, much debate still remains regarding how to best define and predict flame height in wall fires, what exactly is the

correct magnitude of peak heat flux in the steady region of a flame, and how does flame heat flux behave farther downstream in the thermal plume, beyond the flame height, y_f . This flame model represents a significant advancement over similar scaling laws in the literature as it was developed on non-steady (spreading) flames, at the critical length scale of interest, and spanning both the purely laminar and laminar-to-turbulent transitional regimes. Additionally, flame height is defined here quantitatively, by a threshold value of flame heat flux (ultimately, the key factor of interest) rather than visually, as often prescribed for simplicity in other works. This model has been shown to accurately describe both very small flames observed shortly after ignition (i.e. $3 \leq y_f \leq 6$ cm) and flames up to 20 cm tall.

This model of the flame has been coupled with the solid phase pyrolysis solver, ThermaKin2D (which computes the transient rate of gaseous fuel production of a pyrolyzing solid from fundamental physical and chemical properties of its constituents) to produce a unified description of material degradation and burning. The pyrolysis model was parameterized using a combination of mg-scale thermal analysis experiments and g-scale gasification tests; the parameterization of this model is summarized in this work. Simulations of vertical burning of 4 cm tall extruded PMMA samples in response to steady flaming conditions were carried out and the predicted sample mass loss rate was found to closely match experimental measurements. This result confirms the accuracy of measured flame heat flux values and their parameterization in the model. Model predictions of flame spread behavior over 17.5 cm tall samples – including time to ignition and initial, peak, and rate of rise of sample mass loss rate – were also found to be in a good agreement with the corresponding experimental observations.

It should be emphasized that no parameters in the unified model were sampled from the literature or adjusted in any way to improve the agreement with the measured mass loss rate evolution. Thus, the degree of agreement represents a true indicator of the importance of the processes represented in the model. The unified model has been shown to simultaneously predict degradation of milligram-sized samples under linear temperature rise conditions, radiation driven gasification of material plates, and steady flaming and upward flame spread on such plates, where flame to material heat transfer is dominated by convection. Model parameterization and validation was performed through direct experiments on the same material across four orders of magnitude of length scale, from thermally thin to thermally thick. This unified model bridges a range of scales and offers a path for development of rigorous quantitative relationships between various flammability test standards.

Our research group has established a systematic methodology for pyrolysis model parameterization of both non-charring and charring polymers as well as for several composite materials for use in this unified model of material degradation. The flame model developed in this work has therefore been correspondingly generalized to accurately calculate heat feedback from flames supported by a wide range of materials through scaling of model expressions that calculate flame height and peak heat flux on the basis of the heat of complete combustion of the gaseous volatiles produced by a pyrolyzing solid, $\Delta H_{c \text{ complete}}$. This generalization is accomplished using experimental measurements of flame heat flux and sample mass loss rate obtained during upward flame spread over seven additional commonly used polymers – ABS, FRP, HIPS, PBT, PMMA_{CAST}, POM, and PP – two of which are glass reinforced composites. Each of these

materials presents a varied range of burning behaviors including dripping, polymer melt flow, sample burnout, and heavy soot and solid residue formation.

For these seven additional materials, model-predicted flame heat flux, q_{HFg}'' , is shown to match experimental measurements taken across the full length of the flame with an average accuracy of 3.9 kW m^{-2} (approximately 10 – 15 % of peak measured flame heat flux). Thus, this model of the flame unifies the widest range of solid fuel compositions of any flame model currently available in the literature. It is important to highlight that model generalization is accomplished on the basis of scaling by $\Delta H_{c \text{ complete}}$, which can be measured in mg-scale tests conducted in the MCC. This is particularly beneficial from a material development perspective because it suggests that flame behavior at this scale can be predicted on the basis of a small number of tests conducted using limited quantities of a material.

The unified model of material degradation developed here provides the framework to quantitatively study material burning behavior in response to a wide range of common fire scenarios with a level of accuracy and reduced computational cost unmatched by other currently available models. This work also demonstrates the potential of using small scale measurements for assessment of flame spread dynamics through modeling – an extremely useful capability for the development of new, flame resistant materials. Preliminary characterization of several secondary factors, which may impact upward flame spread, has also been presented in this work, including: the effects of finite width on sample burning behavior, peak flame heat flux, and flame heat flux distribution, the impact of soot deposition and char formation at a material's surface on flame heat transfer, determination of the flame to surface heat transfer mechanism (convection vs. radiation), and the mechanisms of action of bromine- and phosphorous-based flame retardants.

Appendix

A1. Determination of Steady State Flame Heat Flux, q''_{steady}

Plotted in Fig. A 1 is the average heat flux measured at $y = 17.5$ cm during upward flame spread over PMMA; the polynomial fit of this curve and its first derivative with respect to time, $\frac{dq''_{fitted}}{dt}$, are also included here. q''_{steady} represents the relatively constant (with respect to time) heat flux observed when the steady portion of the flame establishes itself above the gauge (where $y \leq y_f$). q''_{steady} is calculated as the average of experimentally measured flame heat flux recorded over the 30 s interval immediately following the earliest time at which $\frac{dq''_{fitted}}{dt} < 0.02 \text{ kW m}^{-2} \text{ s}^{-1}$ (bolded data points in Fig. A 1). At $y = 17.5$ cm, this is shown to occur just after $t - t_{ign} = 360$ s yielding: $q''_{steady} = 33.1 \text{ kW m}^{-2}$.

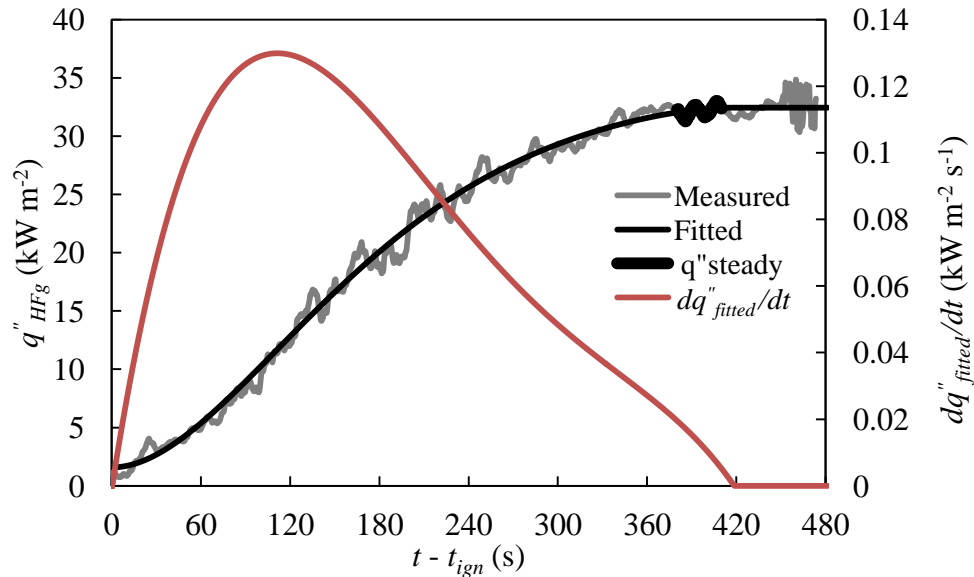


Figure A 1. Determination of steady state flame heat flux, q''_{steady} , at $y = 17.5$ cm for extruded PMMA wall flames

A2. Recessed Heat Flux Gauge Measurements

Measurements of radiation heat flux from wall flames can be recorded using a gauge that is recessed by a known distance into the front surface of the burning material. In these tests, the gauge is initially shielded by a layer of insulation (to prevent accrual of deposits at its front face) which is kept in place until the flame has spread and established itself above the gauge position (i.e. $y_f > y$). Flame heat flux is measured by removing the shield in front of the gauge, allowing the flame to stabilize for 10 – 20 s, and then quickly and completely extinguishing it. Reported values, $q''_{recessed}$, are calculated as the difference between heat flux measured just prior to flame extinction and that recorded shortly thereafter, once $\frac{dq''}{dt} > -1 \text{ kW m}^{-2} \text{ s}^{-1}$; this calculation effectively removes the impact that heated insulation sidewalls in front of the gauge have on measured heat flux.

Fig. A2 shows recessed heat flux gauge measurements from two representative tests of a propane wall flame. Here, the points used to calculate reported $q''_{recessed}$ for tests 1 and 2 are highlighted as $q''_{recessed} = 20.93 - 8.19 = 12.74 \text{ kW m}^{-2}$ and $q''_{recessed} = 20.19 - 6.76 = 13.43 \text{ kW m}^{-2}$.

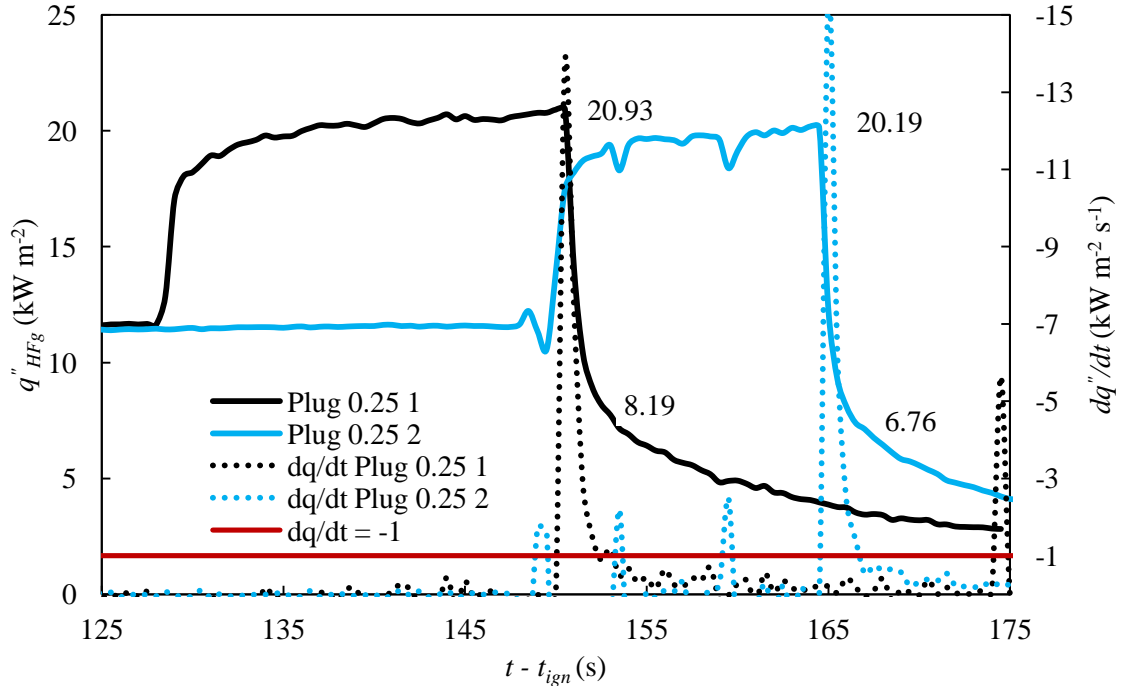


Figure A 2. Recessed gauge heat flux measurement of a propane flame taken at extinction. This same method is used for determining the heat flux to a recessed gauge in a burning sample of PMMA . Note, the secondary y-axis, $\frac{dq''}{dt}$, reports negative values.

Ideally, $q''_{recessed}$ could be measured before the insulating materials surrounding the gauge heat up. Unfortunately, this is not possible during tests of polymeric materials because recessed gauge measurements can only be analyzed later in each test, after q''_{steady} is observed at the measurement location (i.e. after $y_f > y$), in order to calculate

$$q_{rad}^{\%} = 100 \times \left(\frac{q''_{rad}}{q''_{steady}} \right). \text{ While waiting for the flame to spread upward and establish itself}$$

above the heat flux gauge, the surrounding insulation (that forms the walls of the heat flux gauge cavity) will heat up. Following the procedure outlined here effectively eliminates the contributions of these hot surrounding materials.

This procedure is validated by tests in which heat transfer from the same propane wall flame is measured by a recessed gauge immediately after flame ignition. Unlike the flames supported by polymeric materials, which must first heat up and pyrolyze before producing gaseous volatiles, this propane flame can be easily turned on or off. In this manner, side walls of the heat flux gauge cavity are not preheated and thus, initially, they have no impact on measured results. In these tests, $q''_{recessed}$ is determined as the maximum value measured before $\frac{dq''}{dt}$ decreases below $1 \text{ kW m}^{-2} \text{ s}^{-1}$. In the two representative tests shown in Fig. A3, this yields: $q''_{recessed} = 12.94$ and 12.25 kW m^{-2} ; these measurements are consistent with values determined by the flame extinction method described above (12.74 and 13.43 kW m^{-2}) thus validating each approach to provide reliable measurements flame to surface heat flux when the gauge is recessed.

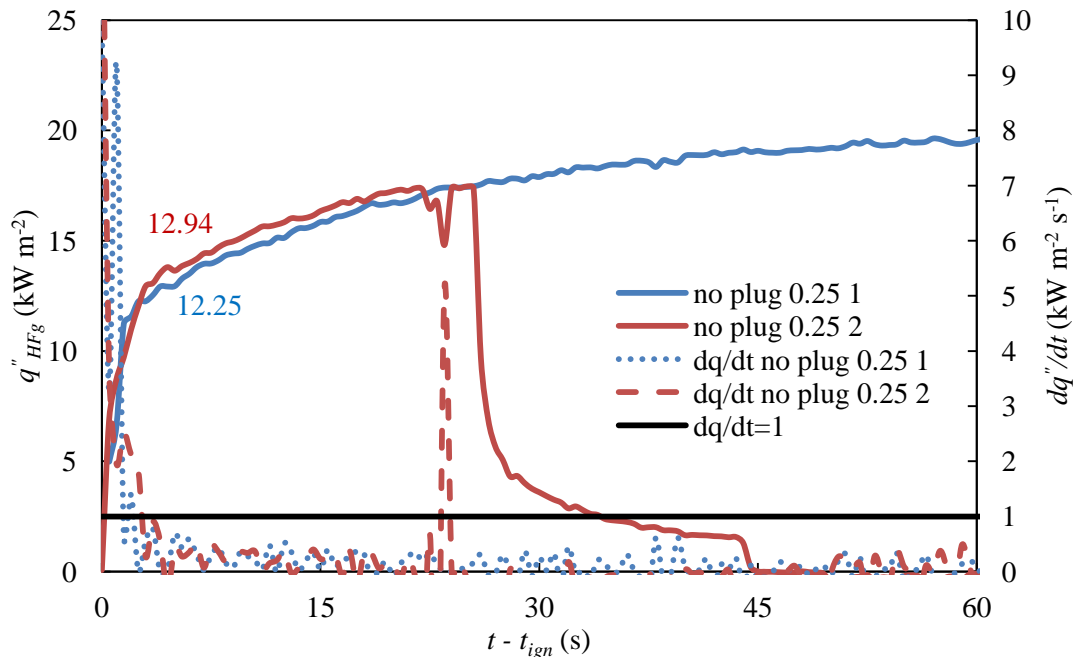
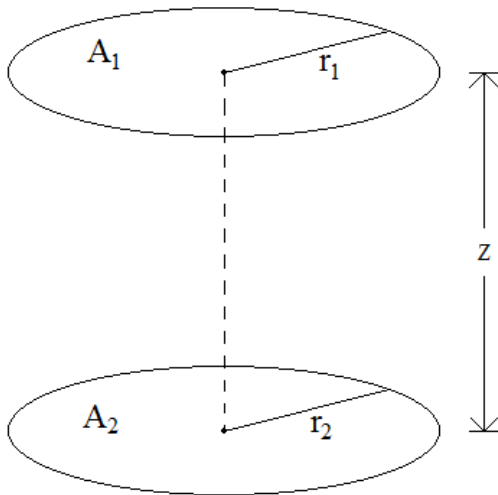


Figure A 3. Recessed gauge heat flux measurement of a propane flame taken at ignition.

A3. View Factor Calculations

Theoretical [50]



$$R_1 = \frac{r_1}{z} \quad R_2 = \frac{r_2}{z} \quad X = 1 + \frac{1+R_2^2}{R_1^2}$$

$$F_1 = \frac{1}{2} \left(X - \sqrt{X^2 - 4 \left(\frac{R_2}{R_1} \right)^2} \right)$$

$$R_1 = R_2 = R = \frac{3/16}{1/4} = \frac{3}{4}$$

$$X = 1 + \frac{1+R_2^2}{R_1^2} \rightarrow X = 1 + \frac{1+R^2}{R^2}$$

$$\frac{1 + \left(\frac{3}{4}\right)^2}{\left(\frac{3}{4}\right)^2} = \frac{34}{9}$$

$$F_{1 \rightarrow 2} = \frac{1}{2} \left(\frac{34}{9} - \sqrt{\left(\frac{34}{9}\right)^2 - 4 \left(\frac{R}{R}\right)^2} \right) = 0.286$$

Figure A 4. View factor schematic.

Here, A_1 and A_2 represent the surface area of the opening drilled through the sample/insulation and the front face of the heat flux gauge, respectively. Z is taken as the nominal distance that the heat flux gauge is recessed, 0.64 cm.

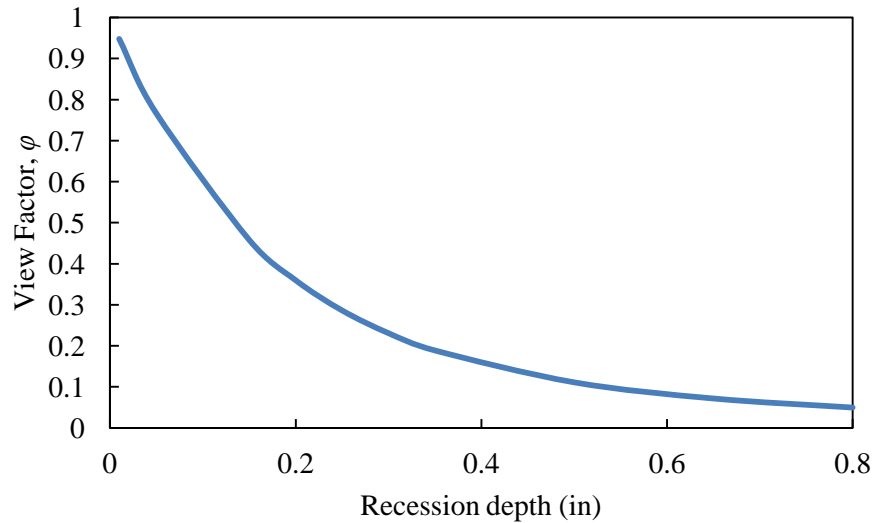


Figure A 5. Radiative view factor as a function of recession depth, assuming $r_1 = r_2 = 0.48$ cm.

Empirical

The radiative view factor, ϕ , of a recessed heat flux gauge was determined experimentally by comparing the heat flux it recorded while exposed to the radiant heater of a cone calorimeter when the gauge was flush with and recessed 0.64 cm into the surface of a sample. In these tests, the heat flux gauge was positioned in a sample prepared as per the procedure defined in Section 2.2 of this work, which was placed 2.5 cm below (normal to) the cone calorimeter's heater. Once in place, the sample and heat flux gauge were shielded by four 6.0 mm thick layers of Kaowool PM insulation and the cone heater was turned on. When the heater reached a steady temperature, the shielding insulation was removed. As seen in Fig. A 6, incident heat flux is determined from each of these tests as the peak measurement obtained before $\frac{dq''}{dt} < 1 \text{ kW m}^{-2} \text{ s}^{-1}$.

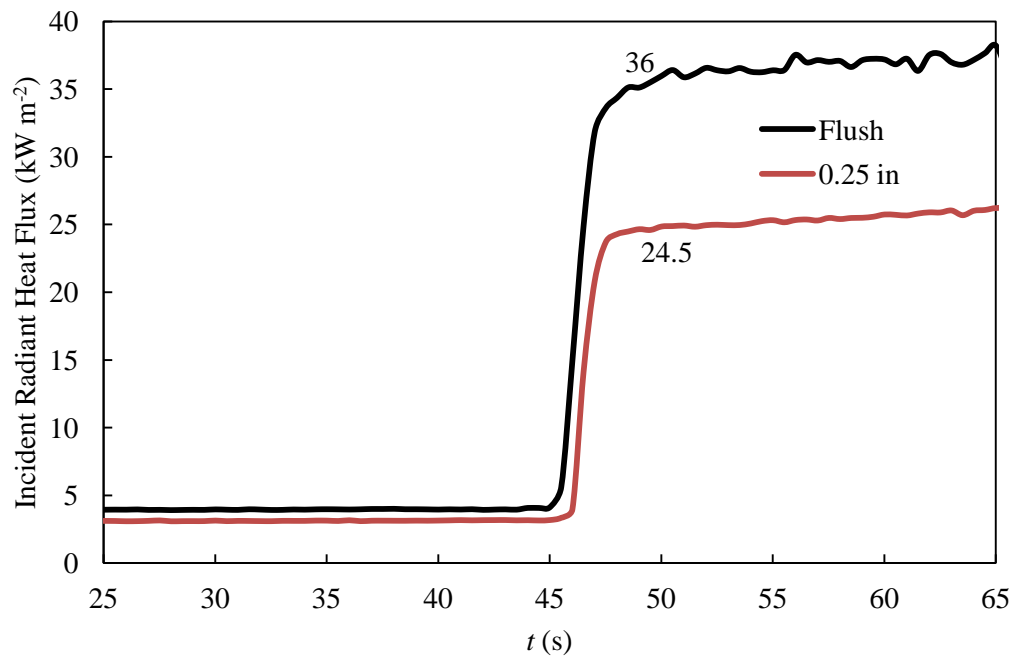


Figure A 6. Measured heat flux as a function of heat flux gauge recession depth (inches).

Using the measurements shown here, φ can be calculated as

$$\varphi = \frac{q_{recessed}''}{q_{flush}''} = \frac{24.5 \text{ kW m}^{-2}}{36 \text{ kW m}^{-2}} = 0.77 . \text{ An uncertainty of } \pm 0.05 \text{ is obtained by recognizing}$$

that, although shielded, the prepared sample/insulation assembly surrounding the heat flux gauge still heats up slightly before direct exposures. When the heat flux gauge is flush with the sample's face, this results in a $\sim 1.8 \text{ kW m}^{-2}$ difference in measured heat flux versus when the gauge is exposed to otherwise identical conditions but openly supported (not surrounded by a sample.) This serves as a fair approximation for the upper bound of uncertainty in this measurement and thus the radiative view factor is reported as: $\varphi = 0.77 \pm 0.05$

A4. Adiabatic Flame Temperature Calculations

A5.1 Propane

The adiabatic flame temperature of propane was calculated using the NASA Chemical Equilibrium with Applications Solver [67]

Input

```
prob case=c3h87616  hp p(atm)=1
phi=1
reac
  fuel  C3H8          wt%= 100.0 t,k= 298.15
  oxid  Air           wt%= 100.0 t,k=298.15
output short
output trace= 1e-5
end
```

Output:

NASA-GLENN CHEMICAL EQUILIBRIUM PROGRAM CEA2, FEBRUARY 5, 2004
BY BONNIE MCBRIDE AND SANFORD GORDON
REFS: NASA RP-1311, PART I, 1994 AND NASA RP-1311, PART II, 1996


```
prob case=c3h87616  hp p(atm)=1
phi=1
reac
  fuel  C3H8          wt%= 100.0 t,k= 298.15
  oxid  Air           wt%= 100.0 t,k=298.15
output short
output trace= 1e-5
end
```

THERMODYNAMIC EQUILIBRIUM COMBUSTION PROPERTIES AT ASSIGNED

PRESSURES

CASE = c3h87616

TEMP	REACTANT	WT FRACTION	ENERGY
		(SEE NOTE)	KJ/KG-MOL
K			
298.150	FUEL C3H8	1.0000000	-104680.000

OXIDANT Air 1.0000000 -125.530
298.150

O/F= 15.67890 %FUEL= 5.995600 R,EQ.RATIO= 1.000000 PHI,EQ.RATIO=
1.000000

THERMODYNAMIC PROPERTIES

P, BAR 1.0132

T, K 2264.87

RHO, KG/CU M 1.5156-1
H, KJ/KG -146.41
U, KJ/KG -814.95
G, KJ/KG -22025.2
S, KJ/(KG) (K) 9.6601

M, (1/n) 28.168
(dLV/dLP)t -1.00302
(dLV/dLT)p 1.0893
Cp, KJ/(KG) (K) 2.2632
GAMMAS 1.1789
SON VEL,M/SEC 887.8

MOLE FRACTIONS

*Ar 8.5612-3
*CO 1.2447-2
*CO2 1.0274-1
*H 4.5743-4
*H2 3.2648-3
H2O 1.4793-1
*NO 2.2995-3
*N2 7.1267-1
*O 3.0470-4
*OH 3.5395-3
*O2 5.7822-3

* THERMODYNAMIC PROPERTIES FITTED TO 20000.K

NOTE. WEIGHT FRACTION OF FUEL IN TOTAL FUELS AND OF OXIDANT IN TOTAL
OXIDANTS

A5.2 Polymeric Materials

The adiabatic flame temperature of each polymeric material studied in this work was calculated using the MATLAB script below assuming complete combustion of a stoichiometric mixture of the monomer in air to produce CO₂, H₂O, and N₂ (no minor species) using each material's heat of complete combustion, $H_{c\text{complete}}^{MATL}$, and temperature dependent heat capacities, c_p , as defined in the NIST Chemistry Webbook [70]. For water vapor between $298 \leq T \leq 500$ K, c_p is defined as per the NIST-JANAF Thermochemical Tables [114].

```
clf
clc
clear

%-----PMMA-----
T_fl_PMMA = 2,327K
% Hc=24500;    % heat of combustion, J/g Fuel
% MW=100;     % g / mol Fuel
% vF=1;       % # of moles of Fuel, by default this will probably = 1
% vco2=5;     % # of moles of CO2
% vh2o=4;     % # of moles of H2O
% vn2=22.56;  % # of moles of N2

%-----ABS-----T_fl_ABS
solves to be 2,405 K
% Hc=36500;   % heat of combustion, J/g Fuel
% MW=211;    % g / mol Fuel
% vF=1;      % # of moles of Fuel, by default this will probably = 1
% vco2=15;   % # of moles of CO2
% vh2o=8.5;  % # of moles of H2O
% vn2=72.88; % # of moles of N2

%-----FRP-----T_fl_FRP solves
to be 2,277K

Hc=22200;    % heat of combustion, J/g Fuel
MW=512;     % g / mol Fuel
vF=1;       % # of moles of Fuel, by default this will probably = 1
vco2=25;    % # of moles of CO2
vh2o=18;    % # of moles of H2O
vn2=107.16; % # of moles of N2
%Note: The composition of FRP chosen here (used to determine molecular
weight and stoichiometry when balancing this reaction) is based on the
report, "FULL PUBLIC REPORT M390B Unsaturated Polyester Resin File No:
NA/166" [115]. This was chosen over using each of the three main
species - phthalic anhydride, maleic anhydride, and styrene [88]-
```


because it provides a more consistent H_c (as calculated by O_2 consumption) in comparison to our measured H_c .

```
%-----HIPS-----  
T_fl_POM solves to be 2457K  
% Hc=39200;      % heat of combustion, J/g Fuel  
% MW=104;        % g / mol Fuel  
% vF=1;          % # of moles of Fuel, by default this will probably = 1  
% vco2=8;        % # of moles of CO2  
% vh2o=4;        % # of moles of H2O  
% vn2=37.6;      % # of moles of N2
```

```
%-----PBT-----  
T_fl_POM solves to be 2286K  
% Hc=23100;      % heat of combustion, J/g Fuel  
% MW=220;        % g / mol Fuel  
% vF=1;          % # of moles of Fuel, by default this will probably = 1  
% vco2=12;       % # of moles of CO2  
% vh2o=6;        % # of moles of H2O  
% vn2=48.88;     % # of moles of N2
```

```
%-----POM-----  
T_fl_POM solves to be 2407K  
% Hc=15900;      % heat of combustion, J/g Fuel  
% MW=30;         % g / mol Fuel  
% vF=1;          % # of moles of Fuel, by default this will probably = 1  
% vco2=1;        % # of moles of CO2  
% vh2o=1;        % # of moles of H2O  
% vn2=3.76;      % # of moles of N2
```

```
%-----PP-----T_fl_PP solves to  
be 2294K  
% Hc=41000;      % heat of combustion, J/g Fuel  
% MW=42;         % g / mol Fuel  
% vF=1;          % # of moles of Fuel, by default this will probably = 1  
% vco2=3;        % # of moles of CO2  
% vh2o=3;        % # of moles of H2O  
% vn2=16.92;     % # of moles of N2
```

```
syms t  
T_fl=2300;        %Initial guess for flame temperature [ K]  
T_fl_old= 2100;  %Old Guess for Flame temperature [K]  
%Energy needed to raise product species up to 1200K  
%%-----CO2-----  
%CO2; 298K - 1200K
```

```

E_co2_1= double(vco2*int(24.99735 + 55.18696*(t/1000) -
33.69137*(t/1000)^2 + 7.948387*(t/1000)^3 -
0.136638/(t/1000)^2,t,298,1200)); %checked NIST Webbook

%Nitrogen; 298K - 500 K
E_n2_1= double(vn2*int(28.98641 + 1.853978*(t/1000) -
9.647459*(t/1000)^2 + 16.63537*(t/1000)^3 +
0.000117/(t/1000)^2,t,298,500)); %checked NIST Webbook

%Nitrogen; 500K - 1200 K
E_n2_2= double(vn2*int(19.50583 + 19.88705*(t/1000) -
8.598535*(t/1000)^2 + 1.369784*(t/1000)^3 +
0.527601/(t/1000)^2,t,500,1200)); %checked NIST Webbook

%H2O; 298 - 500 K
E_h2o_1 = double(vh2o*int(( 1.502E-05*t^2 - 3.874E-03*t +
3.341E+01),t,298,500)); %Excel Fit of JANAF Tables
http://kinetics.nist.gov/janaf/html/H-064.html
%H2O; 500 - 1200 K
E_h2o_2= double(vh2o*int(30.092 + 6.832514*(t/1000) +
6.793435*(t/1000)^2 - 2.534480*(t/1000)^3 +
0.082139/(t/1000)^2,t,500,1200)); %checked NIST Webbook

E_1200=E_co2_1 + (E_n2_1 + E_n2_2) + (E_h2o_1 + E_h2o_2);

if vF*MW*Hc > E_1200
    disp('T_fl is greater than 1,200K')

% Determine Flame Temp, if it's above
resid=vF*MW*Hc - E_1200;
iter=1;
while abs(resid) > (1e-7)*Hc*vF*MW && iter < 100
    T_flame(iter)=T_fl;

    if T_fl < 1700
        E_co2_2 = double(vco2*int(58.16639 + 2.720074*(t/1000) -
0.492289*(t/1000)^2 + 0.038844*(t/1000)^3 -
6.447293/(t/1000)^2,t,1200,T_fl)); %checked NIST Webbook
        E_h2o_3 = double(vh2o*int(30.092 + 6.832514*(t/1000) +
6.793435*(t/1000)^2 - 2.534480*(t/1000)^3 +
0.082139/(t/1000)^2,t,1200,T_fl)); %checked NIST Webbook
        E_n2_3 = double(vn2*int(19.50583 + 19.88705*(t/1000) -
8.598535*(t/1000)^2 + 1.369784*(t/1000)^3 +
0.527601/(t/1000)^2,t,1200,T_fl)); %checked NIST Webbook

        resid = Hc*vF*MW - (E_1200 + (E_co2_2) + (E_h2o_3)
+(E_n2_3));

```

```

elseif T_fl >= 1700 && T_fl < 2000
    E_co2_2 = double(vco2*int(58.16639 + 2.720074*(t/1000) -
0.492289*(t/1000)^2 + 0.038844*(t/1000)^3 -
6.447293/(t/1000)^2,t,1200,1700)); %checked NIST Webbook
    E_h2o_3 = double(vh2o*int(30.092 + 6.832514*(t/1000) +
6.793435*(t/1000)^2 - 2.534480*(t/1000)^3 +
0.082139/(t/1000)^2,t,1200,1700)); %checked NIST Webbook
    E_n2_3 = double(vn2*int(19.50583 + 19.88705*(t/1000) -
8.598535*(t/1000)^2 + 1.369784*(t/1000)^3 +
0.527601/(t/1000)^2,t,1200,1700)); %checked NIST Webbook

    E_co2_3 = double(vco2*int(58.16639 + 2.720074*(t/1000) -
0.492289*(t/1000)^2 + 0.038844*(t/1000)^3 -
6.447293/(t/1000)^2,t,1700,T_fl)); %checked NIST Webbook
    E_h2o_4 = double(vh2o*int(41.96426 + 8.622053*(t/1000) -
1.499780*(t/1000)^2 + 0.098119*(t/1000)^3 -
11.15764/(t/1000)^2,t,1700,T_fl)); %checked NIST Webbook
    E_n2_4 = double(vn2*int(19.50583 + 19.88705*(t/1000) -
8.598535*(t/1000)^2 + 1.369784*(t/1000)^3 +
0.527601/(t/1000)^2,t,1700,T_fl)); %checked NIST Webbook

    resid = Hc*vF*MW - (E_1200 + (E_co2_2 + E_co2_3) + (E_h2o_3 +
E_h2o_4) + (E_n2_3 + E_n2_4));

elseif T_fl >= 2000
    E_co2_2 = double(vco2*int(58.16639 + 2.720074*(t/1000) -
0.492289*(t/1000)^2 + 0.038844*(t/1000)^3 -
6.447293/(t/1000)^2,t,1200,1700)); %checked NIST Webbook
    E_h2o_3 = double(vh2o*int(30.092 + 6.832514*(t/1000) +
6.793435*(t/1000)^2 - 2.534480*(t/1000)^3 +
0.082139/(t/1000)^2,t,1200,1700)); %checked NIST Webbook
    E_n2_3 = double(vn2*int(19.50583 + 19.88705*(t/1000) -
8.598535*(t/1000)^2 + 1.369784*(t/1000)^3 +
0.527601/(t/1000)^2,t,1200,1700)); %checked NIST Webbook

    E_co2_3 = double(vco2*int(58.16639 + 2.720074*(t/1000) -
0.492289*(t/1000)^2 + 0.038844*(t/1000)^3 -
6.447293/(t/1000)^2,t,1700,2000)); %checked NIST Webbook
    E_h2o_4 = double(vh2o*int(41.96426 + 8.622053*(t/1000) -
1.499780*(t/1000)^2 + 0.098119*(t/1000)^3 -
11.15764/(t/1000)^2,t,1700,2000)); %checked NIST Webbook
    E_n2_4 = double(vn2*int(19.50583 + 19.88705*(t/1000) -
8.598535*(t/1000)^2 + 1.369784*(t/1000)^3 +
0.527601/(t/1000)^2,t,1700,2000)); %checked NIST Webbook

    E_co2_4 = double(vco2*int(58.16639 + 2.720074*(t/1000) -
0.492289*(t/1000)^2 + 0.038844*(t/1000)^3 -
6.447293/(t/1000)^2,t,2000,T_fl)); %checked NIST Webbook
    E_h2o_5 = double(vh2o*int(41.96426 + 8.622053*(t/1000) -
1.499780*(t/1000)^2 + 0.098119*(t/1000)^3 -
11.15764/(t/1000)^2,t,2000,T_fl)); %checked NIST Webbook
    E_n2_5 = double(vn2*int(35.51872 + 1.128728*(t/1000) -
0.196103*(t/1000)^2 + 0.014662*(t/1000)^3 -
4.553760/(t/1000)^2,t,2000,T_fl)); %checked NIST Webbook

```

```
        resid = Hc*vF*MW - (E_1200 + (E_co2_2 + E_co2_3 + E_co2_4) +  
(E_h2o_3 + E_h2o_4 + E_h2o_5) +(E_n2_3 + E_n2_4 + E_n2_5));  
    end
```

```
    del_T = T_fl-T_fl_old;  
    T_fl_old = T_fl;
```

```
    if resid > 0  
        T_fl=T_fl + (0.9)*abs(del_T);  
    elseif resid < 0  
        T_fl=T_fl - (0.9)*abs(del_T);  
    end
```

```
    iter = iter +1;
```

```
end  
iter  
resid  
T_fl  
plot(T_flame)
```

```
elseif vF*MW*Hc < E_1200  
    disp('Are you sure this is a flame? It looks like you need to do a  
hand calc or edit this script to look for T_fl < 1,200 K')  
end
```

A6. ThermaKin2D Input Files

A6.1 Components (.cmp)

COMPONENT: KAOWOOL
STATE: S
DENSITY: 256 0 0 0
HEAT CAPACITY: 1070 0 0 0
CONDUCTIVITY: 0.0519 -4e-5 1e-7 2
TRANSPORT: 1e-30 0 0 0
EMISSIVITY & ABSORPTION: 0 10000

COMPONENT: PMMA
STATE: S
DENSITY: 1155 0 0 0
HEAT CAPACITY: 601.4 3.63 0 0
CONDUCTIVITY: 0.45 -3.8e-4 0 0
TRANSPORT: 2e-5 0 0 0
EMISSIVITY & ABSORPTION: 0.95 1.94

COMPONENT: PMMA_black
STATE: S
DENSITY: 1155 0 0 0
HEAT CAPACITY: 601.4 3.63 0 0
CONDUCTIVITY: 0.45 -3.8e-4 0 0
TRANSPORT: 2e-5 0 0 0
EMISSIVITY & ABSORPTION: 0.95 10000

COMPONENT: PMMA_glass
STATE: S
DENSITY: 1155 0 0 0
HEAT CAPACITY: 601.4 3.63 0 0
CONDUCTIVITY: 0.27 -2.4e-4 0 0
TRANSPORT: 2e-5 0 0 0
EMISSIVITY & ABSORPTION: 0.95 1.94

COMPONENT: PMMA_glass_black
STATE: S
DENSITY: 1155 0 0 0
HEAT CAPACITY: 601.4 3.63 0 0
CONDUCTIVITY: 0.27 -2.4e-4 0 0
TRANSPORT: 2e-5 0 0 0
EMISSIVITY & ABSORPTION: 0.95 10000

COMPONENT: PMMA_ch
STATE: S
DENSITY: 1155 0 0 0
HEAT CAPACITY: 601.4 3.63 0 0
CONDUCTIVITY: 0.27 -2.4e-4 0 0
TRANSPORT: 2e-5 0 0 0
EMISSIVITY & ABSORPTION: 0.95 1.94

COMPONENT: PMMA_g
STATE: G
DENSITY: 1155 0 0 0
HEAT CAPACITY: 1800 0 0 0
CONDUCTIVITY: 0.27 -2.4e-4 0 0
TRANSPORT: 2e-5 0 0 0
EMISSIVITY & ABSORPTION: 0.95 1.94

MIXTURES
S SWELLING: 0
L SWELLING: 0
G SWELLING LIMIT: 1e-30
PARALL CONDUCTIVITY: 0.5

PARALL TRANSPORT: 0.5

REACTION: PMMA + NOCOMP -> PMMA_glass + NOCOMP
STOICHIOMETRY: 1 0 1 0
ARRHENIUS: 1 0
HEAT: 0 0 0 0
TEMP LIMIT: L 378

REACTION: PMMA_black + NOCOMP -> PMMA_glass_black + NOCOMP
STOICHIOMETRY: 1 0 1 0
ARRHENIUS: 1 0
HEAT: 0 0 0 0
TEMP LIMIT: L 378

REACTION: PMMA_glass + NOCOMP -> PMMA_ch + PMMA_g
STOICHIOMETRY: 1 0 0.015 0.985
ARRHENIUS: 8.6e12 188100
HEAT: -846000 0 0 0
TEMP LIMIT: L 300

REACTION: PMMA_glass_black + NOCOMP -> PMMA_ch + PMMA_g
STOICHIOMETRY: 1 0 0.015 0.985
ARRHENIUS: 8.6e12 188100
HEAT: -846000 0 0 0
TEMP LIMIT: L 300

A6.2 Conditions (.cnd); 17.5 cm Tall Sample

OBJECT TYPE: 2D

OBJECT STRUCTURE

FROM BOTTOM:
LAYER LENGTH: 0.04
FROM FRONT:
THICKNESS: 0.0059
TEMPERATURE: 300
MASS FRACTIONS:
PMMA 1

THICKNESS: 0.006
TEMPERATURE: 300
MASS FRACTIONS:
KAOWOOL 1

LAYER LENGTH: 0.135
FROM FRONT:
THICKNESS: 0.0059
TEMPERATURE: 300
MASS FRACTIONS:
PMMA_black 1

THICKNESS: 0.006
TEMPERATURE: 300
MASS FRACTIONS:
KAOWOOL 1

Remove this section to define a
4 cm tall material object

OBJECT BOUNDARIES

FRONT BOUNDARY

MASS TRANSPORT: YES
 PMMA_g LIN 0.05 0
 PMMA_glass_black EXP 5500 80404 } J_{flow} , eqn. 26

EXTERNAL HEAT FLUX 1: YES
 START & END TIMES: 0 122
 RAMP: HOLD
 MODE: CONV
 CONVECTION COEFF: 25
 POSITION DEPEND1: 1974 -87750 0.008
 POSITION DEPEND2: 1413 -17667 0.0203
 POSITION DEPEND3: 5068 -200400 0.0253

EXTERNAL HEAT FLUX 2: YES
 START & END TIMES: 122 302
 RAMP: UP
 MODE: RAD
 POSITION DEPEND1: -3000 0 0.05
 POSITION DEPEND2: 0 0 0.10
 POSITION DEPEND3: 0 0 0.5

EXTERNAL HEAT FLUX 3: YES
 START & END TIMES: 302 600
 RAMP: HOLD
 MODE: RAD
 POSITION DEPEND1: -3000 0 0.05
 POSITION DEPEND2: 0 0 0.10
 POSITION DEPEND3: 0 0 0.5

Account for 'blowing effect', see Section 3.3.1. These heat flux terms are defined to reduce incident heat flux to the material object in accordance with the experimentally measured reduction in q''_{HFg} at $y < 5$ cm. External Heat Flux 2 (EHF 2) removes an increasing amount of heat (linear increase from 0 to 3 kW m⁻²) from ignition until $t - t_{ign} = 180$ s. EHF 3 removes 3 kW m⁻² from the surface of the sample when $t - t_{ign} > 180$ s

FLAME: YES
 IGNITION MASS FLUXES:
 PMMA_g 1e-5
 FLAME LENGTH: -0.1192 0.0696 0.2751
 HEAT FLUX MODE: CONV
 CONVECTION COEFF: 19.3
 HEAT FLUX INSIDE: 2072 0.05 1762
 HEAT FLUX BELOW: 1e2
 HEAT FLUX ABOVE: 1.54 0.432 0.022

BACKGROUND TEMP: 291
 RADIAT ABSORPT MODE: RAND

BACK BOUNDARY

MASS TRANSPORT: NO
 EXTERNAL HEAT FLUX 1: NO
 EXTERNAL HEAT FLUX 2: NO
 EXTERNAL HEAT FLUX 3: NO
 FLAME: NO

BACKGROUND TEMP: 291
RADIAT ABSORPT MODE: RAND

INTEGRATION PARAMETERS

LAYER SIZE: 0.001
ELEMENT SIZE: 5e-5
TIME STEP: 0.005
DURATION: 600

OUTPUT FREQUENCY:
LAYERS: 5
ELEMENTS: 20
TIME STEPS: 200

A7. FDS Input Files (Fine Grid)

Note: for brevity, DEVC ID and SLCF lines of this code are not included. The user is able to define measurement devices and slice files given knowledge of presented outputs presented in Section 5; their inclusion here (which would require several pages) will not affect simulation results.

```
&HEAD CHID='PMMA_DNS_preheat_1e-4mm', TITLE='2D DNS run, 80s preheated
temperatures, grid cells between 0.1-0.4mm, 7 meshes, external flux for
14.5 seconds' /

&MESH IJK=150,1,800, XB=0.00,0.015,0.0,0.01,-0.015,0.065 / flame,
0.1mm, 120,000 cells
&MESH IJK=75,1,400, XB=0.015,0.03,0.0,0.01,-0.015,0.065 / near flame
entrainment, 0.2mm, 30,000 cells
&MESH IJK=300,1,75, XB=0.00,0.06,0.0,0.01,0.065,0.08 / upper flame,
0.2mm, 22,500 cells
&MESH IJK=300,1,75, XB=0.00,0.06,0.0,0.01,-0.03,-0.015 / lower
entrainment, 0.2mm, 22,500 cells
&MESH IJK=150,1,50, XB=0.00,0.06,0.0,0.01,0.08,0.10 / top flame, 0.4mm,
7,500 cells
&MESH IJK=75,1,200, XB=0.03,0.06,0.0,0.01,-0.015,0.065 / outer
entrainment, 0.4mm, 15,000 cells
&MESH IJK=150,1,75, XB=0.00,0.06,0.0,0.01,-0.06,-0.03 / bottom
entrainment, 0.4mm, 11,250 cells

&TIME T_END=60. /

&MISC TMPA=18., DNS=.TRUE., SECOND_ORDER_INTERPOLATED_BOUNDARY=.TRUE. /

&DUMP DT_DEVC=0.25, DT_RESTART=1. /

&REAC SOOT_YIELD=0.0, FUEL='MMA', HEAT_OF_COMBUSTION=25000.,
FUEL_RADCAL_ID='MMA' /

&SPEC ID = 'MMA'
FORMULA = 'C5H8O2'
RAMP_K = 'k_MMA'
RAMP_MU = 'mu_MMA'
RAMP_D = 'D_MMA'
SPECIFIC_HEAT = 0.80
RAMP_CP = 'cp_MMA' /

&RAMP ID='k_MMA', T=100., F=0.0150 /
&RAMP ID='k_MMA', T=410., F=0.0386 /
&RAMP ID='k_MMA', T=727., F=0.0663 /

&RAMP ID='mu_MMA', T=100., F=9.44E-6 /
&RAMP ID='mu_MMA', T=410., F=1.74E-5 /
&RAMP ID='mu_MMA', T=727., F=2.45E-5 /

&RAMP ID='D_MMA', T=15., F=7.64E-6 /
&RAMP ID='D_MMA', T=220., F=1.96E-5 /
&RAMP ID='D_MMA', T=420., F=3.55E-5 /
&RAMP ID='D_MMA', T=620., F=5.54E-5 /
&RAMP ID='D_MMA', T=820., F=7.89E-5 /
&RAMP ID='D_MMA', T=1020., F=1.06E-4 /
&RAMP ID='D_MMA', T=1227., F=1.37E-4 /

&RAMP ID='cp_MMA', T=15., F=0.753 /
&RAMP ID='cp_MMA', T=220., F=1.28 /
&RAMP ID='cp_MMA', T=420., F=1.68 /
&RAMP ID='cp_MMA', T=620., F=1.98 /
```

```

&RAMP ID='cp_MMA', T=727., F=2.09 /

&MATL ID = 'PMMA'
  ABSORPTION_COEFFICIENT = 2240.
  EMISSIVITY = 0.95
  SPECIFIC_HEAT_RAMP = 'c_PMMA'
  CONDUCTIVITY_RAMP = 'k_PMMA'
  DENSITY = 1155.
  N_REACTIONS = 1
  A(1) = 8.6E12
  E(1) = 1.881E5
  SPEC_ID = 'MMA'
  NU_SPEC = 0.985
  MATL_ID = 'PMMA char'
  NU_MATL = 0.015
  HEAT_OF_REACTION = 846. /

&MATL ID='PMMA char'
  ABSORPTION_COEFFICIENT = 2240.
  EMISSIVITY = 0.95
  DENSITY = 1155
  CONDUCTIVITY_RAMP = 'k_PMMA'
  SPECIFIC_HEAT_RAMP = 'c_PMMA' /

&RAMP ID='k_PMMA', T=15., F=0.3406 /
&RAMP ID='k_PMMA', T=105., F=0.3064 /
&RAMP ID='k_PMMA', T=106., F=0.1790 /
&RAMP ID='k_PMMA', T=600., F=0.0605 /

&RAMP ID='c_PMMA', T=15., F=1.637 /
&RAMP ID='c_PMMA', T=600., F=3.743 /

&MATL ID = 'KAOWOOL'
  SPECIFIC_HEAT = 1.070
  CONDUCTIVITY_RAMP = 'k_Kaowool'
  DENSITY = 256. /

&RAMP ID='k_Kaowool', T=20., F=0.0487 /
&RAMP ID='k_Kaowool', T=40., F=0.0492 /
&RAMP ID='k_Kaowool', T=60., F=0.0497 /
&RAMP ID='k_Kaowool', T=80., F=0.0502 /
&RAMP ID='k_Kaowool', T=100., F=0.0509 /
&RAMP ID='k_Kaowool', T=120., F=0.0516 /
&RAMP ID='k_Kaowool', T=140., F=0.0524 /
&RAMP ID='k_Kaowool', T=160., F=0.0533 /
&RAMP ID='k_Kaowool', T=180., F=0.0543 /
&RAMP ID='k_Kaowool', T=200., F=0.0553 /
&RAMP ID='k_Kaowool', T=220., F=0.0565 /
&RAMP ID='k_Kaowool', T=240., F=0.0577 /
&RAMP ID='k_Kaowool', T=260., F=0.0590 /
&RAMP ID='k_Kaowool', T=280., F=0.0604 /
&RAMP ID='k_Kaowool', T=300., F=0.0618 /
&RAMP ID='k_Kaowool', T=320., F=0.0633 /
&RAMP ID='k_Kaowool', T=340., F=0.0650 /
&RAMP ID='k_Kaowool', T=360., F=0.0666 /
&RAMP ID='k_Kaowool', T=380., F=0.0684 /
&RAMP ID='k_Kaowool', T=400., F=0.0703 /
&RAMP ID='k_Kaowool', T=538., F=0.0852 /
&RAMP ID='k_Kaowool', T=816., F=0.1269 /
&RAMP ID='k_Kaowool', T=1093., F=0.1839 /

&MATL ID = 'STEEL'
  FYI = 'SFPE Handbook'

```

```

SPECIFIC_HEAT      = 0.473
CONDUCTIVITY       = 43.
DENSITY            = 7801. /

&SURF ID           = 'UPPER'
COLOR              = 'SKY BLUE 3'
MATL_ID            = 'PMMA', 'KAOWOOL'
THICKNESS          = 0.0059, 0.006
BACKING            = 'EXPOSED'
CELL_SIZE_FACTOR  = 0.1 /

&SURF ID           = 'INSULATION'
COLOR              = 'TAN'
MATL_ID            = 'KAOWOOL'
THICKNESS          = 0.0119 /

&SURF ID           = 'HOLDER'
COLOR              = 'GRAY 30'
MATL_ID            = 'STEEL', 'KAOWOOL'
THICKNESS          = 0.0016, 0.006 /

&SURF ID='LAYER1', COLOR='SKY BLUE 3', MATL_ID='PMMA', 'KAOWOOL',
THICKNESS=0.0059, 0.006, CELL_SIZE_FACTOR=0.1, TMP_INNER=198.3, 52.2,
BACKING='EXPOSED', EXTERNAL_FLUX=49.13, RAMP_EF='HEATER' /
&SURF ID='LAYER2', COLOR='SKY BLUE 3', MATL_ID='PMMA', 'KAOWOOL',
THICKNESS=0.0059, 0.006, CELL_SIZE_FACTOR=0.1, TMP_INNER=198.3, 52.2,
BACKING='EXPOSED', EXTERNAL_FLUX=48.69, RAMP_EF='HEATER' /
&SURF ID='LAYER3', COLOR='SKY BLUE 3', MATL_ID='PMMA', 'KAOWOOL',
THICKNESS=0.0059, 0.006, CELL_SIZE_FACTOR=0.1, TMP_INNER=198.3, 52.2,
BACKING='EXPOSED', EXTERNAL_FLUX=48.25, RAMP_EF='HEATER' /
&SURF ID='LAYER4', COLOR='SKY BLUE 3', MATL_ID='PMMA', 'KAOWOOL',
THICKNESS=0.0059, 0.006, CELL_SIZE_FACTOR=0.1, TMP_INNER=198.3, 52.2,
BACKING='EXPOSED', EXTERNAL_FLUX=47.82, RAMP_EF='HEATER' /
&SURF ID='LAYER5', COLOR='SKY BLUE 3', MATL_ID='PMMA', 'KAOWOOL',
THICKNESS=0.0059, 0.006, CELL_SIZE_FACTOR=0.1, TMP_INNER=198.3, 52.2,
BACKING='EXPOSED', EXTERNAL_FLUX=47.38, RAMP_EF='HEATER' /
&SURF ID='LAYER6', COLOR='SKY BLUE 3', MATL_ID='PMMA', 'KAOWOOL',
THICKNESS=0.0059, 0.006, CELL_SIZE_FACTOR=0.1, TMP_INNER=198.3, 52.2,
BACKING='EXPOSED', EXTERNAL_FLUX=46.94, RAMP_EF='HEATER' /
&SURF ID='LAYER7', COLOR='SKY BLUE 3', MATL_ID='PMMA', 'KAOWOOL',
THICKNESS=0.0059, 0.006, CELL_SIZE_FACTOR=0.1, TMP_INNER=198.3, 52.2,
BACKING='EXPOSED', EXTERNAL_FLUX=46.5, RAMP_EF='HEATER' /
&SURF ID='LAYER8', COLOR='SKY BLUE 3', MATL_ID='PMMA', 'KAOWOOL',
THICKNESS=0.0059, 0.006, CELL_SIZE_FACTOR=0.1, TMP_INNER=198.3, 52.2,
BACKING='EXPOSED', EXTERNAL_FLUX=46.06, RAMP_EF='HEATER' /
&SURF ID='LAYER9', COLOR='SKY BLUE 3', MATL_ID='PMMA', 'KAOWOOL',
THICKNESS=0.0059, 0.006, CELL_SIZE_FACTOR=0.1, TMP_INNER=198.3, 52.2,
BACKING='EXPOSED', EXTERNAL_FLUX=45.62, RAMP_EF='HEATER' /
&SURF ID='LAYER10', COLOR='SKY BLUE 3', MATL_ID='PMMA', 'KAOWOOL',
THICKNESS=0.0059, 0.006, CELL_SIZE_FACTOR=0.1, TMP_INNER=198.3, 52.2,
BACKING='EXPOSED', EXTERNAL_FLUX=45.18, RAMP_EF='HEATER' /
&SURF ID='LAYER11', COLOR='SKY BLUE 3', MATL_ID='PMMA', 'KAOWOOL',
THICKNESS=0.0059, 0.006, CELL_SIZE_FACTOR=0.1, TMP_INNER=198.3, 52.2,
BACKING='EXPOSED', EXTERNAL_FLUX=44.74, RAMP_EF='HEATER' /
&SURF ID='LAYER12', COLOR='SKY BLUE 3', MATL_ID='PMMA', 'KAOWOOL',
THICKNESS=0.0059, 0.006, CELL_SIZE_FACTOR=0.1, TMP_INNER=198.3, 52.2,
BACKING='EXPOSED', EXTERNAL_FLUX=44.31, RAMP_EF='HEATER' /
&SURF ID='LAYER13', COLOR='SKY BLUE 3', MATL_ID='PMMA', 'KAOWOOL',
THICKNESS=0.0059, 0.006, CELL_SIZE_FACTOR=0.1, TMP_INNER=198.3, 52.2,
BACKING='EXPOSED', EXTERNAL_FLUX=43.87, RAMP_EF='HEATER' /
&SURF ID='LAYER14', COLOR='SKY BLUE 3', MATL_ID='PMMA', 'KAOWOOL',
THICKNESS=0.0059, 0.006, CELL_SIZE_FACTOR=0.1, TMP_INNER=198.3, 52.2,
BACKING='EXPOSED', EXTERNAL_FLUX=43.43, RAMP_EF='HEATER' /

```



```

&SURF ID='LAYER120', COLOR='SKY BLUE 3', MATL_ID='PMMA','KAOWOOL',
THICKNESS=0.0059,0.006, CELL_SIZE_FACTOR=0.1, TMP_INNER=118,42.3,
BACKING='EXPOSED', EXTERNAL_FLUX=6.96, RAMP_EF='HEATER' /
&SURF ID='LAYER121', COLOR='SKY BLUE 3', MATL_ID='PMMA','KAOWOOL',
THICKNESS=0.0059,0.006, CELL_SIZE_FACTOR=0.1, TMP_INNER=118,42.3,
BACKING='EXPOSED', EXTERNAL_FLUX=5.96, RAMP_EF='HEATER' /
&SURF ID='LAYER122', COLOR='SKY BLUE 3', MATL_ID='PMMA','KAOWOOL',
THICKNESS=0.0059,0.006, CELL_SIZE_FACTOR=0.1, TMP_INNER=118,42.3,
BACKING='EXPOSED', EXTERNAL_FLUX=4.96, RAMP_EF='HEATER' /
&SURF ID='LAYER123', COLOR='SKY BLUE 3', MATL_ID='PMMA','KAOWOOL',
THICKNESS=0.0059,0.006, CELL_SIZE_FACTOR=0.1, TMP_INNER=118,42.3,
BACKING='EXPOSED', EXTERNAL_FLUX=3.96, RAMP_EF='HEATER' /
&SURF ID='LAYER124', COLOR='SKY BLUE 3', MATL_ID='PMMA','KAOWOOL',
THICKNESS=0.0059,0.006, CELL_SIZE_FACTOR=0.1, TMP_INNER=118,42.3,
BACKING='EXPOSED', EXTERNAL_FLUX=2.95, RAMP_EF='HEATER' /
&SURF ID='LAYER125', COLOR='SKY BLUE 3', MATL_ID='PMMA','KAOWOOL',
THICKNESS=0.0059,0.006, CELL_SIZE_FACTOR=0.1, TMP_INNER=118,42.3,
BACKING='EXPOSED', EXTERNAL_FLUX=2.45, RAMP_EF='HEATER' /
&SURF ID='LAYER126', COLOR='SKY BLUE 3', MATL_ID='PMMA','KAOWOOL',
THICKNESS=0.0059,0.006, CELL_SIZE_FACTOR=0.1, TMP_INNER=46.4,32.6,
BACKING='EXPOSED' /
&SURF ID='LAYER127', COLOR='SKY BLUE 3', MATL_ID='PMMA','KAOWOOL',
THICKNESS=0.0059,0.006, CELL_SIZE_FACTOR=0.1, TMP_INNER=22.,20.,
BACKING='EXPOSED' /

```

```

&RAMP ID='HEATER', T=0.0, F=1.0 /
&RAMP ID='HEATER', T=14.5, F=1.0 /
&RAMP ID='HEATER', T=15.0, F=0.0 /

```

```

&VENT XB=0.0,0.0,0.00,0.01,0.0002, SURF_ID='LAYER1' /
&VENT XB=0.0,0.0,0.00,0.01,0.0002,0.0004, SURF_ID='LAYER2' /
&VENT XB=0.0,0.0,0.00,0.01,0.0004,0.0006, SURF_ID='LAYER3' /
&VENT XB=0.0,0.0,0.00,0.01,0.0006,0.0008, SURF_ID='LAYER4' /
&VENT XB=0.0,0.0,0.00,0.01,0.0008,0.001, SURF_ID='LAYER5' /
&VENT XB=0.0,0.0,0.00,0.01,0.001,0.0012, SURF_ID='LAYER6' /
&VENT XB=0.0,0.0,0.00,0.01,0.0012,0.0014, SURF_ID='LAYER7' /
&VENT XB=0.0,0.0,0.00,0.01,0.0014,0.0016, SURF_ID='LAYER8' /
&VENT XB=0.0,0.0,0.00,0.01,0.0016,0.0018, SURF_ID='LAYER9' /
&VENT XB=0.0,0.0,0.00,0.01,0.0018,0.002, SURF_ID='LAYER10' /
&VENT XB=0.0,0.0,0.00,0.01,0.002,0.0022, SURF_ID='LAYER11' /
&VENT XB=0.0,0.0,0.00,0.01,0.0022,0.0024, SURF_ID='LAYER12' /
&VENT XB=0.0,0.0,0.00,0.01,0.0024,0.0026, SURF_ID='LAYER13' /
&VENT XB=0.0,0.0,0.00,0.01,0.0026,0.0028, SURF_ID='LAYER14' /
&VENT XB=0.0,0.0,0.00,0.01,0.0028,0.003, SURF_ID='LAYER15' /
&VENT XB=0.0,0.0,0.00,0.01,0.003,0.0032, SURF_ID='LAYER16' /
&VENT XB=0.0,0.0,0.00,0.01,0.0032,0.0034, SURF_ID='LAYER17' /
&VENT XB=0.0,0.0,0.00,0.01,0.0034,0.0036, SURF_ID='LAYER18' /
&VENT XB=0.0,0.0,0.00,0.01,0.0036,0.0038, SURF_ID='LAYER19' /
&VENT XB=0.0,0.0,0.00,0.01,0.0038,0.004, SURF_ID='LAYER20' /
&VENT XB=0.0,0.0,0.00,0.01,0.004,0.0042, SURF_ID='LAYER21' /
&VENT XB=0.0,0.0,0.00,0.01,0.0042,0.0044, SURF_ID='LAYER22' /
&VENT XB=0.0,0.0,0.00,0.01,0.0044,0.0046, SURF_ID='LAYER23' /
&VENT XB=0.0,0.0,0.00,0.01,0.0046,0.0048, SURF_ID='LAYER24' /
&VENT XB=0.0,0.0,0.00,0.01,0.0048,0.005, SURF_ID='LAYER25' /
&VENT XB=0.0,0.0,0.00,0.01,0.005,0.0052, SURF_ID='LAYER26' /
&VENT XB=0.0,0.0,0.00,0.01,0.0052,0.0054, SURF_ID='LAYER27' /
&VENT XB=0.0,0.0,0.00,0.01,0.0054,0.0056, SURF_ID='LAYER28' /
&VENT XB=0.0,0.0,0.00,0.01,0.0056,0.0058, SURF_ID='LAYER29' /
&VENT XB=0.0,0.0,0.00,0.01,0.0058,0.006, SURF_ID='LAYER30' /
&VENT XB=0.0,0.0,0.00,0.01,0.006,0.0062, SURF_ID='LAYER31' /
&VENT XB=0.0,0.0,0.00,0.01,0.0062,0.0064, SURF_ID='LAYER32' /
&VENT XB=0.0,0.0,0.00,0.01,0.0064,0.0066, SURF_ID='LAYER33' /
&VENT XB=0.0,0.0,0.00,0.01,0.0066,0.0068, SURF_ID='LAYER34' /
&VENT XB=0.0,0.0,0.00,0.01,0.0068,0.007, SURF_ID='LAYER35' /

```



```

&VENT XB=0.0,0.0,0.00,0.01,0.0198,0.02, SURF_ID='LAYER100' /
&VENT XB=0.0,0.0,0.00,0.01,0.02,0.0202, SURF_ID='LAYER101' /
&VENT XB=0.0,0.0,0.00,0.01,0.0202,0.0204, SURF_ID='LAYER102' /
&VENT XB=0.0,0.0,0.00,0.01,0.0204,0.0206, SURF_ID='LAYER103' /
&VENT XB=0.0,0.0,0.00,0.01,0.0206,0.0208, SURF_ID='LAYER104' /
&VENT XB=0.0,0.0,0.00,0.01,0.0208,0.021, SURF_ID='LAYER105' /
&VENT XB=0.0,0.0,0.00,0.01,0.021,0.0212, SURF_ID='LAYER106' /
&VENT XB=0.0,0.0,0.00,0.01,0.0212,0.0214, SURF_ID='LAYER107' /
&VENT XB=0.0,0.0,0.00,0.01,0.0214,0.0216, SURF_ID='LAYER108' /
&VENT XB=0.0,0.0,0.00,0.01,0.0216,0.0218, SURF_ID='LAYER109' /
&VENT XB=0.0,0.0,0.00,0.01,0.0218,0.022, SURF_ID='LAYER110' /
&VENT XB=0.0,0.0,0.00,0.01,0.022,0.0222, SURF_ID='LAYER111' /
&VENT XB=0.0,0.0,0.00,0.01,0.0222,0.0224, SURF_ID='LAYER112' /
&VENT XB=0.0,0.0,0.00,0.01,0.0224,0.0226, SURF_ID='LAYER113' /
&VENT XB=0.0,0.0,0.00,0.01,0.0226,0.0228, SURF_ID='LAYER114' /
&VENT XB=0.0,0.0,0.00,0.01,0.0228,0.023, SURF_ID='LAYER115' /
&VENT XB=0.0,0.0,0.00,0.01,0.023,0.0232, SURF_ID='LAYER116' /
&VENT XB=0.0,0.0,0.00,0.01,0.0232,0.0234, SURF_ID='LAYER117' /
&VENT XB=0.0,0.0,0.00,0.01,0.0234,0.0236, SURF_ID='LAYER118' /
&VENT XB=0.0,0.0,0.00,0.01,0.0236,0.0238, SURF_ID='LAYER119' /
&VENT XB=0.0,0.0,0.00,0.01,0.0238,0.024, SURF_ID='LAYER120' /
&VENT XB=0.0,0.0,0.00,0.01,0.024,0.0242, SURF_ID='LAYER121' /
&VENT XB=0.0,0.0,0.00,0.01,0.0242,0.0244, SURF_ID='LAYER122' /
&VENT XB=0.0,0.0,0.00,0.01,0.0244,0.0246, SURF_ID='LAYER123' /
&VENT XB=0.0,0.0,0.00,0.01,0.0246,0.0248, SURF_ID='LAYER124' /
&VENT XB=0.0,0.0,0.00,0.01,0.0248,0.025, SURF_ID='LAYER125' /
&VENT XB=0.0,0.0,0.00,0.01,0.025,0.030, SURF_ID='LAYER126' /
&VENT XB=0.0,0.0,0.00,0.01,0.030,0.035, SURF_ID='LAYER127' /
&VENT XB=0.00,0.00,0.00,0.01,0.035,0.05, SURF_ID='UPPER' / Top half of
sample

```

```

&VENT XB=0.00,0.00,0.00,0.01,0.05,0.10, SURF_ID='INSULATION' / Upper
portion above sample
&VENT XB=0.00,0.00,0.00,0.01,-0.02,0.00, SURF_ID='INSULATION' / 2cm
section directly below sample
&VENT XB=0.00,0.00,0.00,0.01,-0.06,-0.02, SURF_ID='HOLDER' / 4cm of
steel holder with insulation behind

```

```

&VENT MB='XMAX', SURF_ID='OPEN' /
&VENT MB='ZMIN', SURF_ID='OPEN' /
&VENT MB='ZMAX', SURF_ID='OPEN' /

```

```

&BNDF QUANTITY='GAUGE HEAT FLUX' /
&BNDF QUANTITY='BURNING RATE' /
&BNDF QUANTITY='WALL TEMPERATURE' /

```

```

&TAIL /

```

References

1. National Materials Advisory Board, "Fire Safety Aspects of Polymeric Materials, Volume 6, Aircraft: Civil and Military," Publication NMAB 318-6, Washington D.C. (1977)
2. Lyon, R.E., "Nonhalogen Fire-Resistant Plastics for Aircraft Interiors," FAA Report, DOT/FAA/AR-TN08/5 (January 2008)
3. ASTM Standard 1354-15A, "Standard Test Method for Heat and Visible Smoke Release Rates for Materials and Products Using an Oxygen Consumption Calorimeter," ASTM International, West Conshohocken, PA, DOI: 10.1520/E1354-15A, www.astm.org (2003)
4. ASTM Standard 3801-10, "Standard Test Method for Measuring the Comparative Burning Characteristics of Solid Plastics in a Vertical Position," ASTM International, West Conshohocken, PA, DOI: 10.1520/D3801-10, www.astm.org (2003)
5. ASTM Standard E162-15A, "Standard Test Method for Surface Flammability of Materials Using a Radiant Heat Energy Source," ASTM International, West Conshohocken, PA, DOI: 10.1520/E0162-15A, www.astm.org (2003)
6. UL Standard 94, "Standard for Safety of Flammability of Plastic Materials for Parts in Devices and Applications testing," Northbrook, IL, Underwriter's Laboratories, http://ulstandards.ul.com/standard/?id=94_6 (2013)
7. A. Horner (ed.), "Aircraft Material Fire Test Handbook," FAA report, DOT/FAA/AR-00/12 (April 2000)
8. V. Babrauskas, "Heat Release Rate: The Single Most Important Variable in Fire Hazard," *Fire Safety Journal* 18: 255-272 (1992)
9. Ito, A., Kashiwagi, T., "Characterization of Flame Spread over PMMA Using Holographic Interferometry Sample Orientation Effects," *Combustion and Flame* 71: 189-204 (1988)
10. Pizzo, Y., Consalvi, J.L., Querre, P., Coutin, M., Porterie, B., "Width Effects on the Early Stage of Upward Flame Spread Over PMMA Slabs: Experimental Observations," *Fire Safety Journal* 44: 407-414 (2009)
11. Markstein, G.H., DeRis, J., "Upward Flame Spread over Textiles," *Proceedings of the Combustion Institute* 14: 1085-1097 (1973)
12. ASTM Standard E84, "Standard Test Method for Surface Burning Characteristics of Building Materials," ASTM International, West Conshohocken, PA, DOI: 10.1520/E0084-15A, www.astm.org (2003)
13. Quintiere, J., "The Application of Flame Spread Theory to Predict Material Performance," *Journal of the Research of the National Bureau of Standards*: 61-70 (1988)
14. Grant, G., Drysdale, D., "Numerical Modelling of Early Flame Spread in Warehouse Fires," *Fire Safety Journal* 24: 247-278 (1995)
15. Thomas, P.H., Lawson, D.I., "On the minimum speed of flame propagation in fabrics," Joint Fire Research Operation, Borehamwood, UK (1957)
16. Brehob, E.G., Kim, C.I., Kulkarni, A.K., "Numerical Model of Upward Flame Spread on Practical Wall Materials," *Fire Safety Journal* 36: 225-240 (2001)
17. Stoliarov, S.I., Crowley, S., Lyon, R.E., Linteris, G.T., "Prediction of the Burning Rates of Non-Charring Polymers," *Combustion and Flame* 156: 1068-1083 (2009)

18. DeRis, J., "Spread of a Laminar Diffusion Flame," *Proceedings of the Combustion Institute* 12: 241-252 (1969)
19. Fernandez-Pello, A.C., Williams, F.A., "Laminar Flame Spread over PMMA Surfaces," *Proceedings of the Combustion Institute* 15: 217-231 (1975)
20. Williams, F.A., "Mechanisms of Fire Spread," *Proceedings of the Combustion Institute* 16: 1281-1294 (1977)
21. Fernandez-Pello, A.C., Hirano, T., "Controlling Mechanisms of Flame Spread," *Combustion Science and Technology* 32: 1-31 (1983)
22. Orloff, L. DeRis, J., Markstein, G.H., "Upward Turbulent Fire Spread and Burning of Fuel Surface," *Proceedings of the Combustion Institute* 15: 183-192 (1975)
23. Sibulkin, M., Kim, J., "The Dependence of Flame Propagation on Surface Heat Transfer II: Upward Burning," *Combustion Science and Technology* 17: 39-49 (1977)
24. Annamalai, K., Sibulkin, M., "Flame Spread over Combustible Surfaces for Laminar Flow Systems, Part I: Excess Fuel and Heat Flux," *Combustion Science and Technology* 19: 167-183 (1979)
25. Annamalai, K., Sibulkin, M., "Flame Spread over Combustible Surfaces for Laminar Flow Systems, Part II: Flame Heights and Fire Spread Rates," *Combustion Science and Technology* 19: 185-193 (1979)
26. Pagni, P.J., Shih, T.M., "Excess Pyrolyzate," *Proceedings of the Combustion Institute* 16: 1329-1343 (1977)
27. Saito, K., Quintiere, J.G., Williams, F.A., "Upward Turbulent Flame Spread," *Fire Safety Science* 1: 75-86 (1985)
28. Karlsson, B., "A Mathematical Model for Calculating Heat Release Rate in the Room Corner Test," *Fire Safety Journal* 20: 93-113 (1993)
29. Delichatsios, M.M., Matthews, M.K., Delichatsios, M.A., "An Upward Fire Spread and Growth Simulation," *Fire Safety Science* 3: 207-216 (1991)
30. Stoliarov, S.I., Leventon, I.T., Lyon, R.E., "Two-Dimensional Model of Burning for Pyrolyzable Solids," *Fire and Materials* 38: 391-408 (2013)
31. Lautenberger, C., Fernandez-Pello A.C., "Generalized Pyrolysis Model for Combustible Solids," *Fire Safety Journal* 44: 819-839 (2009)
32. McGrattan, K., Hostikka, S., Floyd, J., Baum, H., Rehm, R., "Fire Dynamics Simulator (Version 5) Technical Reference Guide," NIST Special Publication 1018-5 (2007)
33. Tsai, K., Turnbull, J., Will, G., Drysdale, D., "Upward Flame Spread: Heat Transfer to the Unburned Surface," *Fire Safety Science* 7: 117-128 (2003)
34. Consalvi, J.L., Pizzo, Y., Porterie, B., "Numerical Analysis of the Heating Process in Upward Flame Spread Over Thick PMMA Slabs," *Fire Safety Journal* 43: 351-362 (2008)
35. Quintiere, J.G., Harkleroad, M., Hasemi, Y. "Wall Flames and Implications for Upward Flame Spread," *Combustion Science and Technology* 48:191-222 (1986)
36. Kulkarni, A.K. Kim, C.I., Kuo, C.H., "Heat Flux, Mass Loss Rate, and Upward Flame Spread for Burning Vertical Walls," NIST-GCR-90-584 (1990)
37. Fernandez-Pello, A.C., "Upward Laminar Flame Spread Under the Influence of Externally Applied Radiation," *Combustion Science and Technology* 17: 87-99 (1977)

38. Fernandez-Pello, A.C., "A Theoretical Model for the Upward Laminar Spread of Flames over Vertical Fuel Surfaces," *Combustion and Flame* 31: 135-148 (1978)
39. Tsai, K.C., Drysdale, D., "Flame Height Correlation and Upward Flame Spread Modelling," *Fire and Materials* 26: 279-287 (2002)
40. Hasemi, Y. "Experimental Wall Flame Heat Transfer Correlations for the Analysis of Upward Flame Spread," *Fire Science and Technology* 4: 75-90 (1984)
41. Lattimer, B.Y., "Heat Fluxes From Fires to Surfaces," *The SFPE Handbook of Fire Protection Engineering (3rd ed)*, DiNenno P.J. (ed.), National Fire Protection Association, Quincy, MA 02269, p. 2-269 (2002)
42. Consalvi, J.L., Pizzo, Y., Porterie, B., Torero, J., "On the Flame Height Definition for Upward Flame Spread," *Fire Safety Journal* 42: 384-392 (2007)
43. Delichatsios, M.A., "Turbulent Convective Flows and Burning on Vertical Walls." *Proceedings of the Combustion Institute* 19 : 855-867 (1983)
44. Delichatsios, M.A., "Flame Heights in Turbulent Wall Fires with Significant Flame Radiation," *Combustion Science and Technology* 39: 195-214 (1991)
45. Tu, K.M., Quintiere, J.G., "Wall Flame Heights with External Radiation," *Fire Technology* 27: 195-203 (1991)
46. Gollner, M.J., Williams, F.A., Rangwala, A.S., "Upward Flame Spread over Corrugated Cardboard," *Bombustion and Flame* 158: 1404-1412 (2011)
47. Tewarson, A., Ogden, D., "Fire Behavior of Polymethymethacrylate," *Combustion and Flame* 89: 237-259 (1992)
48. Delichatsios, M.A., "Modeling of Aircraft and Cabin Fires," National Bureau of Standards, NBS-GCR-84-473 (1984)
49. Rangwala, A. S., Buckley, S.G. and Torero, J.L., "Upward Flame Spread on a Vertically Orented Fuel Surface," *Proceedings of the Combustion Institute* 31: 2607-2615 (2007)
50. Holman, J.P., *Heat Transfer, Ninth Edition*, New York: McGraw Hill, p. 377 (2002)
51. Pizzo, Y., Consalvi, J.L., Querre, P., Coutin, M., Audouin, L., Porterie, B. Torero, J.L., "Experimental Observations on the Steady State Burning Rate of a Vertically Orientated PMMA Slab," *Combustion and Flame* 152: 451-460 (2008)
52. Ahmad, T., Faeth, G.M., "Turbulent Wall Fires," *Proceedings of the Combustion Institute* 17: 1149-1160 (1979)
53. Tsai, K.C., Wan, F., "Upward Flame Spread: The Width Effect," *Fire Safety Science* 8: 409-419 (2005)
54. Xie, W., DesJardin, P.E., "An Embedded Upward Fame Spread Model Using 2D Direct Numerical Simulation," *Combustion and Flame* 156: 522-530 (2009)
55. Ren, N., Wang, Y., Trouve, A., "Large Eddy Simulation of Vertical Turbulent Wall Fires," *Procedia Engineering* 62: 443-452 (2013)
56. Li, J., Stoliarov, S.I., "Measurement of Kinetics and Thermodynamics of the Thermal Degradation for Non-Charring Polymers," *Combustion and Flame* 160: 1287-1297 (2013)
57. Li, J., Stoliarov, S.I., "Measurement of Kinetics and Thermodynamics of the Thermal Degradation for Charring Polymers," *Polymer Degradation and Stability* 106: 2-15 (2014)
58. McKinnon, M.B. Stoliarov, S.I., Witkowski, A. "Development of a Pyrolysis Model for Corrugated Cardboard," *Combustion and Flame* 160: 2595-2607 (2013)

59. McKinnon, M.B., Stoliarov, S.I., "Pyrolysis Model Development for a Multilayer Floor Covering," *Materials* 8: 6117 – 6153 (2015)
60. Martin, G.M., McKinnon, M.B., Stoliarov, S.I., "A Pyrolysis Model for Multiple Compositons of a Reinforced Polymer Composite," *Combustion and Flame* (Submitted 2016)
61. Thermal Ceramics, "Kaowool PM Low Temperature Boards." [Online, Cited: October 1, 2014]
<http://www.matweb.com/search/datasheet.aspx?matguid=59a8251a2e6849f0b98ea96e228df036&ckck=1>
62. Kulkarni A.K., Brehob, E., Manogar, S., Nair, R., "Turbulent Upward Flame Spread on a Vertical Wall Under External Radiation," National Institute of Standards and Technology, NIST-GCR-94-638 (1994)
63. Beaulieu, P.A., Dembsey, N.A., "Effect of Oxygen on Flame Heat Flux in Horizontal and Vertical Oreintations," *Fire Safety Journal* 43: 410-428 (2008)
64. Leventon, I. T., Stoliarov, S.I., "Evolution of Flame to Surface Heat Flux During Upward Flame Spread on Poly(Methyl Methacrylate)," *Proceedings of the Combustion Institute* 34: 2523-2530 (2013)
65. Smyth, K.C., Miller, J.H., Dorfman, R.C., Mallard, W.G., Santoro, R.J., "Soot Inception on a Methane/Air Diffusion Flame as Characterized by Detailed Species Profiles," *Combustion and Flame* 62: 157-181 (1985)
66. Santoro, R.J., Yeh, T.T., Horvath, J.J., Semergian, H.G., "The Transport and Growth of Soot Particles in Laminar Diffusion Flames," *Combustion Science and Technology* 53: 89-115 (1987)
67. McBride, B.J., Gordon, S. (ed.), "Computer Program for Calculation of Complex Chemical Equilibrium Compositions and Applications II. Users Manual and Program Description," NASA Reference Publication 1311 (1996)
68. Lyon, R.E., Quintiere, J.G., "Criteria for Piloted Ignition of Solids," *Combustion and Flame* 151: 551-559 (2007)
69. Tewarson, A., "Generation of Heat and Chemical Compounds in Fires," *The SFPE Handbook of Fire Protection Engineering 4th ed.*, DiNenno P.J. (ed.), National Fire Protection Association, Quincy, MA. p. 3-109 (2008)
70. National Institute of Standards and Technology, "NIST Chemistry Webbook," [online, Cited December 1, 2015] <http://webbook.nist.gov/chemistry/>
71. Li, J., Gong, J., Stoliarov, S.I., Gasification Experiments for Pyrolysis Model Parameterization and Validation," *International Journal of Heat and Mass Transfer* 77: 738-744 (2014)
72. Forsth, M., Roos, A., "Absorptivity and its Dependence on Heat Source Temperature and Degree of Thermal Breakdown," *Fire and Materials* 35: 285-301 (2011)
73. Linteris, G., Zammarano, M., Wilthan, B., Hanssen, L., "Absorption and Reflection of Infrared Radation by Polymers in Fire-Like Environments," *Fire and Materials* 36: 537-553 (2011)
74. McKinnon, M.B., "Development of a Model for Flaming Combustion of Corrugated Cardboard," Department of Fire Protection Engineering, University of Maryland, Masters Thesis (2012)

75. Massman, W.J., "A Review of the Molecular Diffusivities of H₂O, CO₂, CH₄, CO, O₃, SO₂, NH₃, N₂, O, NO, and NO₂ in Air, O₂, and N₂ Near STP," *Atmospheric Environment* 32: 1111-1127 (1988)
76. Leventon, I.T., Li, J., Stoliarov, S.I., "A Flame Spread Simulation Based on a Comprehensive Solid Pyrolysis Model Coupled with a Detailed Empirical Flame Structure Representation," *Combustion and Flame* 162: 3884-3895 (2015)
77. Gollner, M.J., Huang, X., Williams, F.A., Rangwala, A.S. "Buoyancy-enhanced Flame Spread over Continuous Surfaces," 7th US Combustion Meeting, Paper # 2F02 (2011)
78. Wang, Y., Jow, J., Su, K., Zhang, J., "Development of the Unsteady Upward Fire Model to Simulate Polymer Burning under UL94 Vertical Test Conditions," *Fire Safety Journal* 54: 1-13 (2012)
79. Ahmad, T., Faeth, G.M., "An Investigation of the Laminar Overfire Region Along Upright Surfaces," *Journal of Heat Transfer* 100: 112-119 (1978)
80. Marxman, G.A., "Combustion in the Turbulent Boundary Layer on a Vaporizing Surface," *Proceedings of the Combustion Institute* 10: 1337-1349 (1965)
81. Zhang, Y., Bustamante, M. G., Gollner, M.G., Sunderland, P.B., Quintiere, J.G., "Burning of Flat Wicks at Various Orientations," *Journal of Fire Sciences* 32: 52-71 (2014)
82. Siegel, R. and Howell, J., *Thermal Radiation Heat Transfer*, New York: Taylor & Francis, p. 838 (2002)
83. Kandola, B.K., Price, D., Milnes, G.J., Da Silva, A., "Development of a novel experimental technique for quantitative study of melt dripping of thermoplastic polymers," *Polymer Degradation and Stability* 98: 52-63 (2013)
84. Hasemi, Y. "Surface Flame Spread," *The SFPE Handbook of Fire Protection Engineering 4th ed.*, DiNenno P.J. (ed.), National Fire Protection Association, Quincy, MA., p. 2-278 (2008)
85. Heskestad, G., "Peak Gas Velocities and Flame Heights of Buoyancy – Controlled Turbulent Diffusion Flames," *Proceedings of the Combustion Institute* 18: 951-960 (1981)
86. Zukowski, E.E., Cetegen, B.M., Kubota, T., "Visible Structure of Buoyant Diffusion Flames," *Proceedings of the Combustion Institute* 20: 361-366 (1984)
87. Fibre Glast Development Corporation, "Product Data Sheet," [Online, Cited: November 5, 2015] <http://cdn.fibreglast.com/downloads/00345-A.pdf>
88. Mouritz, A.P., Gibson, A.G. *Fire Properties of Polymer Composite Materials*, Dordrecht, The Netherlands: Springer, p. 25-31 (2006)
89. Hugget, C., "Estimation of Rate of Heat Release by Means of Oxygen Consumption Measurements," *Fire and Materials* 4: 61-65 (1980)
90. Lyon, R., Walters, R. N., Stoliarov, S.I., Safronava, N., "Principles and Practice of Microscale Combustion Calorimetry," FAA Report, DOT/FAA/TC-12/53 R3 (April 2013)
91. Raffan-Montoya, F., Ding, X., Stoliarov, S. I., Kraemer, R. H., "Measurement of heat release in Laminar Diffusion Flames Fueled by Controlled Pyrolysis of Milligram-Sized Solid Samples: Impact of Bromine- and Phosphorus-Based Flame Retardants," *Combustion and Flame* 162: 4660-4670 (2015)

92. ASTM Standard D7309-13, "Standard Test Method for Determining Flammability Characteristics of Plastics and Other Solid Materials Using Microscale Combustion Calorimetry," ASTM International, West Conshohocken, PA, 10.1520/D7309-13. www.astm.org (2003)
93. Walters, R. N., Hackett, S. M., Lyon, R. E. "Heats of Combustion of High Temperature Polymers," *Fire and Materials* 24: 245-252 (2000)
94. Heskestad, G., "Fire Plumes, Flame Height, and Air Entrainment," *The SFPE Handbook of Fire Protection Engineering 3rd ed.*, DiNenno P.J. (ed.), National Fire Protection Association, Quincy, MA. p. 2-1 (2002)
95. Tewarson, A., Lee, J. L., Pion, R. F., "The Influence of Oxygen Concentration on Fuel Parameters for Fire Modeling," *Proceedings of the Combustion Institute* 18: 563-570 (1981)
96. Tewarson, A., "Experimental Evaluation of Flammability Parameters of Polymeric Materials," *Flame-Retardant Polymeric Materials, Volume 3*, New York : Plenum Press, p. 97-153 (1982)
97. Tewarson, A., "Combustion Efficiency and Its Radiative Component," *Fire Safety Journal* 39: 131-141 (2004)
98. Quintiere, J. G., Lyon, R., Crowley, S., "An Exercise in Obtaining Flame Radiation Fraction from the Cone Calorimeter," *Proceedings of the 14th International Conference and Exhibition on Fire and Materials*: 149-161 (2015)
99. Korver, K.T., "A Generalized Model for Wall Flame Heat Flux During Upward Flame Spread On Polymers," Department of Fire Protection Engineering, University of Maryland, Masters Thesis (2015)
100. Pizzo, Y., Lallemand, C., Kacem, A., Kaiss, A., Gerardin, J., Acem, Z., Boulet, P., Porterie, B., "Steady and Transient Pyrolysis of Thick Clear PMMA Slabs," *Combustion and Flame*, Vol. 162: 226-236 (2015)
101. Kempel, F., Schartel, B., Marti, J. M., Butler, K. M., Rossi, R., Idelsohn, S. R., Onate, E., Hofmann, A., "Modelling the vertical UL 94 test: competition and collaboration between melt dripping, gasification and combustion," *Fire and Materials* 39: 570-584 (2015)
102. Quintiere, J. G., Downey, B. P., Lyon, R.E., "An Investigation of the Vertical Bunsen Burner Test for Flammability of Plastics," FAA Report, FAA, DOT/FAA/AR-TN11/19 (February 2012)
103. Lannon, C. M., "A Methodology for Determining the Fire Performance Equivalency Amongst Similar Materials During a Full-Scale Fire Scenario Based on Bench-Scale Testing," Department of Fire Protection Engineering, University of Maryland, Masters Thesis (2015)
104. ISO Standard 9705:1993, *Fire Tests - Full-scale room test for surface products*," International Standards Organization, Geneva, Switzerland (1993)
105. Kirk, R.E., Othmer, D.F., *Kirk-Othmer encyclopedia of chemical technology*. New York: Wiley (2007)
106. Guerra, P., Alae, M., Eligarrat, E., Barcelo, D., "Introduction to Brominated Flame Retardants: Commercially Products, Applications, and Physicochemical Processes," ed. Eljarrat, E., Barcelo, D., *Brominated Flame Retardants - Handbook of Environmental Chemistry*, Berlin: Springer, Vol:16, p. 1-18 (2011)

107. De Wiit, C. A., Kierkegaard, A., Ricklund, N., Sellstrom, U., "Emerging Brominated Flame Retardants in the Environment," Eljarrat, E., Barcelo, D. (ed.), *Brominated Flame Retardants - Handbook of Environmental Chemistry*, Berlin: Springer, Vol: 16, p. 241-286 (2011)
108. Birnbaum, L.S., Staskal, D.F., "Brominated Flame Retardants: Cause for Concern?," *Environmental Health Perspectives* 112: 9-17 (2004)
109. Kodur, V. K. R., Harmathy, T. Z., "Properties of Building Materials" *The SFPE Handbook of Fire Protection Engineering (3rd ed)*, DiNenno P.J. (ed.), National Fire Protection Association, Quincy, MA 02269, p. 1-155 (2002)
110. Beyler, C. L., Hirschler, M. M., "Thermal Decomposition of Polymers," *The SFPE Handbook of Fire Protection Engineering (4th ed)*, DiNenno P.J. (ed.), National Fire Protection Association, Quincy, MA 02269, p. 1-112 (2008)
111. Yaws, C. L., *Handbook of Thermal Conductivity, Volume 2*, Houston: Gulf Publishing Company, p. 376 (1995)
112. Yaws, C. L., *Handbook of Viscosity, Volume 2*, Houston: Gulf Publishing Company, p. 376 (1995)
113. Poling, B. E., Prausnitz, J.M., O'Connell, J.P., *The Properties of Gases and Liquids, Fifth Edition*, McGraw Hill, p. 3.6, 11.11 (2001)
114. National Institute of Standards and Technology, "NIST-JANAF Thermochemical Tables," [online, Cited December 1, 2015] <http://kinetics.nist.gov/janaf/html/H-064.html>
115. Worksafe Australia: National Industrial Chemicals Notifications and Assessment Scheme, "M390B Unsaturated Polyester Resin," Full Public Report: NA/166, Sydney Australia (July 1994)